Microfluidic platforms for multiplexed functional testing of intact tumor tissues

Adán David Rodríguez Arizpe

A dissertation
submitted in partial fulfillment of the
requirements for the degree of

Doctor of Philosophy

University of Washington

2021

Reading Committee:

Albert Folch, Chair

Venu Pillarisetty

Jonathan T.C. Liu

Program Authorized to Offer Degree:

Bioengineering

University of Washington

ABSTRACT

Microfluidic platforms for multiplexed functional testing of intact tumor tissues

Adán David Rodríguez Arizpe

Chair of the Supervisory Committee:
Prof. Albert Folch
Department of Bioengineering

Despite advances in targeted therapies, cancer treatment continues to face significant challenges as it moves toward the goal of rationally chosen personalized therapy. There is a great need for functional testing platforms that use human, intact tumor tissue to predict patient outcomes to cancer therapy. The successful development of such platforms would advance both drug development and identification of optimal treatments for a given patient (i.e., precision oncology). However, current approaches that solely use patient-derived cells from dissociated tissue typically lack most of the tumor microenvironment (TME) and are not rapid enough to guide patient-specific therapy decisions. Furthermore, the response of each individual to a given treatment can vary widely across the population. This report outlines the progress we have made in developing two digitally fabricated microfluidic platforms that utilize intact patient-derived tumor tissue to solve critical challenges related to the advancement of personalized therapy. The first chapter outlines an introduction to digital manufacturing and laser micromachining through CO_2 laser ablation and compatible bonding techniques for microfluidic applications. The second chapter summarizes the development of a digitally fabricated microfluidic platform (Oncoslice) that allows for selective spatiotemporal exposure of organotypic slice cultures to dozens of drug conditions. The chapter includes published demonstrations of successful microfluidic delivery of small-molecule cancer drug panels to glioblastoma (GBM) xenograft slices and GBM and colorectal cancer patient tumor slices. Furthermore, it includes preliminary results that spear our future aims to utilize the platform to evaluate combination immunotherapies and their interaction with the TME. Finally, the third chapter summarizes our most recent advances in developing a microfluidic platform that enables drug treatment, exogenous T cell therapy, and high-content analysis using hundreds to thousands of similarly sized, precision-sliced cuboidal micro-tissues

("cuboids") produced from a single tumor sample. The chapter incorporates published results related to cuboid sectioning and characterization (i.e., size, viability, TME), microfluidic platform prototype development and functionality, and pilot drug delivery experiments.

TABLE OF CONTENTS

LIST OF FIGURES

LIST OF TABLES

LIST OF SUPPLEMENTARY INFORMATION

ACKNOWLEDGEMENTS

I would first like to express my deep appreciation and gratitude to my advisor, Prof. Albert Folch, for the patient guidance and mentorship he provided during this fantastic journey. The door to Prof. Folch's office was always open whenever I faced complex challenges during my research. Albert consistently allowed this project to be my work. Still, he always steered me in the right direction, outlined my areas of opportunity, and motivated me to rise from all the challenges associated with this project. Similarly, I would like to especially thank Dr. Lisa Horowitz for her support, mentorship, training, and most importantly, for her genuine curiosity and scientific thinking, which was paramount for the success of our work. I will always be grateful for the support of every member of the Folch lab.

I would also like to thank my advisors Dr. Venu Pillarisetty, Prof. Jonathan T.C. Liu, and Prof. Daniel T. Chiu, for their mentorship, support, and advice, which directed our research into fascinating directions. I must also express my very profound gratitude to my parents and family for their unconditional support and motivation during this adventure. Finally, and most importantly, I will be eternally grateful to my wife, Samantha Lankenau, for providing me with unfailing support and continuous encouragement throughout my years of study and through the process of researching and writing this thesis. Thank you!

The work presented here was supported by a grant from the National Cancer Institute (NCI) R01 CA181445-01A1, NCI IMAT R21CA251952, Washington Research Foundation, National Institute of Health, U.S Department of Defense (CA150370), National Science Foundation, UW CoMotion, Juno Therapeutics, and an International Scholars award from the Consejo Nacional de Ciencia y Tecnología (CONACYT) of Mexico.

DEDICATION

To Sam,
my loving wife

Deserts between us
And time on our side

Love knows no distance
When my dreams are of you
No ocean could stop me
No road is too long
Waiting for you
Was my journey home

Silly to think paradise
Would ever be within inches
Of course, it's a bridge
That we must cross
To our dreams
And when I tell you
I will fulfill your dreams
I hope you know

All my dreams are with you

-unknown (08/08/19)

`

INTRODUCTION

The average cost of developing a new cancer drug is now more than $650 million.[1–3] Unfortunately, most pharmaceutical drugs in the clinical development phase never make it to market; in a recent report, 76% of clinical failures were due to a lack of efficacy (52%) or to safety issues (24%), with almost 30% being cancer drugs.[4,5] One of the leading causes of this expensive gridlock is that preclinical animal tests do not accurately predict toxic doses and drug metabolism observed in humans.[6] A recent study of clinical drug development success rates indicated that oncology had the lowest likelihood of approval from phase 1.[4,5] Clearly, there is an urgent need for better functional drug assays based on human tissue, which would more closely mimic patient disease and predict clinical outcomes to complement ongoing efforts using 3D cell culture systems and animal models. In its Provocative Questions in Cancer, the National Cancer Institute (NCI) highlights the potential impact of direct-in-human drug testing approaches: "If systems can be developed that accurately predict drug responses in human, advances in drug treatment or prevention would be dramatically streamlined, and time frames for drug development shortened considerably. The ultimate benefit for patients would be immense".[7] Functional assays can potentially complement and extend genomics-based approaches for personalized oncology by capturing critical determinants of therapeutic response such as tissue architecture, tumor heterogeneity, and the tumor microenvironment (TME).[8] Also, functional drug assays on patient tissue may serve as a way to guide therapy decisions to complement current genomic approaches to personalized medicine.[9]

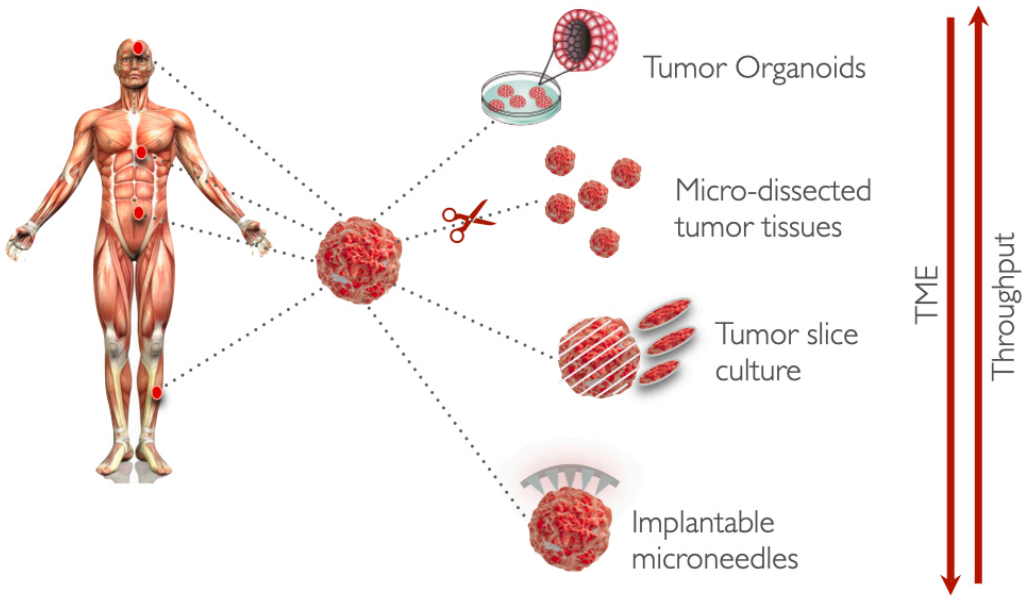

Figure 1. Live Tumor Tissue Models.

Live tumor tissue drug testing models have shown a tremendous promise as drug activity models and have the potential to advance precision and personalized medicine. The models are arranged from top to bottom in decreasing order of throughput and increasing order of complexity of the TME, as shown by the arrows on the right.

With increasing evidence that tumor-associated stromal cells play critical roles in tumorigenesis and tumor progression,[10] it has become clear that dissociated tumor cell culture models cannot faithfully replicate the spatiotemporal complexity of tumor biology.[11] New technologies to probe intact tissues are needed to advance drug testing and personalized medicine. Over the past decade, investigators have increasingly utilized intact live tumor tissues to replicate tumor physiology in diverse functional assays. One of the most acute challenges in functional precision cancer medicine arises from the fact that dissociated cells are insufficient for the functional assays – to preserve the TME, these assays should be performed on intact tissue, whose availability is scarce. The small size of clinical samples has prompted many groups (including

`

ours) to use various approaches (**Fig.1**). The following live tissue assay approaches are listed from less to more preservation and faithful representation of the TME. 1) Tumor spheroids (small spheres or "organoids" formed from patient-derived, dissociated cells[12–19]) create cell-cell and cell-matrix 3-D interactions that more closely resemble in-vivo interactions and have been used for high-throughput drug screening assays[20] that can be predictive of the patient's responses.[12,13] However, these spheroids retain only a limited amount of the original TME because they rely on an amplification or growth step. 2) Microdissected tumors (μDTs), derived from cutting of tumors into submillimeter tissue pieces (confusingly, often termed "spheroids" as well), maintain the original TME relatively intact.[21–27] 3) Tumor slices[28,29] is an approach sensitive to tissue scarcity, but this limitation is potentially addressed by a microfluidic approach that miniaturizes multiplexed drug delivery to individual slices.[30–32] 4) Patient-derived xenograft (PDX) mouse models permit the study of drug responses in an intact organism (including immune checkpoint blockade in humanized PDX[33]), but with the caveats that all or most of the TME is from the host mouse and PDX from individual patients grow too slowly to inform initial post-operative therapeutic decisions. Lastly, 5) implantable or needle microdelivery devices[34,35] locally deliver small doses of (up to 16) drugs to the tumor *in vivo,* with maximal preservation of the TME, but subject to limitations of tumor accessibility and patient safety.

Microfluidic technology is generally well suited for the challenge of delivering minute amounts of drugs to small tissue biopsies, such as live human tissue, which is almost always available only in very limited quantities. We have addressed the NCI Provocative Question by developing two microfluidic platforms that miniaturize functional drug testing on intact tumor slices and μDTs. The first chapter of this report outlines a detailed description of the laser-based fabrication techniques we employed to develop microfluidic platforms. Furthermore, it describes

how the application of digital manufacturing strategies, in combination, offers low-cost, efficient, and rapid microfluidic fabrication processes for the effective development of microfluidic technologies with the potential for an organic translation towards clinical tools. The second chapter reports most of our published results on a microfluidic platform for high-throughput chemosensitivity testing on individual slice cultures. [32,36–38] Finally, the third chapter describes our published results on a microfluidic platform that utilizes uniformly sized microscale "cuboids" of live tissue with well-preserved tissue microenvironments.[39] With both microfluidic platforms we demonstrate how intact tissues and microfluidic technologies can facilitate functional drug testing and potentially create an enormous impact on biological research, drug discovery, and personalized medicine.

Chapter 1. LASER-BASED FABRICATION OF THERMOPLASTIC MICROFLUIDIC DEVICES

1.1 ABSTRACT

Microfluidic technologies show great promise for improving diagnostics, biological research, and biomedical applications, such as cancer research. Despite the great success and potential of microfluidic technologies, clinical adoption remains a big challenge. Challenges related to the ease of widespread validation testing and commercialization directly attribute to slow clinical adoption. There is a critical need to develop cost-effective and rapid prototyping of microfluidics in academic research laboratories that facilitate an organic translation of large-scale manufacturing. In this chapter, we outline a microfluidic fabrication process based on digital manufacturing techniques, mainly involving CO_2 laser ablation of thermoplastics. We focus on demonstrating microfluidic fabrication through a combination of computer-aided design (CAD), CO_2 laser ablation, and rapid bonding techniques such as solvent and transfer adhesive bonding. The application of these fabrication strategies offers low-cost, efficient, and rapid microfluidic fabrication processes for the effective development of technologies with the potential for an organic translation towards clinical tools.

1.2 INTRODUCTION

Microfluidics, a technology that focuses on engineered manipulation of fluids at the submillimeter scale, is widely recognized for its promise for improving diagnostics, biological research, and biomedical applications.[40,41] As the field continues to evolve, microfluidics has shown great potential to serve as a cancer research tool. Microfluidic technologies are of great value due to their high sensitivity, high throughput, low cost, and enhanced spatiotemporal

control.[40] Developing and applying microfluidic technologies to address the unmet challenges in cancer can lead towards answering complex/fundamental biological questions, improving drug development, and advancing precision medicine. Microfluidic technologies face challenges related to the ease of widespread validation testing and commercialization. Such barriers are directly related to the fabrication technologies employed to develop a microfluidic platform and the difficulty of an organic translation towards large scale manufacturing and commercialization.

Ever since its early introduction in the late 1990s, materials used for microfluidic devices have evolved from traditional silicon and glass to elastomers, paper, hydrogels, and thermoplastics [42–44]. Key factors such as biocompatibility, cost, ease of fabrication and prototyping, manufacturability, and commercialization are paramount for microfluidics technologies' success. Defining fabrication materials play a crucial role in developing and commercializing microfluidic technologies. In addition to selecting the right materials, identifying compatible fabrication techniques also dictates microfluidic technologies' success, especially when bridging the gap towards commercialization and large-scale manufacturing. In 1998, Whitesides used polydimethylsiloxane (PDMS), an optically transparent, gas-and-vapor-permeable elastomer, for the fabrication of complex microfluidic devices and helped soft-lithography become the most widely adopted method for fabricating microfluidic devices.[41] Despite all the advantages offered by PDMS, there are several limitations to implementing biomedical research material. For example, PDMS is not adequate for drug-based studies; both absorption into PDMS[45–52] and adsorption onto PDMS[53] can potentially alter experimental outcomes by changing the target concentrations and by partitioning molecules in undesired regions of a microfluidic device. Additionally, the manufacture and distribution of PDMS devices are not easily scalable; complex PDMS microfluidic devices are hardly translatable to large-scale manufacturing methods such as

injection molding, rolling, and embossing. Finally, making PDMS prototypes for iterating on a new design is relatively easy for an experienced lab technician, but making numerous copies and packaging them for collaborators or commercialization is exceptionally challenging.[44,54]

The need for an increase in fabrication efficiency and ease of translation has motivated researchers to investigate alternative fabrication procedures. Recently, there has been a push towards materials and fabrication methods compatible with digital manufacturing (DM). DM is an integrated production method in which computers guide modular three-dimensional (3D) design, performance simulation, automated fabrication, assembly, and quality control.[55,56] With DM, designs can be digitally inspected and adjusted, annotated, and cloud-shared with collaborators, resulting in better design turnaround time, cost, and performance.

A recent review by our group (Folch et al.) describes the outlining properties and DM for its application in microfluidic technologies. [55] Manufacturing techniques for microfluidics are subtractive, additive, and molding (also known as formative).[55] All DM methods share (1) the ability to produce a physical device from a digital design file and (b) the ability to encode the fabrication process as a set of parameters. Most importantly, both the design files and process specifications can be shared electronically with collaborators. There are various DM techniques; however, the fabrication of microfluidic devices must meet basic requirements, limiting and guiding the choice of techniques and materials. The first requirement for the technology of choice is to create cavities and channels in the submillimeter scale. The second requirement is for the channels to be constructed in a transparent material to facilitate microscopic observation.

Most importantly, all materials must be biocompatible. Most additive manufacturing techniques such as stereolithography and photopolymer inkjet satisfy both requirements and have been widely applied for microfluidics with success.[55] On the other hand, DM technologies based

on subtractive manufacturing, such as laminated object manufacturing (LOM, also called laser-cutting)[57] and computer numerical control (CNC) milling[58], also meet both requirements microfluidics.

In this chapter, we demonstrate our results obtained through LOM, specifically with CO_2 laser ablation. LOM is a low-cost technique in which plastic, metal, ceramic, or paper laminates are cut with a laser[57] or a physical plotter tip[59], aligned layer by layer, and bonded with chemicals or transfer adhesives to create 3D objects.[55] Recent reports show successful laser ablation–based microstructure of polymeric substrates for biomicrofluidic applications.[60–62] Thermoplastics such as polymethyl methacrylate (PMMA), polycarbonate, polystyrene, and cyclic olefin copolymer (COC) are ideal; they are directly compatible with most laser cutting machines and are optically transparent.[44,63] Here, we demonstrate the fundamental aspects behind laser-based fabrication of microfluidic devices through CO_2 laser ablation, CAD-to-chip process, and compatible bonding techniques. We successfully applied our findings obtained using this DM technique and developed two microfluidic devices for cancer research, as shown in the following chapters.

1.3 Results & Discussion

1.3.1 *CO_2 laser ablation*

Laser material processing uses laser energy to modify the shape or appearance of a material. Lasers covering wavelengths from UV to thermal IR (8-12 μm) are standard for laser micromachining of thermoplastics. UV-Lasers are frequently used for creating microstructures in polymer materials. [63] The ablation of thermoplastics is a complex combination of photochemical and photothermal processes.[64] During this process, some chemical bonds of the substrate are broken directly during photon absorption. In contrast, others are broken thermally by the released

heat of excited molecules that do not break up photochemically.[63] However, the micromachining process is slow and with a limited depth per laser pulse.[65] Such characteristics have a substantial impact on processing time, and, additionally, laser equipment is costly ($100,000).

On the other hand, CO_2 lasers can pattern sub-millimeter microchannels in thermoplastics at high speed and relatively low equipment costs ($15,000). Compared to UV lasers, a CO_2 laser continuously emits infrared radiation at a wavelength of 10.6 μm and always ablates the underlying substrate thermally. Wherever the focused laser beam meets the workpiece surface, the irradiated spot's temperature will rise rapidly, such that the material will first melt and then decompose, leaving a void in the workpiece.[63] The decomposition mechanism depends on the strength of the monomers' chemical bonds that make up the polymer and the polymer's structure.[63,66] For example, in the case of poly (methyl methacrylate) (PMMA), the material vaporizes in the form of monomers when it reaches boiling temperature and leads to cavities not contaminated by degradation components.

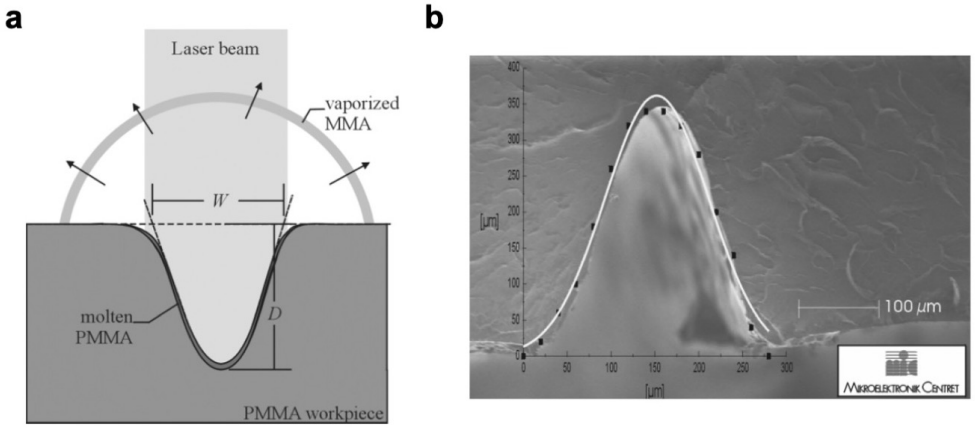

Figure 1.1 CO_2 Laser Ablation

(a) Schematic of the laser beam, the micromachined groove, including the molten PMMA, and the vaporized hemispherical cloud of MMA leaving the cut-zone. (**b)** SEM micrograph of a

PMMA channel cross-section with overlaid Gaussian fit. *Adapted with permission from Klank et al.* [63]

During the laser cutting process, the beam moves across the workpiece's surface, creating a pool of melted polymer. The pool is driven away from the hot spot into all directions by heated gases of vaporizing plastic, while most of the melted material is solidifying in the wake of the beam. In this modus, the moving laser beam can cut structures such as microchannels into the polymer substrate, as shown in Fig. 1.1a. The channel's cross-section highly depends on the polymer's thermal diffusivity (speed of heat dispersion) and the laser beam's intensity distribution. [63] Since the thermal diffusivity of polymeric materials is very low, the intensity distribution dictates the channel cross-section, which usually follows a Gaussian-like profile (**Fig. 1.2b**). In the following sub-sections, we describe the typical workflow for microfluidic design, two types of laser ablation techniques, calibration process, processing for transparency, and bonding techniques.

1.3.2 *CO_2 laser engraving/cutting for microfluidic design*

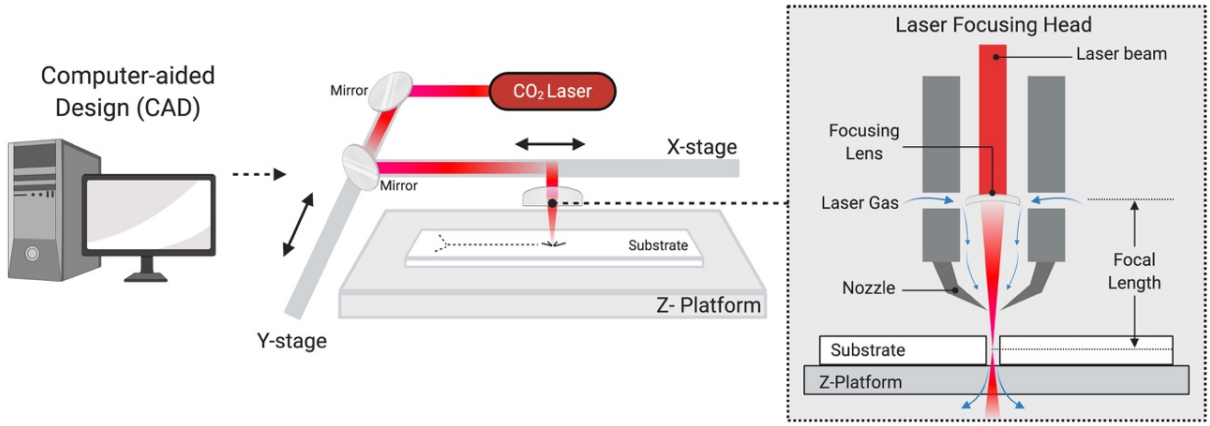

Figure 1.2 CO_2 laser micromachining workflow overview

Designs are made using compatible computer-aided design software and sent to a direct-write laser machining system. The laser system consists of a stage that Z-axis for optimal substrate positioning. The CO_2 laser has a motor placed on the X-axis and moves in both X and Y directions. The laser focusing head has an embedded focusing lens and a gas aperture.

To increase prototyping speed/flexibility and production of our microfluidic devices while maintaining costs low, we focused on CO_2 laser systems to fabricate microfluidic channels on thermoplastic substrates. We mainly utilized PMMA because of its high compatibility with CO_2 laser machining, low cost, chemical properties, optical transparency, biocompatibility, and ability to thermally bond itself to create sealed microchannels. As shown in Fig. 1.1, the user designs microfluidic architectures using computer-aided design software such as AutoCAD and sends it directly to the laser system for automatic machining. In most laser systems, the CO_2 beam moves by robotic arms in two dimensions across the entire substrate area. The microchannels are machine by the ablation process when the laser focuses on the laser substrate. The laser power, beam motion speed, and the number of passes of the laser dictate any feature's width and depth. To fabricate desired microchannel dimensions, the user needs to calibrate the laser machining process for any given design.

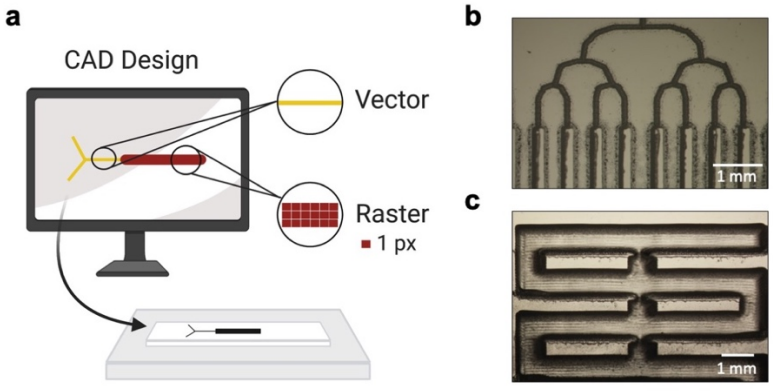

Figure 1.3 Vector and Raster laser process overview

(a) Schematic of laser vector and raster engraving specification in CAD drawing software. Sample images of a vector **(b)** and raster cut **(c)** microchannels (before back-end processing/cleaning and surface treatments).

A laser system can perform cutting, engraving, and marking. When cutting, the laser beam goes all the way through the material, while engraving only partially removes material from the top surface. On the other hand, marking does not remove material but only changes the color of the material. We focus mainly on cutting and engraving for microfluidic device fabrication, as marking is commonly used for metals and other applications.

The input file defines the design, which can contain either vector or raster images. Most CO_2 laser systems recognize both types of images, which enable the user to fabricate various types of microchannels. It is essential to understand the difference between vector and raster processes (**Fig.1.3**). A vector image stores lines as geometric formulas, and a laser system recognizes them as paths. On the other hand, raster images are pixel-based. The dots per inch or pixels per inch (DPI) in the raster image directly affects the level of detail imprinted onto the material. For both processes, the power % and speed % of the laser beam determine the depth and width. For microfluidic design, vector cuts allow for the creation of narrow microchannels (<100 μm wide) or through-cut features. Conversely, raster cuts permit control of the width (>100 μm) and microchannels' depth but are not suitable for through-cuts. Therefore, a microfluidic device design usually contains both processes, depending on its application and purpose.

Apart from the different ways a laser system processes a vector and a raster image, engraved channels also present differences. Vector channels cut in both vertical and horizontal directions (X & Y) in the substrate area present very similar characteristics. On the other hand, raster channels cut vertically (Y) yield scalloped edges, while horizontal channels have much smoother edges.[65] High powers and low speeds result in deep microchannels, while the inverse results in shallow channels. The main difference between these two processes during the

fabrication of microchannels is creating high aspect ratio features. Vector cuts provide precise and smooth-edged microchannels but have a relatively low width to depth aspect ratio. However, raster cuts can provide a higher width to depth aspect ratio.

1.3.3 *Identifying laser settings for microfluidic device design*

When using a CO_2 laser system to fabricate microfluidic devices, the user needs to find the optimal process (vector/raster) and settings (power/speed) to create the desired microchannel architectures in any material, such as PMMA. Defining the optimal process can be achieved through a laser calibration by investigating depth ratios for both vector and raster processes by varying the power %, speed %, and the number of passes. We utilized a Universal Laser Systems, VLS3.60 system with a 10.6 μm CO_2 laser with a maximum power of 30 watts, High Power Density Focusing Optics (HPDFO) lens, and integrated gas assist.[67] Similar to our studies, Maguire et al. recently examined microfluidic fabrication results using a 10.6 μm CO2 engraving laser on cast PMMA, in both raster and vector mode, with a 1.5" lens and an HPDFO lens.[65] Here, we complement both findings to demonstrate the fundamental differences between raster and vector process calibrations for microfluidic fabrication.

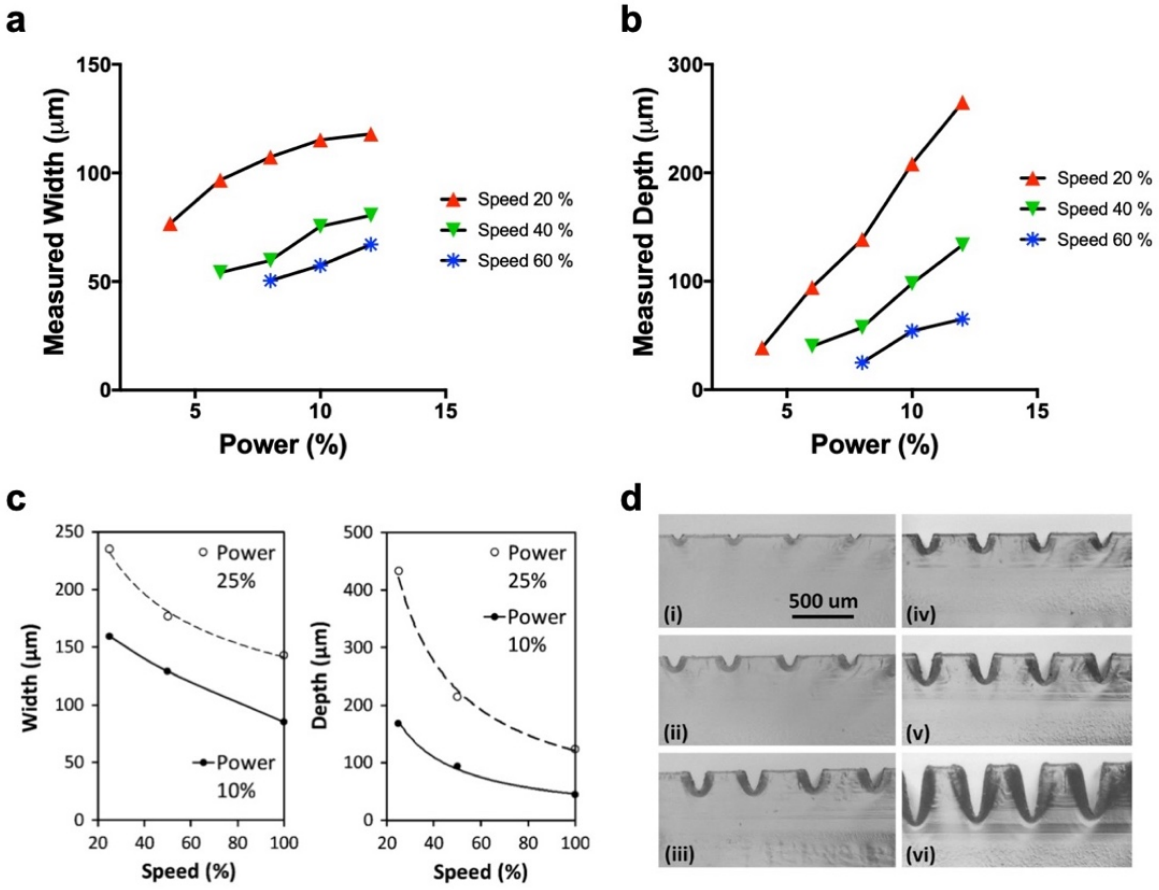

Figure 1.4 Vector engraving

Vector channel width **(a)** and depth **(b)** versus power, for speeds of 20%, 40%, and 60%. **(c)** Vector channel width and depth versus speed, for powers of 10% (2.5 W) and 25% (6.25 W). **(d)** Vector written channel cross-sections, for power of 10%, at speeds of **i** 100%, **ii** 50%, and **iii** 25%, and for powers of 25%, at speeds of **iv** 100%, v 50%, and vi 25%. All images are at the same scale. *Graphs and images in **(c)** and **(d)** adapted with permission from Tweedie et al.* [65]

To understand vector engraving characteristics in PMMA substrates, we explored the change in width and depth as a function of power % and speed %. We utilized a power % ranging from 2-12 % and did 2% increments at 20, 40, and 60% speed (**Fig. 1.4a,b**). [68,69] As expected, we

observed an incremental change while increasing power and a decrement with higher speeds for the width. At settings with low power and high speeds, we found that the laser did not produce engravings in PMMA. For example, 12% power and 40% speed settings result in the minimum width of ~48 μm.

Similarly, there was a higher depth at high power % and low speed % for the depth. We found that the shallowest microchannel of ~25 μm (~50 μm wide) results with an 8% power and 60% speed. Through a similar approach, Maguire et al. reported a minimum width of ~80 μm, but with a depth of only 50 μm (**Fig.1.4c**). We can predict the depth and width at a given speed and power setting in our selected range with the obtained curves. For example, for vector cuts made at a 20% speed, we could estimate a depth using the resulting linear regression D = 28.33 (P%) – 77.48, where D is the channel's depth. Note that the channel width changes more noticeably with depth for vector engraved channels.

By following a similar strategy, any user could identify the optimal vector engraving settings to fabricate any given design. Intuitively, the power and speed range would be different, depending on the desired dimensions. However, vector engraving suffers a limitation when the desired microchannel needs a high depth to the width aspect ratio or a through-cut in a thick PMMA substrate (>300 μm). This limitation can be solved by gradually removing material through repeated laser passes, as shown in Fig. 1.4d. With this technique, the cut depth increases linearly with the number of passes. Similarly, Fig.1.4d also shows how vector engraved channels closely approximate V-grooves.

To grasp the features of raster engraving, we followed a very similar approach. During this process, we noted that the edge smoothness of a channel depends on the channel's orientation (vertical or horizontal) concerning the X-axis of the robotic arms (**Fig. 1.5a**). Vertical channels

showed scalloped edges, while horizontal channels had much smoother edges (Fig. 1.5b).[65] Also, for raster engravings, a power setting higher than 10% at high speeds (>90%) is required to prevent the scanned line from breaking into individual points. Individual scanning points arise due to the interaction between the ablation threshold and the laser's pulse frequency and speed, where there is no independent control of these two laser parameters.[65] With raster engraving, re-deposited material is visible as dark-edged spots along the channel top surface, and the amount increases with channel depth. Also, the base is not transparent in back-illumination because of surface roughness.

We focused our investigation on understanding the difference between the dimensions drawn in a CAD file and the resulting channel when engraved in both orientations (**Fig.1.5a,b**). For this purpose, we drew channels with widths ranging from 300 to 700 μm and raster engraved them in both orientations at a constant power range 80-100% (80-90% not shown) and speeds ranging from 18-28% (24-28% not shown). As shown in the resulting plots, vertical raster engravings show more noise and are less intuitive than horizontal raster engravings. The evident difference in edge smoothness directly attributes to the observed difference between vector and raster engravings. As expected, the drawn dimensions differ significantly from the resulting channel dimensions. However, as with vector engravings, a linear regression can estimate the required CAD drawing dimensions and laser settings to obtain a channel with a particular width and depth dimensions. For example, for a raster engraving made at 100% and 20% speed, for horizontal channels Mw = 0.9952 (Cw) + 156 and for vertical channels Mw = 1.094 (Cw) + 206, where Mw is the measured/resulting width and Cw is the CAD file width. A similar approach could be performed for other power and speed variations, depending on the target dimensions of a microchannel.

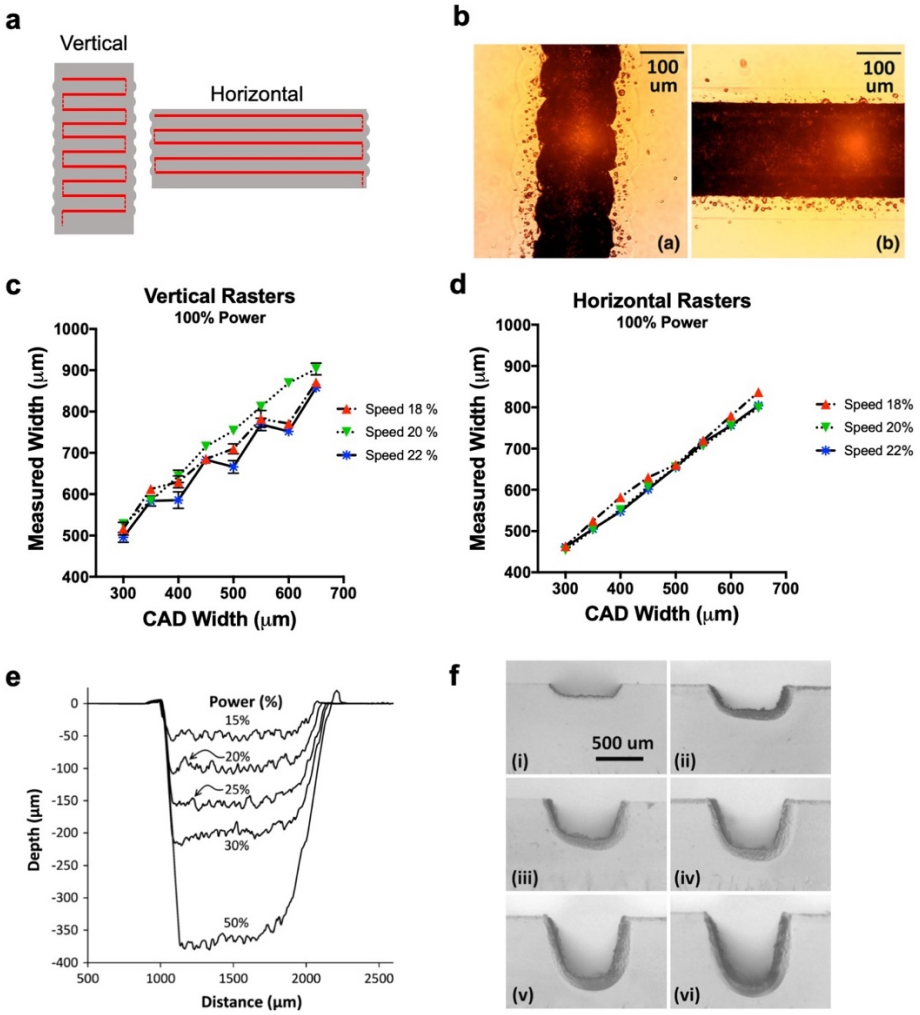

Figure 1.5 Raster engraving

(a) Schematic of substrate orientation for laser raster engraving. **(b)** Images for raster written channels in back illumination. The vertical direction channels show edge scalloping not seen on the horizontal direction channels, directly produced by the raster engravings. Sample microchannel width calibration for vertical **(c)** and horizontal **(d)** raster engravings. The horizontal substrate orientation for raster engraving shows a more uniform curve compared to the vertical orientation. **(e)** Stylus profilometry scans of raster engraved channels at 25% speed. Laser Power is indicated as a percentage of peak power. **(f)** Raster engraved channels via multiple lasers passes, at focus, with backlighting. Parts **(i)** to **(vi)** are sequentially engraved for 1X, 2X, 3X, 4X, 5X and 6X times, with the same settings (power 50%, speed 50%). All images are to the same scale. *Images and graphs in **(b)**, **(e)**, and **(f)** adapted with permission from Tweedie et al.* [65]

As with vector engraving, we follow a similar approach to estimate the relationship of power and speed to the depth of a channel fabricated through a raster process. As expected, we observed deeper and wider channels with a high power% and low-speed%. Maguire et al. investigated the increase in depth as a power function from 15 to 50% at a constant speed of 25%. Through stylus profilometry scans, they were able to quantify the depth increase and reported a minimal usable depth of ~50 μm (Fig. 1.4e).[65] The profiles showed slightly raised edges at the channel tops and are characteristic of the thermal melt removal process. As with vector engraving, material re-deposition can be decreased through gradual material removal, as shown in Fig. 1.4f. Note that raster engraved channels show a profile that closely approximates a U-shape groove compared to the V-shaped grooves of vector-engraved channels.

Overall, these findings demonstrate the fundamental characteristics of vector and raster engraving/cutting in PMMA substrates. For microfluidic fabrication with a CO_2 laser system, a new user would need to understand the relationship between power and speed for both vector and raster processes to produce designs starting from a CAD drawing effectively. As shown in this section, the most straightforward strategy is to develop width and depth calibration curves for both vector and raster processes. Notably, these curves would be independent for each material. After understanding each process's differences, a design could contain a wide variety of vector/raster combinations with different power/speed settings. Most laser systems allow the user to specify up to 10 different settings for a given pass, which allows for the fabrication of complex microfluidic structures. After identifying the optimal process and settings for a given design, prototyping and fabrication result in an extremely rapid DM process.

1.3.4 *Back-end transparency processing and bonding*

CO_2 laser ablation of polymeric substrates typically results in the introduction of defects and loss of clarity. Defects occur due to chaotic vaporization and solidification of material as it is ablated from the surface by the laser beam. Surface roughness and lack of transparency can negatively impact fluid flow and optical-based biological endpoint analyses in microfluidic devices.[70] To improve surface quality, several post-processing methods have been developed, including thermal cycling[71] and surface coating[72]. Thermal cooling lowers the surface roughness of PMMA by heating the material to 60° C for 30 min and cooling again reduces roughness without affecting feature dimensions. Surface coating relies on a more complex and expensive protocol that selectively coats channel walls with liquid coatings[72–74]. Although these processes have shown success, another prominent alternative is surface quality enhancement through solvent vapor exposure.[75] This process has shown an edge due to its simplicity, control, compatibility with a wide variety of polymers, and its bonding application. Solvent-based treatments/bonding can be a high throughput process that is readily scalable from prototyping to mass production.[76]

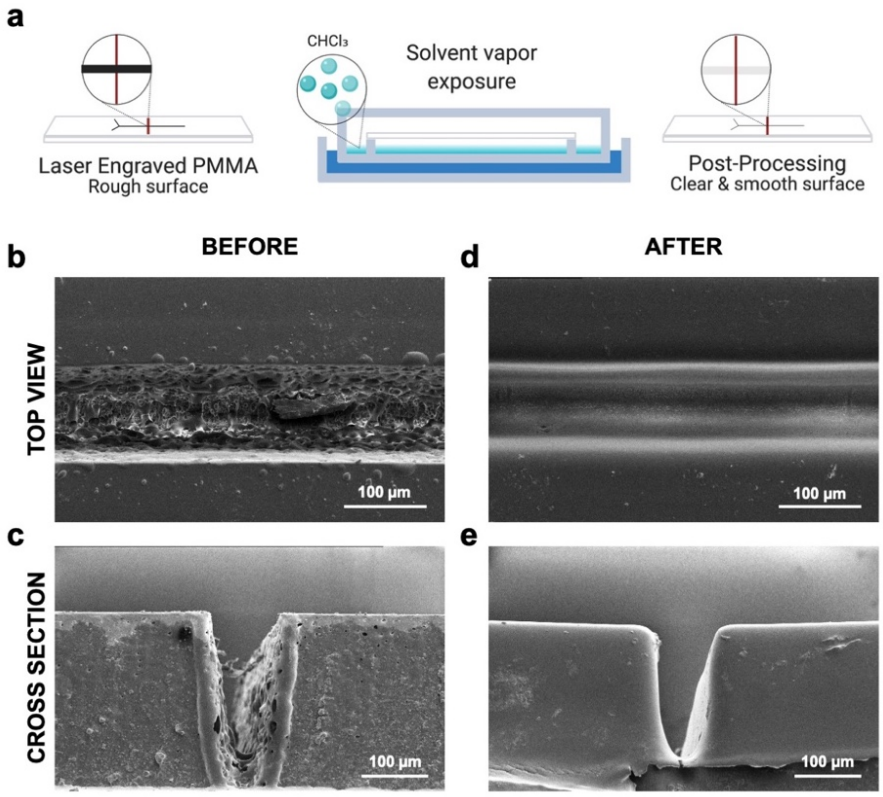

Figure 1.6 Back-end processing for surface quality

(a) Schematic of solvent vapor exposure process for surface roughness removal of laser engraved PMMA substrates. Chloroform vapor is concentrated in a sealed chamber that sits atop a room-temperature water bath leveled to the surface. SEM images of vector engraved microchannels before **(b,c)** and after **(d,e)** chloroform vapor exposure. Uniform chloroform vapor exposure results in clear and smooth channels.

Fig. 1.6a shows increased surface quality through solvent vapor exposure through direct exposure to a saturated vapor atmosphere (**Fig. 1.6a**). The thin solvent-saturated surface layer causes reflow of polymer and thereby smoothes out rough features. This process also creates a gradient in the polymer viscosity in a shallow region at the surface, which allows the mixing of two polymer layers during bonding under pressure and temperature.[75]

Notably, this process's solvent selection highly depends on the polymer (solute) and their respective Hildebrand solubility parameters. The parameter is a numerical value that indicates the relative solvency behavior of a specific solvent. The solvent's cohesive energy density derives

from the heat of vaporization or the energy required to vaporize a liquid, and it defines the Hildebrand parameter.[77] The cohesive energy density of a liquid is a numerical value that indicates the energy of vaporization in calories per cubic centimeter and directly reflects the degree of van der Waals forces holding the liquid together. The correlation between the vaporization and van der Waals forces translates into a correlation between vaporization and solubility.[77] Interestingly, this happens because the same intermolecular attractive forces are required to vaporize or dissolve a liquid. As proposed by Joel H. Hildebrand, materials with similar cohesive energy density values are miscible. In other words, if the cohesive forces for each material are similar, their molecules can readily coexist, and dissolution of the solute will occur. Hildebrand proposed the square root of the cohesive energy density as a numerical value indicating the solvency behavior of a specific solvent:

$$\partial = \sqrt{c} = \sqrt{\frac{\Delta H - RT}{V_m}}$$

Equation 1.1 Hildebrand Equation

where c = cohesive energy density, ΔH = heat of vaporization, R = gas constant, T = temperature, V_m = molar volume ∂(SI) = $MPa^{1/2}$ = 2.0455 x ∂ [$cal^{½}cm^{3/2}$]. [76,77] Table 1.1 outlines the solubility parameters of relevant solvents and thermoplastics reported in literature.[76–79]

Table 1.1 Solubility parameters of solvents and thermoplastics

Solvent	**∂ $MPa^{1/2}$**
Diethyl ether	15.4
Cyclohexane	16.8
Benzene	18.7

`

Chloroform	18.7
Acetone	19.7
Methylene Chloride	20.2
Ethylene dichloride	20.2
Ethyl Alcohol	26.2
Glycerol	36.2
Water	48.0
Thermoplastic	**∂ MPa$^{1/2}$**
Polytetrafluoroethylene (PTFE)	12.6
Polyethylene (PE)	16.3
Cyclic olefin copolymer (COC)	17.7
Polystyrene	18.6
Poly (methyl methacrylate) (PMMA)	18.7-18.9
Poly (vinyl chloride) (PVC)	19.4
Polycarbonate (PC)	19.4
Poly (Ethylene Terephthalate) (PET)	21.8

For example, PMMA has a solubility parameter of 18.7-18.9. Therefore, a solvent with a similar parameter would be required to ensure a maximum solvency and polymer reflow. Of the solvents listed in Table 1, chloroform vapor has been shown to solvate a PMMA film to the most significant degree and about six times more than ethylene dichloride.[77] Solvents with more significant differences in solubility parameters have a less swelling effect.

We investigated the process of surface smoothing through solvent vapor exposure by following a similar protocol as the one reported by Ogilvie et al. and exposed laser ablated PMMA microchannels. For this purpose, we vector engraved microchannels of ~125 μm and exposed them to chloroform vapor for 1-6 minutes. We imaged vector engravings before and after treatment using a scanning electron microscopy (Fig. 1.6 c-d). As shown in Figs. 1.6 b&c, the surface of the microchannels was rough as expected. We experimented with different exposure times and found that 4 minutes yielded the best outcome, as shown in Figs 1.6 d&e. At lower exposure times, the surface still contained rough areas, while higher times resulted in excessive polymer reflow seen as complete "melting" or microchannel collapse. As expected, our results concur with the results reported by Ogilvie et al. and others.[70,75]

After performing this study, we believe that the exposure time could be different depending on a specific PMMA microfluidic device's characteristics. The dimensions of a microchannel dictate the degree of solvation required to achieve optimal surface smoothness and clarity. Nevertheless, due to this process's simplicity and control, finding the optimal conditions can be achieved through a time-lapse study; with optimal conditions found, surface smoothness through vapor exposure can become a high throughput process that is readily scalable.

1.3.5 *Solvent bonding*

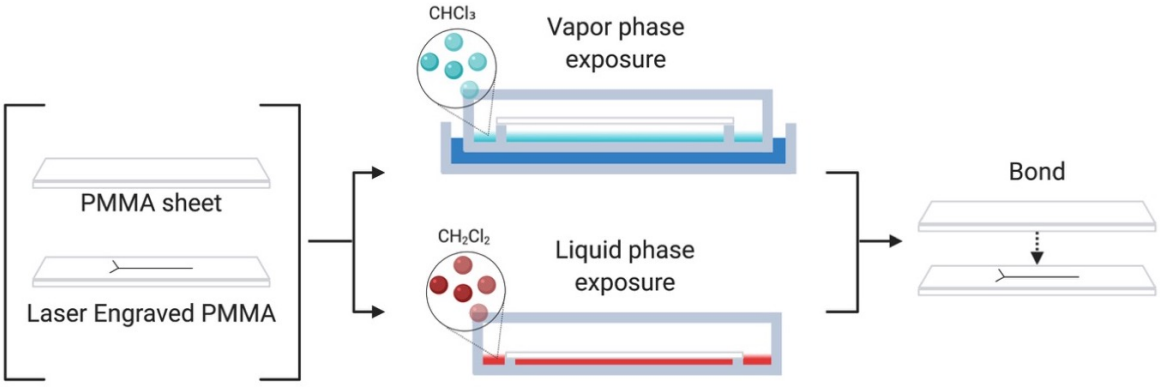

Figure 1.7 Solvent bonding overview

Schematic of vapor and liquid phase solvent bonding processes for laser engraved PMMA substrates. Laser engraved open microchannels sealed through solvent bonding techniques. The thermoplastic substrates are treated in a closed chamber and directly pressed together to form leak-proof bonds. PMMA substrates can be bonded through chloroform or methylene chloride exposure in their vapor or liquid phase. The solvent bonding process is directly dependent on microfluidic design.

Solvent bonding is a direct bonding process where a chemical acts as a solvent for another material with similar solubility Hildebrand parameter. For thermoplastics, solvent bonding takes advantage of a polymer's solubility in a selected solvent to achieve entanglement of polymer chains across the interface. When the surface of a thermoplastic is solvated, polymer chains become mobile. Mobile chains can readily diffuse across the solvated layer, leading to the extensive intertwining of chains between two surfaces and resulting in strong and irreversible bonds.[76] As described earlier, along with back-end surface treatments, solvent bonding can be a high-throughput process scalable from prototyping to mass production. Depending on the application, solvents can be applied to thermoplastic substrates in either the liquid or vapor phase. Liquid phase application is usually used with polymer/solvent systems with non-equal solubility parameters to prevent excessive solvent uptake, leading to microchannel deformation during bonding.

`

Similarly, liquid phase application is also a better technique to bond thicker PMMA substrates (>1mm) to thinner PMMA bonded structures. Vapor phase application can avoid over-exposure and channel deformation issues by allowing a more controlled exposure of solvent molecules to the polymer surface.[76] Additionally, the vapor solvent technique can be used for both the back-end surface quality enhancement and solvent bonding during a single step. For both methods (vapor/liquid), the addition of controlled pressure and temperature promotes a stronger bond.

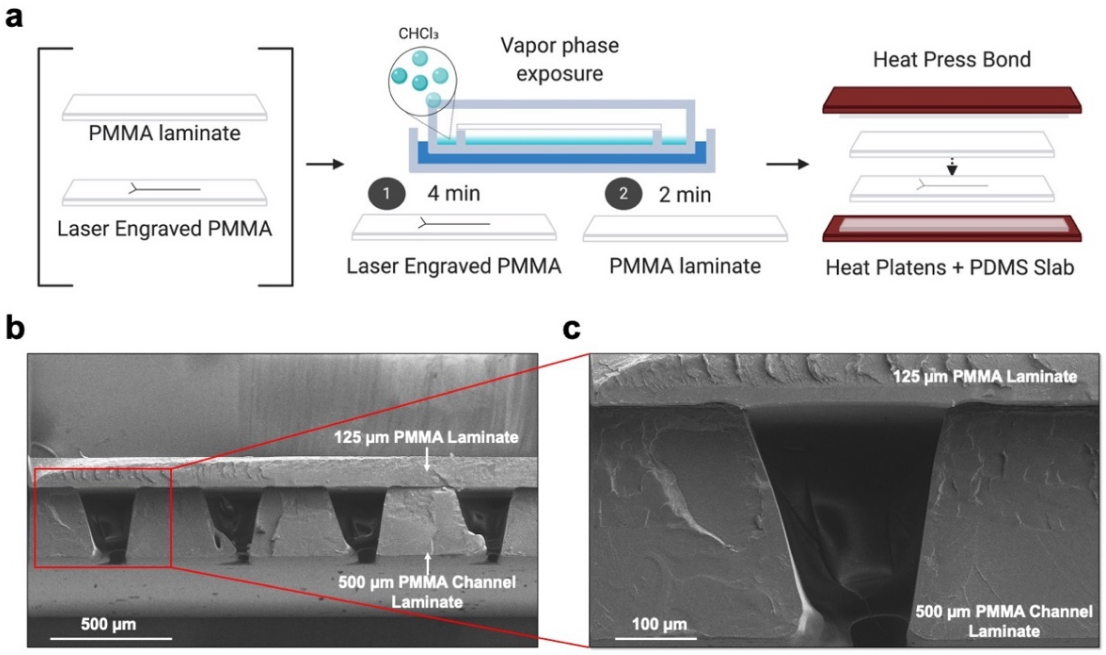

Figure 1.8 Vapor solvent bonding with pressure and heat

(a) Schematic of solvent bonding process facilitated by chloroform vapor exposure and thermal pressing. **(b,c)** SEM images of a 500-µm PMMA laminate with microchannels irreversibly bonded to a 125-µm PMMA laminate after chloroform vapor exposure.

We investigated solvent bonding of PMMA laser engraved laminates through chloroform vapor exposure with controlled pressure and temperature using a heat press (**Fig. 1.7a**). The combined temperature and pressure generate enough polymer flow at the interface to achieve

intimate contact, with interdiffusion of polymer chains between the surfaces leading to a strong bond. Under ideal conditions, the resulting bond strength can reach the cohesive strength of the bulk material. [76] As shown in Fig. 1.7a, we incorporated a ~1 mm PDMS slab to ensure an even distribution of heat and pressure during the bonding process.

We found that to successfully solvent bond any laser-cut microfluidic device, four conditions need to be optimized: 1) vapor/liquid solvent exposure time, 2) pressing force, 3) pressing temperature, and 4) pressing time. We established an initial baseline for each condition for our preliminary studies by following the protocols reported by Ogilvie et al. and Tsao et al.: 4-minute chloroform vapor exposure, followed by heat pressing at 120 – 200 psi and 60˚C for 5-20 minutes.[75,76] We previously reported the steps to find the optimal conditions to bond a 300 μm PMMA laser engraved substrate to a 125 μm PMMA laminate. After carefully examining each condition's impact through isolation, we were able to find the optimal bonding conditions.[68] For the design used in our study, we found that the vapor exposure was optimal when treating the 500 μm PMMA laser engraved laminate for 4 minutes and the 125 μm PMMA laminate for 2 minutes (one after the other). We left the 300 μm PMMA laminate outside in a closed vapor-free chamber while the thin laminate remained in solvent vapor exposure. Right after the 2-minute treatment, we manually bonded the two layers and then placed them in a heat press set at 60˚C and pressed at 140-160 psi for 5 minutes. Finally, we removed the bonded structure and left it to cool down. Depending on the design and selected thermoplastics, gradual cool-down to room temperature inside the press is also common to avoid stress cracks in the structure.[63] Figs. 1.7b&c, show SEM images of the two PMMA bonded laminates forming closed microchannels.

We found that each of these conditions is highly dependent upon the specific design characteristics of any given microfluidic device during our studies. Some key characteristics are

the thickness of the chosen PMMA laminates, the geometrical characteristics of the microfluidic chip architecture (e.g., surface area, channel dimensions), and the pressing surface area (heat-press characteristics). For example, an over-exposure to chloroform vapor and excessive pressure leads to microchannel collapse, usually observed as channel melting. Conversely, under-exposure to chloroform and low pressure leads to weak bonds. Therefore, finding the optimal solvent bonding is paramount for the successful fabrication of any microfluidic device. After defining the optimal solvent bonding conditions, the process becomes highly amenable to a multi-batch fabrication procedure.

1.3.6 *Track-etched membrane bonding to PMMA substrates*

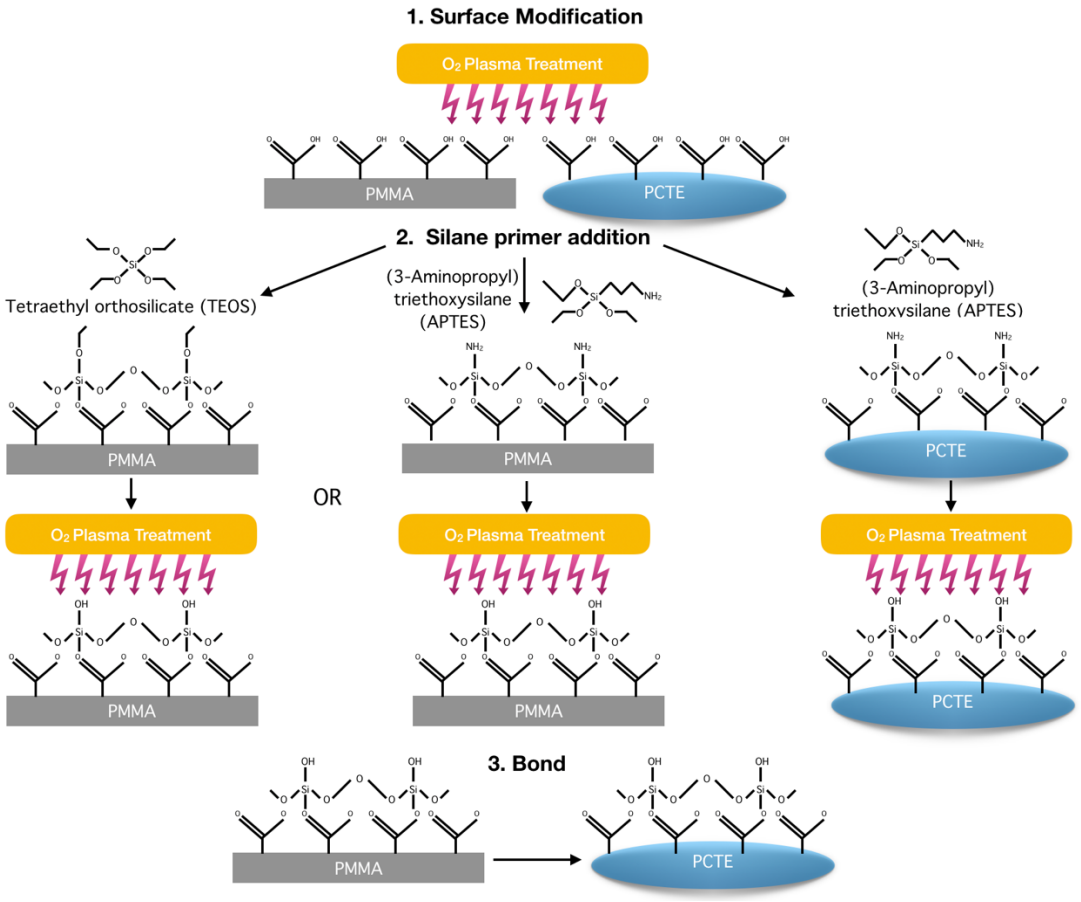

Figure 1.9 PCTE and TPU membrane bonding to PMMA substrates

Left and middle show silane primer addition to PMMA with TEOS or APTES, respectively. Right shows silane primer addition to PCTE membrane with APTES.

Next, we investigated the bonding of membranes to PMMA engraved laminates. We found that membranes made of PCTE/TPU can also be bonded to PMMA substrates using chemical/thermal bonding approaches. PCTE membranes can be bonded to PMMA through a silane primer surface modification (**Fig. 1.9**). Silane primer surface modification allows for the bonding of dissimilar polymer substrates such as PMMA and PC. [80–83] As shown in Fig.1.9, exposure of the PMMA and PCTE substrates to oxygen plasma results in converting a fraction of the polymer into carboxylic acid groups, making the surface more hydrophilic and facilitating the

addition of Si-containing groups. Through similar addition mechanisms, the ethoxy groups on tetraethyl orthosilicate (TEOS, 10% in 60% isopropyl alcohol) or (3-Aminopropyl) triethoxysilane (APTES, 5% in water) react with the carboxylic groups in plasma-treated PMMA and PCTE. Subsequent exposure to oxygen plasma converts the reactive ethoxy groups at the polymer surface into silanol groups. Siloxane (Si-O-Si) bonds are formed across the interface between the modified substrates after bonding. [80] The addition of PCTE membranes to a microfluidic device could form semi-permeable interfaces selective in particle size.

TPU membranes can be bonded to PMMA through thermal fusion bonding without chemical treatment. [84,85] Pourmand et al. demonstrated that the bonding of PMMA/TPU substrates was successful at a temperature of 130 °C and a vacuum pressure of 12 psi for one hour (**Fig. 1.10**). TPU membranes are highly flexible and have been used to fabricate whole-thermoplastic microfluidic functional elements, including a pneumatic (gas- actuated) normally closed microvalve, a micro-check valve, and a pneumatic dual-phase micropump (**Fig. 1.10 h-i**).[84]

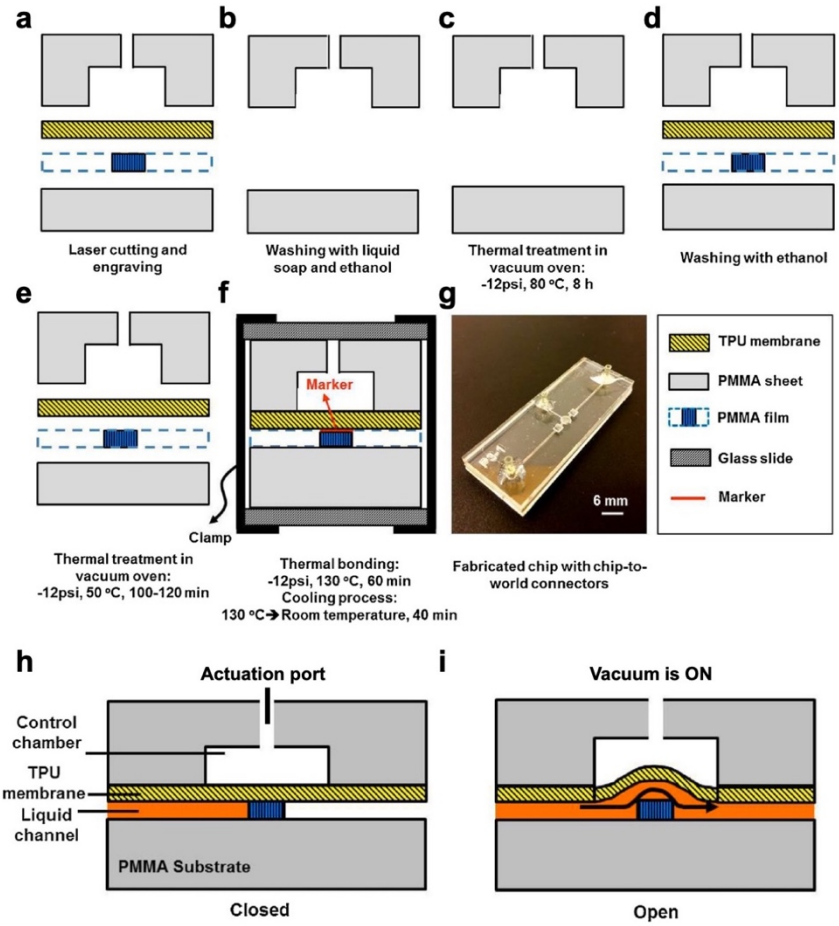

Figure 1.10 Schematic of TPU/PMMA fabrication process

(a) Laser cutting and engraving of PMMA specimens and TPU membrane; **(b)** washing with liquid detergent and pure ethanol; **(c)** thermal treatment of PMMA substrates; **(d)** washing with pure ethanol; **(e)** thermal treatment of all layers including membrane in vacuum oven; **(f)** marked using a marker, alignment, thermal bonding, and cooling down processes. **(g)** Photograph showing a fabricated chip with embedded micropump. Schematics of the operation of the valve, **(h)** open, **(i)** closed. *Adapted with permission from Pourmand et al.* [86]

1.3.7 *Transfer adhesive bonding*

We can categorize microfluidic bonding as either direct or indirect. Direct bonding methods, such as solvent bonding, are processes that do not require any additional materials to mate substrates. As shown previously, we distinguish these methods by their ability to produce

microchannels with homogenous sidewalls. On the other hand, indirect bonding involves using an adhesive layer to seal two substrates and encapsulate microchannels in one or both substrates. Indirect bonding methods require an intermediate adhesive that results in channel sidewalls with different chemical, optical, and mechanical properties than the bulk polymer. [76]

Adhesive bonding methods are well-known due to their simplicity for sealing thermoplastic microfluidic devices. An example of a simple method is liquid adhesives set through the evaporation of the solvent or epoxies and acrylates that cure (polymerize and crosslink) after mixing with a catalyzing agent.[76] There are a few successful examples of this method as a viable approach for polymer microfluidic bonding. The most common liquid adhesive bonding method relies on applying a thin layer of a high viscosity liquid adhesive, forming a bond after curing by UV light irradiation.[76,87–89] However, few published examples of this approach are likely due to microchannel clogging and the challenges associated with controlled application of liquid adhesives and prolonged curing steps. Moreover, the complexity of this process also presents a challenge for large-scale fabrication and commercialization.

Here we present an alternative and more straightforward method based on the use of double-sided transfer adhesive tapes. Transfer adhesive tapes usually are made of adhesive coats on both sides of a polyester film carrier. As shown in Fig.10, we attach a low surface energy adhesive tape to the polymer substrate before CO_2 laser ablation. The addition of the adhesive tape to the polymer before laser engraving/cutting eliminates challenges associated with alignment. For this process, it is critical to find the optimal power and speed settings required to remove the adhesive and polymer material to create microchannels effectively. After the laser cutting process, the substrates can be customarily cleaned and treated for optimal surface clarity and smoothness.

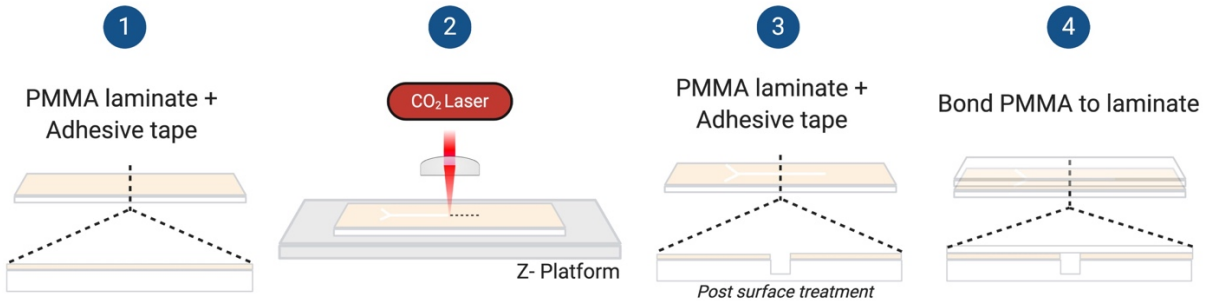

Figure 1.11 Schematic of transfer adhesive bonding fabrication process

The process consists of four steps: **(1)** applying/double-sided rolling transfer adhesive tape to PMMA laminate, **(2)** laser engraving/cutting, **(3)** post-processing surface treatments, and **(4)** bonding to clear PMMA laminate.

Notably, this process is highly dependent on the chosen polymer and the properties of the adhesive tape. We investigated the use of a variety of transfer adhesive tapes, including double-sided silicone/acrylic, acrylic/acrylic, silicone/silicone, high-strength 300 LSE (low surface energy) acrylic adhesive, and polyolefin double-coated thin tape bearing a pressure-sensitive poly(dimethyl)siloxane (PDMS) with PMMA as a substrate. We tested laser cutting performance, bond strength, and leakage when exposed in humid environments (e.g., inside an incubator).[68]

After testing all the adhesive tapes, we found that acrylic adhesives form the strongest bond with PMMA substrates, as expected. On the other hand, we found that silicone adhesives had a weak bond strength but still results in leak-proof microchannels in our designs. Notably, we found that 3M 300 LSE had the best performance, as it formed strong/irreversible bonds, which resulted in leak-proof devices. Finally, PDMS adhesive tapes resulted in an inferior optical quality when applied to PMMA substrates before laser ablation. PDMS-lined PMMA substrates resulted in high amounts of debris, which obstructed laser-ablated microchannels.

Based on our findings, it is essential to note that transfer adhesive tapes are highly recommended for bonding thick substrates where solvent bonding is not ideal or for early prototyping stages. We found that prolonged exposure to chloroform degraded the surrounding

adhesive coatings around the engraved microchannels. Overall, adhesives as an alternative bonding strategy are highly dependent on the design of the microfluidic device.

1.4 CONCLUSIONS

Combining the microfabrication processes outlined in this chapter should serve as a solution to overcome the barriers related to an organic translation towards large scale manufacturing and commercialization. By implementing DM and scalable processing techniques, there is more potential for widespread validation and commercialization of microfluidic technologies. Facilitating the prototyping stages through cost-effective, reliable, and automated fabrication technologies, such as CO_2 laser ablation, is fundamental for the rapid development of microfluidic devices. After finding the optimal design specifications, the CAD drawings are often translatable to a larger-scale fabrication process, such as injection molding.

As shown in the findings outlined in this chapter, each step of the fabrication process requires methodical calibration. Starting from a 2D CAD drawing, the optimal CO_2 laser ablation, back-end, and bonding processes are critical for successful and reliable microfabrication. After defining the essential conditions, fabrication becomes a rapid and straightforward process performed by any trained lab member. We expect that this chapter serves as a guide that facilitates fabrication and a reference for the development of microfluidic technologies. In the following chapters, we demonstrate applying the fabrication techniques shown through two distinct microfluidic platforms that focus on enabling functional testing of human, intact tissues for cancer research.

1.5 EXPERIMENTAL

1.5.1 *CO_2 laser micromachining*

The CO_2 laser system used (VLS3.60, Scottsdale, USA) has a wavelength of 10.6 μm and a maximum power of 30 W. We utilized AutoCAD 2017 for designs and optimized the power speed settings of the CO_2 laser to achieve specific widths and depths for the microchannels. For width/depth and vector/raster calibration studies, we utilized 1mm-thick CLAREX® PMMA sheets Astra Products, Baldwin, NY (11510103)). These sheets feature smooth-surface (roughness less than 0.02 μm), uniform thickness, high light transmission 92 - 94%, isotropic transmission, no double refraction, no retardation, and no autofluorescence.[90] Before laser cutting, we removed the protective liner.

1.5.2 *Back-end processing and solvent bonding*

After laser engraving/cutting, we rinsed the PMMA substrates with DI water and isopropyl alcohol and placed them in an IPA sonication bath for 5 minutes. After sonicating, we rinsed the substrates with DI water and dried them with nitrogen gas. Once the substrates were clean and without residual debris, we performed exposed the engraved microchannels to chloroform vapor to remove surface roughness and prepare for bonding. For chloroform vapor exposure, we filled a rectangular glass chamber with enough chloroform to fill the surface (~10mL) and placed it atop a room-temperature water bath. Before exposing the PMMA substrates to chloroform vapor, we leveled the chamber's surface, sealed the chamber, and left it to equilibrate for 5 minutes to ensure homogenous vapor exposure. We utilized ~6mm standoffs to place the substrate in the chloroform vapor chamber.

We exposed the engraved PMMA substrates for 4 minutes and the sealing layer for 2 minutes consecutively for solvent bonding experiments. After chloroform vapor exposure, we hand pressed the sealing layer onto the channel network layer to form a weak bond. Then, to ensure uniform bonding, we sandwiched the two layers between two ~3 mm thick PDMS slabs with the same outer dimensions as the channel network layer. Finally, we placed the whole ensemble in the heat press for 5 min between 120-160 psi at 60˚C. The chloroform vapor exposure times for both the engraved PMMA substrates and the sealing layers were found through an iterative process, previously reported. [68,69]

1.5.3 *SEM imaging*

We took scanning electron microscopy (SEM) images of the laser cut PMMA channels to evaluate the channels' topological changes due to chloroform exposure and the dimensions of the channels (roofless and sealed). We prepared the samples by rinsing with DI water, sonicating with IPA for 2 min, and rinsing with DI water again. We utilized nitrogen gas to remove excess water and left the samples dry overnight. To image microchannel cross-sections, we prepared substrate samples through a freeze-fracture process involving immersion in liquid nitrogen. Finally, before SEM observation, we coated all samples with a thin, 19.5 nm-thick film of Au-Pd to prevent charging.

1.5.4 *Membrane and transfer adhesives tape bonding*

We utilized 25 mm diameter hydrophilic polycarbonate (PCTE) membranes with a 14.0 µm pore size (PCT14025100, Sterlitech, for our membrane bonding preliminary investigations Kent, WA). We bonded the PCTE membranes with thermal fusion bonding by pressing for 5 min between 120-160 psi at 60˚C. For TPU membrane bonding, we found that Prochimir IRT3

membranes are the most suitable for thermal fusion bonding.[85] These membranes feature a melting range between 145-160˚C and a minimum thickness of 15 μm while being highly breathable. Zhang et al. demonstrate TPU-PMMA bonding using a thermal fusion bonding process at a temperature of 130 ◦C and a pressure of 12 psi for one h, and then they were cooled down gradually from 130 ◦C to room temperature in 40 min.[85] Apart from these two processes, the chemical processes suggested (APTES and plasma) remain untested.

For transfer adhesive tape bonding, we utilized double-sided silicone/acrylic(SA1020, Adhesive Applications, Easthampton, MA), double-sided acrylic/acrylic (A100, Adhesive Applications, Easthampton, MA), Low Surface Energy Acrylic Adhesive (300LSE, 3M, St. Paul, MN), polysil double-coated silicone adhesive tape (S1001-1DC11, Adhesive Applications, Easthampton, MA), and polyolefin double-coated thin tape bearing a pressure-sensitive poly(dimethyl)siloxane (PDMS) with PMMA as a substrate. We manually bonded the adhesive tapes to the PMMA substrates using a roller for uniform bonding. We tested laser cutting performance, bond strength, and leakage when exposed in humid environments (e.g., inside an incubator).[68]

Chapter 2. A MICROFLUIDIC PLATFORM FOR FUNCTIONAL TESTING OF CANCER DRUGS ON INTACT TUMOR SLICES

2.1 ABSTRACT

Present approaches to assess cancer treatments are often inaccurate, costly, and cumbersome. Functional testing platforms that use live tumor cells are a promising tool for drug development and identifying optimal therapies for a given patient, i.e., precision oncology. However, current methods that utilize patient-derived cells from dissociated tissue typically lack the tumor tissue's microenvironment and cannot inform on a timescale rapid enough to guide patient-specific therapy decisions. We have developed a microfluidic platform that allows for multiplexed drug testing of intact tumor slices cultured on a porous membrane. The device is digitally manufactured in a biocompatible thermoplastic by laser-cutting and solvent bonding. Here we describe the fabrication process in detail, characterize the device's fluidic performance, and demonstrate on-device drug-response testing with tumor slices from xenografts and a patient colorectal tumor.

2.2 INTRODUCTION

Tumor-derived slice cultures contain and sample the original tumor’s content and 3D structure, including ECM, non-tumor stromal cell types and biochemical pathways.[91–93] The implication of various cellular (e.g., fibroblasts, lymphocytes, macrophages, and endothelial cells), matric and metabolic components of the tumor microenvironment as drivers of drug responsiveness highlights the importance of retaining these elements in a preclinical screening platform. (17-18). Organotypic slice cultures have demonstrated the ability to closely resemble the

TME architecture and allow for drug metabolism and toxicity studies in brain,[94] liver,[95–97] lung,[97,98] kidney,[97,99] and intestine[95] tumor slices. Drug testing has been performed on slice cultures from multiple tumor types including brain, breast, GI, skin, and pancreas tumors. [91,92,100–102] Slice cultures have the potential to improve functional drug screens by allowing the rapid testing of different potential therapies. For example, drug testing of slice cultures from PDX or from primary tumors has been shown to correlate with treated responses in patients with pancreatic[102] and breast cancers.[103] However, in most studies with slice culture, therapies are uniformly applied to the slice. As the number of slices per tumor is limited, the numbers of conditions that can be tested is limited. Patient-derived clinical samples provide a unique tool to explore the susceptibility of individual tumors to specific therapies. The combination of microfluidic drug delivery with slice culture has the potential to enable multiplexed drug delivery and response assessment while preserving the native microenvironment and tissue microarchitecture. Various microfluidic devices have been developed to study intact tissues such as brain slices, [36,104,105] pancreatic islets,[106–109] adipose tissue,[109–112] intestinal tissue,[113,114] lymph node slices,[115,116] liver slices[117–119] and biopsies[120], testis tissue,[121] and ovarian explants.[122]

We have developed a microfluidic platform for high-throughput chemosensitivity testing on individual slice cultures.[31,32,36,37] Our platform has the potential to identify a subset of therapies of most significant potential to individual patients on a timescale rapid enough to guide therapeutic decision-making. Using our platform, we have evaluated drug responses with U87 GBM xenograft tumors and showed similar and reproducible response profiles on and off the device.[123] This new method should test treatment sensitivity on the patient's tumor tissue to direct a physician's therapeutic strategy. Additionally, our platform can provide a critical missing link between drug

testing in cell or animal models by testing new drug candidates in patient-derived cancer tissue in the early development stages.

Previously, we prototyped the platform by molding in polydimethylsiloxane (PDMS), i.e., by soft lithography.[36] However, PDMS is not adequate for drug-based studies; both absorption into PDMS[46] and adsorption onto PDMS[53] can potentially alter experimental outcomes by changing the target concentrations and by partitioning molecules in undesired regions of a microfluidic device. PMMA features less drug absorption than PDMS, although it can still adsorb drugs on its surface.[118] Furthermore, our early PDMS prototype involved more than two days of highly-skilled fabrication per unit, so it was not readily translatable for large-scale fabrication for widespread adoption. We explored the 3D-printing of PDMS as a possible manufacturing solution,[124] but the printed elastomer is virtually identical to Sylgard 184, so it does not address the drug binding problems; we have also demonstrated high-resolution 3D-printing in inert, biocompatible resins,[125] but limitations in the build size of commercial 3D-printers prevented its use in this application.

Here we report a thermoplastic version of the platform made entirely in poly (methyl methacrylate) (PMMA) by digital manufacturing based on CO_2 laser micromachining. PMMA has been widely used to build microfluidic devices for biomedical applications because it is biocompatible, has excellent optical transparency, low gas permeability, and is less expensive than PDMS.[63,126,127] Compared to conventional photolithography and soft lithography methods, digital manufacturing shortens the design and processing time, streamlines assembly, and reduces manufacturing costs. This manuscript reports a detailed description of the complete fabrication process, including CO_2 laser optimization for microfabrication, post-processing, and solvent bonding techniques for assembly, as well as measurements of diffusion between and above channels using the device. We demonstrate the platform's functionality by multiplexed delivery of

anti-cancer drugs onto glioblastoma multiforme (GBM) xenografts and patient-derived colorectal cancer (CRC) tumor slices. We further demonstrate the device's versatility with an expanded drug treatment panel, multiple types of fluorescent cell death indicators, and real-time measurements using the device. **Most of the work presented in this chapter has been adapted with permission from two of our most recent publications in Lab on a Chip*[32] *(The Royal Society of Chemistry) and Nature Precision Oncology*[31] *(Springer Nature) .**

2.3 Results and Discussion

2.3.1 *Microfluidic Device Design*

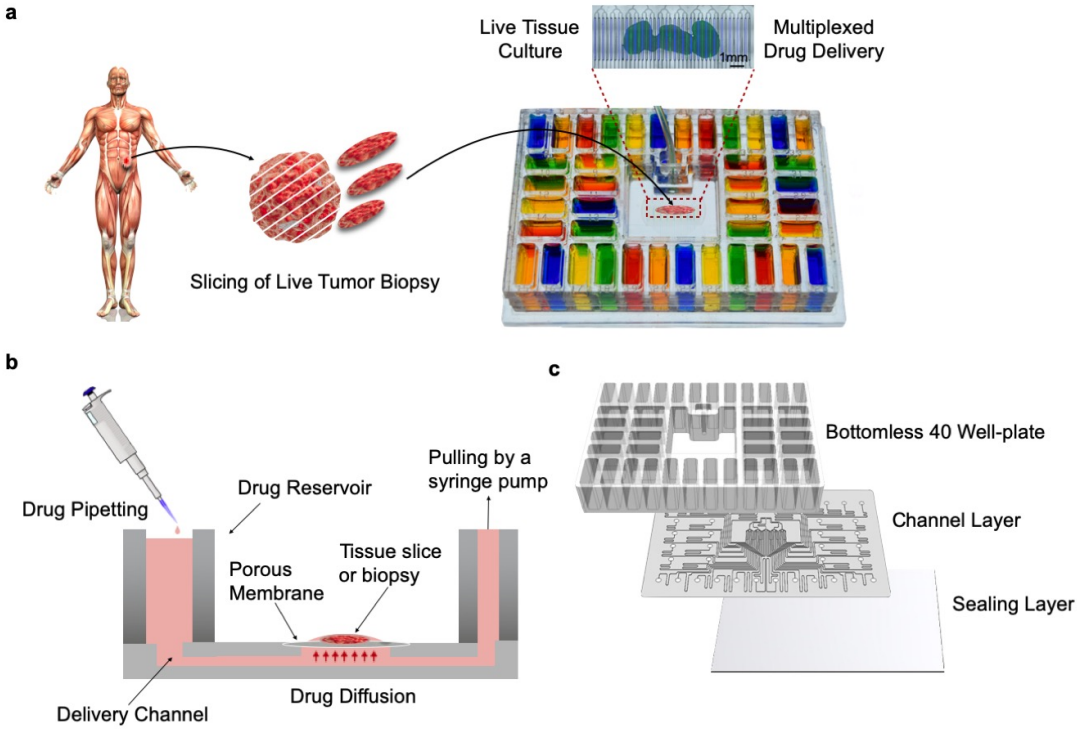

Figure 2.1. Microfluidic device design overview.

(a) Proposed application and device functionality. Micrographs of a mouse glioma tumor slice exposed to two different cell nuclear binding agents (Hoechst, blue, and Sytox Green, green) through alternating streams. **(b)** Cross-sectional schematic of the device. The device operates by gravity flow, and a syringe pump drives the total flow

rate through a common outlet: one syringe pump controls flow across all 40 fluidic streams. Tissue slices are cultured on a PTFE porous membrane. The wet membrane seals the roofless microchannels by capillarity, which allows for fluidic stream transport of culture medium to tissue. **(c)** The PMMA platform's explained schematic shows from top to bottom: 1) bottomless plate with 40 inlet wells, 2) 300μm-thick channel network layer, and 3) 125 μm-thick sealing layer.

Our patented[37] platform permits regioselective delivery of drugs with spatiotemporal control on live tissue slice cultures (**Fig. 2.1a,b).** The platform consists of three functional components, as well as a lid and a base. From top to bottom, these components are: 1) a 40-well plate with a central culture area, 2) a microfluidic channel network layer, and 3) a sealing layer for the bottom surface of the channel network (**Fig. 2.1c, Suppl. Fig. 2.1**). We fabricated the device using a combination of CO_2 laser micromachining and solvent bonding techniques. After optimizing both techniques, we irreversibly bonded all the PMMA components to produce a leak-proof platform.

The microfluidic platform consists of 40 microchannels connecting to a central tissue culture area for drug delivery. Upstream of the central area, each microchannel is individually connected to a different reservoir well of the 40 well-plate, containing a drug. Downstream of the delivery area, all the microchannels are connected to a common outlet via binaries. Initially "roofless," the delivery microchannels are separated by 250 μm-thick PMMA walls, designed to sit underneath a PTFE porous membrane. Placement of a wet PTFE porous membrane onto the roofless microchannels causes the membrane to adhere to the surface through capillary forces; the membrane becomes the "roof" for the roofless microchannels. (We note that it is possible to generate flow in roofless microchannels by applying positive pressure at the inlet,[128,129] but here we wished to generate flow by suction through the outlet, so adding a roof provides a zero-flow constraint and forces flow from the inlets.) Application of negative pressure at the outlet causes a slow flow under the membrane, increases the PTFE membrane adhesion to the PMMA surface to

"seal" the channel, and allows for the diffusive supply of different reagents to the tissue in different channels. Equal microchannel resistances, achieved by having equal microchannel lengths and curves across the whole architecture, result in equal flow across microchannels (**Suppl. Fig. 2.1**) and Flow Characterization section below). Constant CO_2 laser power and speed create microchannels with uniform width and depth. However, small imperfections in the channels occur due to the stochastic nature of laser melting and tracking errors in the mechanisms that move the laser.

The platform allows for live tissue culture and high-density delivery of up to 40 different solutions. Live tumor slices are cultured on top of the porous membrane that forms the open microchannels' roof in the device's central culture area. A 1.6 mL reservoir feeds each microchannel. With a flow rate of 1 mL/hr, each well could provide up to ~64 hr of uninterrupted reagent delivery. To operate the device, the user fills the reservoirs of the 40 well-plate and activates flow with a syringe pump connected to the outlet of the device. Solutions move through the channels on the bottom surface and then diffuse upwards through the membrane into the tissue (**Fig. 2.1b**). The platform is easy to transport, and the clear plastic and well-plate footprint make the device compatible with standard imaging systems.

The interfacing of microfluidics with Transwell inserts has allowed for manipulating the basal surface of cells in culture[130] and represents a very intuitive approach to cell-based microfluidics. Our device can also be adapted to facilitate the transfer of cultured tissue onto the device from Transwell inserts (**Fig. 2.2a**), made of the same porous membrane that we use for the platform. After manually removing the ~2 mm feet at the bottom of the insert, we can directly place the entire Transwell into the device (**Fig. 2.2b**). Figures. 2.2c, d live dye labeling of a U87 GBM xenograft slice with Cell Tracker dyes and the nuclear dye Hoechst.

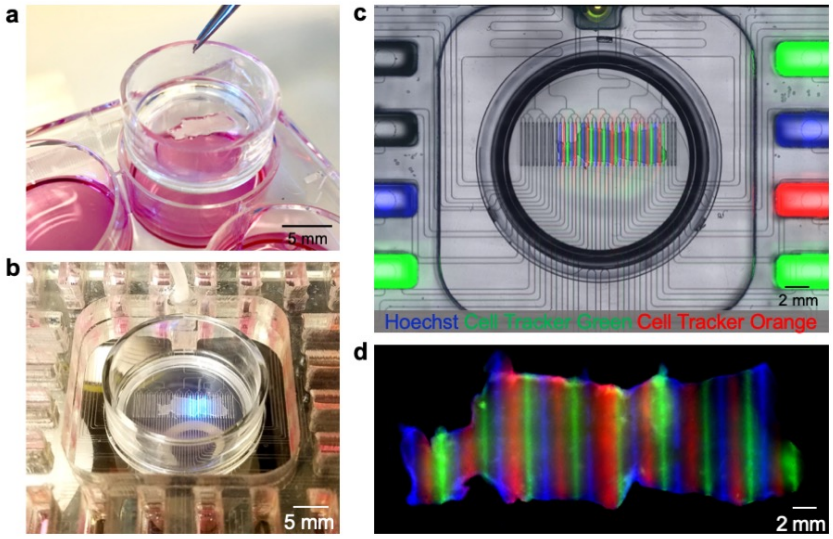

Figure 2.2. Microfluidic device with transwell insert

(a) Photograph of a standard six-well plate with Transwell insert containing U87 GBM flank xenograft slices**. (b)** Live imaging with the platform with incorporated Transwell insert. **(c)** Fluorescent image showing microfluidic delivery of Hoechst (blue), Cell Tracker Green (green), and Cell Tracker Orange (red) to live GBM slices. **(d)** Fluorescent image showing fixed tissue 48-hours after delivery.

2.3.2 *Microfluidic device fabrication through CO_2 micromachining*

Fabrication of each device's components required extensive CO_2 laser calibration to achieve the desired dimensions and microfluidic architecture. The platform's fabrication process consisted of CO_2 laser micromachining, post-ablation processing, thermal fusion, solvent bonding, hydrophilization, and sterilization (**Fig. 2.3**). We optimized the power and speed settings of the CO_2 laser for the fabrication of each platform component. For the microfluidic channel network, we determined different optimal CO_2 laser power and speeds for each specific width and depth of the closed microchannels, roofless delivery channels in the central tissue culture area, and the binary network channels that lead to a single outlet. A total of 40 microchannels, engraved onto a 300 µm-thick sheet of PMMA, lead to 40 parallel roofless delivery channels. The creation of the

roofless delivery channels required multiple, shallow engravings in an iterative process to prevent polymer reflow. We found that high-power laser ablation to create microchannels with a high depth-to-width aspect ratio led to polymer reflow, resulting in channel occlusion/collapse.

Additionally, high laser powers induced thermal stresses that warped the walls of the roofless delivery channels. Engraving and cutting the channel network layer took 7 min while cutting the sealing layer took less than a minute. After successfully calibrating the laser system, we could generate a digital and easily reproducible protocol to fabricate all the device components.

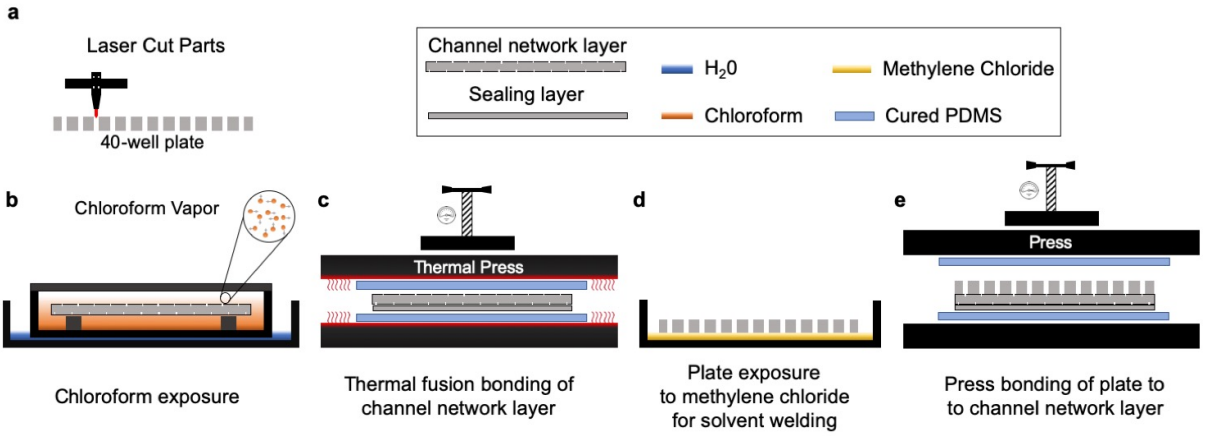

Figure 2.3. A general overview of device fabrication protocol.

The overall fabrication of the device consists of **(a)** laser cutting/engraving and cleaning each of the laminates that compose the microfluidic platform (30 min); **(b)** chloroform vapor exposure (6 min); **(c)** thermal fusion bonding (5 min); **(d)** solvation of the under-surface of the 40-well plate with methylene chloride (1 min); **(e)** alignment and assembly by pressing (5 min); and outlet/base installation (10 min, step not shown).

The 40-well PMMA plate's fabrication is subjected to very different manufacturing constraints because it is thicker (2.5 cm-thick,) and high resolution is not needed. To cut through the full thickness of ~2.5 cm thick PMMA, we utilized a more powerful CO_2 laser system (wavelength of 10.6 μm and a power of 150 W). We performed multiple passes at maximum power

and minimum speeds to create smooth through-cuts to create the well plate wells. Each pass had varying laser speeds from high-to-low to gradually cut through the PMMA thickness, from shallow to deeper cuts. The complete cutting process of the 40 well-plate took about 15 min. Alternatively, to streamline this process, we found it is more cost-effective to order the well plate from a CNC machining service (Nanchang Inte. Industrial Co., Ltd., ~$5/unit).

2.3.3 *Post Processing and Bonding*

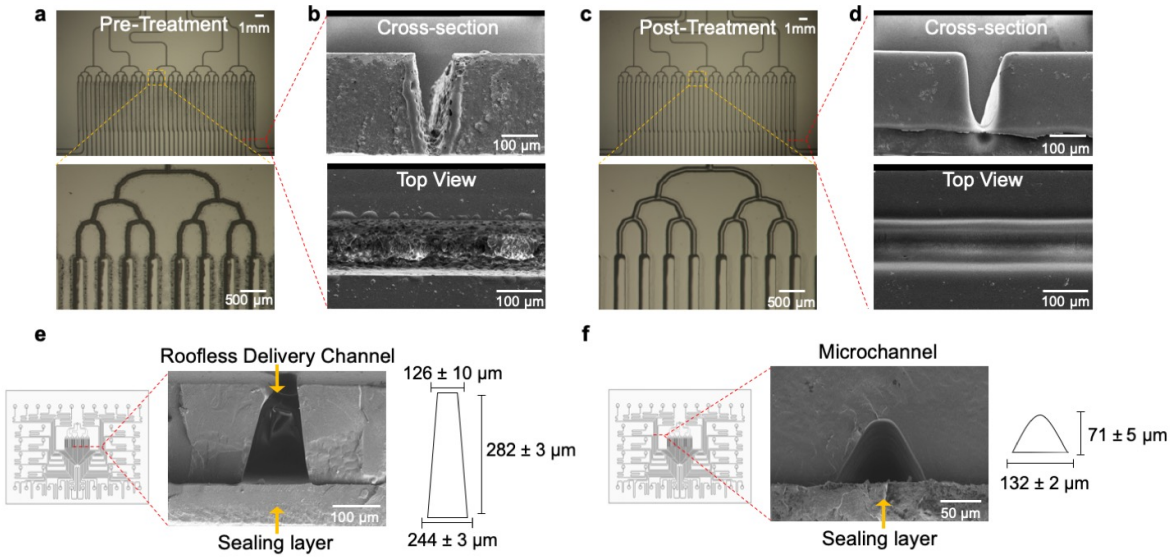

Figure 2.4. Smoothing of microchannel features by chloroform exposure

(a) Micrographs of the channel network layer before exposure to chloroform vapor. The channels have poor optical clarity, as evidenced by the darkness of the channels. **(b)** SEM images of the cross-sectional view and top view of channels after being engraved by laser micromachining. The channels have a rough, porous structure and bulge around the channel rims. **(c)** Micrographs of the channel network layer after exposure to chloroform vapor. The channels have increased optical clarity since more light penetrates through the channels. **(d)** SEM images of the cross-sectional view and top view of the channels after being exposed to chloroform vapor. The channel profile becomes smoother after exposure to chloroform. **(e)** SEM of the cross-sectional view of the roofless/delivery microchannels. The roofless delivery channels have a trapezoidal shape where the opening facing the sealing layer is 244 ± 3 µm wide, the opening facing the membrane and tissue sample is 126 ± 10 µm wide, and the depth is 282

± 3 μm. **(f)** SEM of a sealed microchannel. Solvent bonding with chloroform vapor exposure and thermal pressing yields sealed microchannels. The micromachined laser channels have a curved shape with a width of 132 ± 2 μm and a depth of 71 ± 5 μm.

To improve the device's optical clarity and surface smoothness, we performed a series of post-processing steps. Laser machining with CO_2-based systems is known to introduce manufacturing defects and loss of clarity of polymer substrates during fabrication. However, exposure to solvent vapors removes these defects (**Fig. 2.4a-d**).[75] The method developed by Ogilvie et al. utilizes chloroform vapor.[75] Chloroform is an optimal solvent for surface treatment. Modification of PMMA and direct exposure of chloroform vapor improves optical clarity, reduces surface roughness, and enhances bonding to other PMMA substrates. DeVoe et al. studied ideal solvents for surface modification and solvent bonding of PMMA microfluidic substrates based on the Hildebrand solubility parameter, a measure of the cohesive molecular forces for both solvent and solute.[131] If the cohesive forces for each material are similar, their molecules can readily co-exist, and dissolution of the solute will occur.[76,131] PMMA has a solubility parameter of 20.1 $(J/cm^3)^{1/2}$, while methylene chloride and chloroform have solubility parameters of 20.2 $(J/cm^3)^{1/2}$ and 18.7 $(J/cm^3)^{1/2}$, respectively, making them ideal solvents for strong, cohesive molecular forces.[76,77] Before assembly, we exposed the channel network layer and the 40 well-plate to chloroform to remove rough/porous structures. We selected chloroform as the solvent for surface treatments based on its reported success by other groups.[75,132] However, in principle, methylene chloride would also be an ideal solvent for PMMA surface treatments due to the similarity between its Hildebrand parameter and that of chloroform. During chloroform vapor treatments, a thin layer on the surface of PMMA presumably became dissolved by the vapor, which induced polymer reflow and allowed PMMA to spread out evenly.[75] As shown in Figs. 2.4c,d, chloroform vapor treatment

created a smooth surface, resulting in an optically-clear PMMA surface. This process also removed the bulges around the laser-engraved microchannels' rims and prepared the channel network layer for bonding with the sealing layer.

We followed previously reported thermal fusion bonding and solvent bonding techniques (**Fig. 2.3b-e**).[75,76] These two bonding methods are widely used to create closed microchannels in thermoplastic substrates due to relatively high bond strengths and overall simplicity of approach.[76] We exposed the channel network and sealing layer to chloroform vapor followed by thermal fusion bonding. This process resulted in leak-proof and smooth microchannels with optical clarity. The width of the roofless delivery channels on the side that faces the porous membrane and the tissue sample was 126 ± 10 μm (**Fig. 2.4e**). The microchannels had a curved profile with a base width of 132 ± 2 μm and a height of 71 ± 5 μm (**Fig. 2.4f**). To complete the assembly, we bonded the sealed channel network to the 40 well-plate by solvent bonding. We briefly immersed the bottom of the 40-well plate in methylene chloride to solvate the bonding surface (**Fig. 2.3d**). For this step, we utilized methylene chloride instead of chloroform; the Hildebrand solubility parameter of methylene chloride is closer to PMMA than that of chloroform,[76] and it showed enhanced solvation of the bonding surface of the well-plate. After removing the excess solvent, we immediately bonded the well plate to the channel network with a press at room temperature (**Fig. 2.3e**). We believe that the compatibility of these bonding techniques with CO_2 laser cutting/engraving augments the device's potential to scale from laboratory prototyping to commercialization.

After assembly, the device required a hydrophilization treatment because the surface of PMMA is hydrophobic. The native surface's contact angle is high (83°) and results in a resistive flow within the device's microchannels.[80,133] Oxygen plasma treatment has shown to reduce the contact angle (~45°), causing the PMMA surface to be more hydrophilic and facilitating the microfluidic

flow within the channels.[133] Therefore, after assembly, we treated the assembled platform with oxygen plasma for hydrophilization followed by UV for sterilization.

2.3.4 *Flow Characterization*

We performed a flow assessment analysis to determine uniformity across the device's 40 microchannels for any given batch of devices. We characterized the flow distribution across multiple devices operated at 1.5 mL/hr (37.5 µL/hr/well) and observed an average flow rate of 40.6 ± 0.6 µL/hr/well with an average coefficient of variation of 12 ± 4% (**Suppl. Fig.2.2**). We attribute the discrepancy to the small imperfections during CO_2 ablation and thermal bonding.

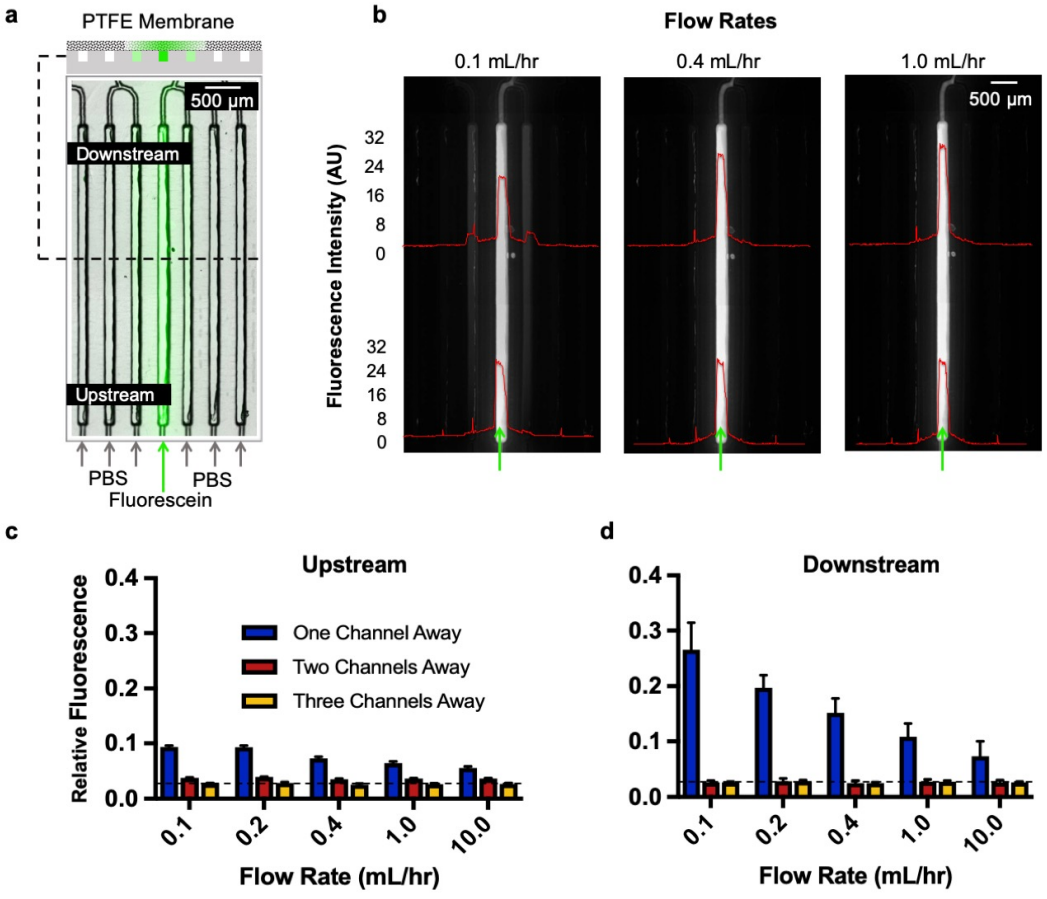

Figure 2.5. Lateral diffusion assessment using fluorescein.

(a) Delivery schematic of 100 mM fluorescein across six of the 40 delivery channels, with the rest having PBS. We intentionally isolated each of the six delivery channels by six channels to analyze spread three channels over on both directions when possible, as shown in the top cross-section schematic. **(b)** We took fluorescent images at 0.1, 0.4, and 1 mL/hr to show overall diffusion profiles upstream and downstream of the delivery channels and adjoining channels. **(c)** Upstream and **(d)** downstream measure of the relative fluorescence showing lateral spread one, two, and three channels away from the delivery channel.

We also investigated the molecular transport through the membrane using fluorescein. We chose fluorescein because its molecular weight (MW, 332 g/mol) is similar to the MW of small-molecule cancer drugs. We were specifically interested in understanding how the permeable PFTE membrane may affect the lateral spread of dye. The device operation begins when a porous PTFE membrane (with tissue on top) seals the roofless channels in the central culture area. This PTFE membrane is a 40 μm-thick fibrous meshwork with a functional pore size of 0.4 μm and porosity of 0.75. Thus, this highly porous membrane allows for lateral and vertical diffusion and potentially allows for some flow as well. With our previous PDMS prototype,[36] we determined that selective drug delivery is enhanced by alternating drug delivery channels with buffer channels. The delivery channels act as a source, and their adjacent channels act as concentration sinks that prevent lateral spread between delivery channels. However, our PMMA device has substantial alterations in the channel dimensions and inter-channel distances concerning our previous PDMS device; hence we needed to study the operating parameters under which we can confidently assert the absence of crosstalk between delivery channels. We investigated lateral diffusion at seven different flow rates to establish the minimum flow rate at which the device can be safely utilized without contaminating adjacent delivery channels. We sealed the roofless channels with a PTFE membrane and ran 100 mM fluorescein across 6 of the 40 delivery channels, with the rest having PBS (**Fig.**

2.5a). We analyzed the lateral diffusion one, two, and three channels away from the delivery channels with this arrangement.

Our experiments suggested that flow penetrates at least some portion of the porous membrane since the observed lateral diffusion (visible as the amount of fluorescence in adjacent channels) scaled with fluid velocity (**Fig. 2.5b**). This observation was consistent with some flow entering the membrane. There is less time for diffusion at higher flow velocities, and at lower velocities, there is more time for diffusion to occur. As a result, the lateral diffusion was higher downstream of the delivery channel than the middle and upstream locations. Our results indicated minimal fluorescein signal on the first channel adjacent to the delivery channel with flow rates above 0.4 mL/hr.

Similarly, the signal two and three channels adjacent to the delivery channel was minimal and barely visible at flow rates above 0.4 mL/hr. However, we have no evidence that the flow lines entering the bottom of the membrane reach the top of the membrane where flow could contact the tissue. These results are consistent with the results we obtained with our previous PDMS device,[36] with similar velocities but higher flow rates given the larger cross-sectional area in the PMMA device.

To quantify the lateral spread from the delivery channels, we analyzed three regions of interest (upstream, middle, and downstream) at the delivery channels and adjacent channels (3 on each side). Our results indicated minimal spread upstream of the channels compared to downstream (**Fig. 2.5c, d**). The baseline (dotted line) is established as the average fluorescence three channels away from the delivery channel at the highest flow rate (upstream and downstream). At 0.1 mL/hr, the slowest flow rate tested and the maximum spread, there was 13.0 ± 1.5% fluorescence one channel away (sink) relative to the delivery channel's average fluorescence. There

was 0.8 ± 0.1% relative fluorescence two channels away for flow rates above 0.4 mL/hr. We reached baseline spread (± 0.1%) for flow rates above 0.4 mL/hr at locations three channels away from the delivery channel. With these experiments, we concluded that the device should operate at a flow rate above 0.4 mL/hr for minimized crosstalk; and that a buffer channel should be used between drug delivery channels for selective drug delivery. Thus, the microfluidic device should have no significant cross-contamination between delivery channels when utilized with alternating drug/buffer (source/sink, 20 each) channels at a flow rate of 0.4 mL/hr or higher. In principle, for other drug-testing experiments that do not require buffer lanes, such as dose-response studies, drugs could be placed adjacent to each other to generate drug response curves.

2.3.5 *Live tissue vertical diffusion assessment*

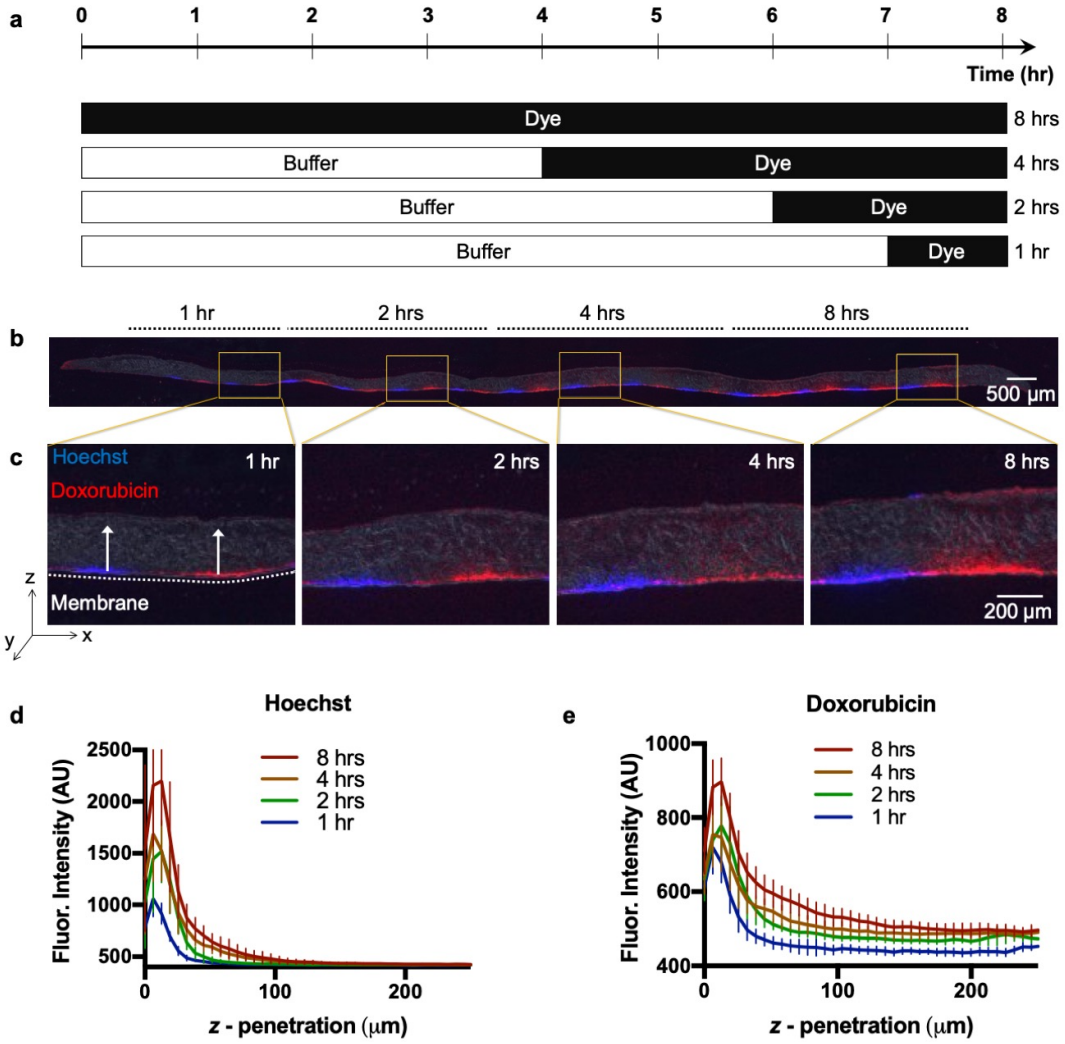

Figure 2.6. Vertical diffusion into U87 xenograft tumor slice.

(a) Schematic of timed delivery of Hoechst and Doxorubicin. **(b)** U87 tissue section (10 µm-thick) after 1, 2, 4, and 8 hrs Hoechst (blue) and Doxorubicin (red) exposure. **(c)** Section magnification of exposed areas. **(d)** Intensity profiles showing Hoechst. **(e)** Doxorubicin tissue z-penetration for each time point (n=8, per time point). Ave ± SD.

Next, we used fluorescent dyes to demonstrate how our microfluidic device can achieve temporal and regioselective drug delivery. In these experiments, we characterized the vertical diffusion of fluorescent compounds to understand how compounds diffuse into the tissue as a

function of time. We used Hoechst, a blue-fluorescent DNA stain, and Doxorubicin (DOX), a red-fluorescent chemotherapy drug. After seven days in culture, we transferred live, 250 μm-thick U87 GBM xenograft tumor slices to the device's culture area. Next, we selectively delivered Hoechst and DOX stripes to the tumor slices for varying periods (**Fig. 2.6a**). The fluorescent compounds were alternated as their fluorescent signals do not overlap, yielding the equivalent of a buffer lane in between for each compound. The compounds were added at different time points while the device was in continuous operation; all of the wells were initially filled with slice medium. We exposed different tissue regions on the same device experiment for 1, 2, 4, or 8 hrs beginning that number of hours before the end of the experiment. We replaced the slice medium with the fluorescent compounds in the selected delivery wells at the corresponding time points. Fig. 2.6b illustrates a 14 μm tissue cross-section at the end of the experiment and the resulting delivery of Hoechst (blue) and DOX (red) at all periods. As expected, fluorescent penetration (z-axis) increases with prolonged exposure times (**Fig. 2.6c**). We quantified penetration depth (**Fig. 2.6d, e**) with a vertical profile. Our results indicated a significant increase in vertical diffusion into the tissue over 8 hrs of exposure for both Hoechst and DOX. Compared to Hoechst, DOX had an increased observable z-penetration, including beyond ~200 μm in 8 hrs. The narrower profile of the Hoechst curve likely reflects the fact that Hoechst fluorescence represents only the dye bound to DNA and not free dye, while DOX fluorescence represents all dye (both bound and free).

Mass transport modeling can provide a quantitative framework for optimizing device design, determining assay times, and interpreting experimental data. To quantitatively describe the transport of the drugs/dyes within the tissue, we estimated their effective diffusion constants (D) using the experimentally obtained vertical fluorescent profiles of the dye/drug at different time-points (**Fig. 2.6d, e**). Assuming that the transport of the dye/drug is primarily driven by passive

isotropic diffusion, we can estimate D by applying Fick's second law of diffusion (Eqn. 1 in the Methods section). For our analysis, we discarded the fluorescence data from the 10 μm section of the tissue adjacent to the membrane, since some of the dye gets removed from the tissue surface during the washing steps post-staining. We fitted a sixth-order polynomial curve to determine the drug/dye concentration at the membrane surface. We then used linear interpolation of the experimental data to find the characteristic length (L) for each time-point (as defined in the Methods section). The value of D can be extracted independently from the four different time-points (1, 2, 4, and 8 hrs), and in a purely diffusive transport process, the D values should be the same for all time points. However, the estimated diffusion constant of Hoechst was 3.5×10^{-14} m^2/s, and that of DOX was 5.4 x 10^{-14} m^2/s at 1 hr, whereas the values decreased monotonically until they reached values at 8 hrs of 0.7×10^{-14} m^2/s and 1.3×10^{-14} m^2/s, respectively (see Table 2.1 for all the values). This monotonic decrease indicates that a simple Fickian diffusion model might not adequately or accurately describe the drugs' transport in the tissue. The drug's binding or adsorption to the tissue matrix and cellular materials (DNA, proteins, lipids) can slow down the diffusive transport over time. Also, tissue-surface evaporation can directionally drive the convective transport of the drugs through the tissue.

Furthermore, the tissue itself can biologically evolve – interaction with the drugs can alter its porosity and binding characteristics. A more realistic model would have to include binding reaction kinetics and convective flow through porous media. It should be straightforward to use finite-element modeling and analysis to simultaneously solve the convection-diffusion and binding kinetics equations and perform a parameter sweep and iterative curve-fitting to estimate the physical constants from the experimentally obtained drug concentration data.

Table 2.1 Diffusion Constant Values

Time (hr)	$D_{Hoechst}$ (m^2/s)	$D_{Doxorubicin}$ (m^2/s)
1	3.52×10^{-14}	5.41×10^{-14}
2	2.09×10^{-14}	5.89×10^{-14}
4	1.57×10^{-14}	2.45×10^{-14}
8	6.93×10^{-15}	1.26×10^{-14}

Diffusion constant values (D) for Hoechst and doxorubicin were estimated (based on Eq. 2.1) using the experimentally obtained vertical diffusion profiles (Fig. 6) of the molecules in the U87 xenograft tumor slice at 1, 2, 4, and 8 hours.

2.3.6 *Live imaging of multiplexed drug responses in GBM xenograft slices on device*

In vitro functional tests on an individual's cancer (e.g., live tissue from a biopsy) could help to predict that patient's outcome, even without any molecular knowledge.[9] Key improvements for these functional drug response assays would be real-time live tissue imaging and multiple orthogonal readouts that would reveal different temporal effects and action mechanisms. As shown in Fig. 2.7, a total of 40 different reagents can be used in the microfluidic platform. After delivery, the areas of exposure can be identified within the tissue using pan-nuclear stains such as Hoechst. Similarly, drug response analyses can be made with fluorescent viability markers, such as Sytox Green/Cell Event, or through conventional histological H&E and IHC.

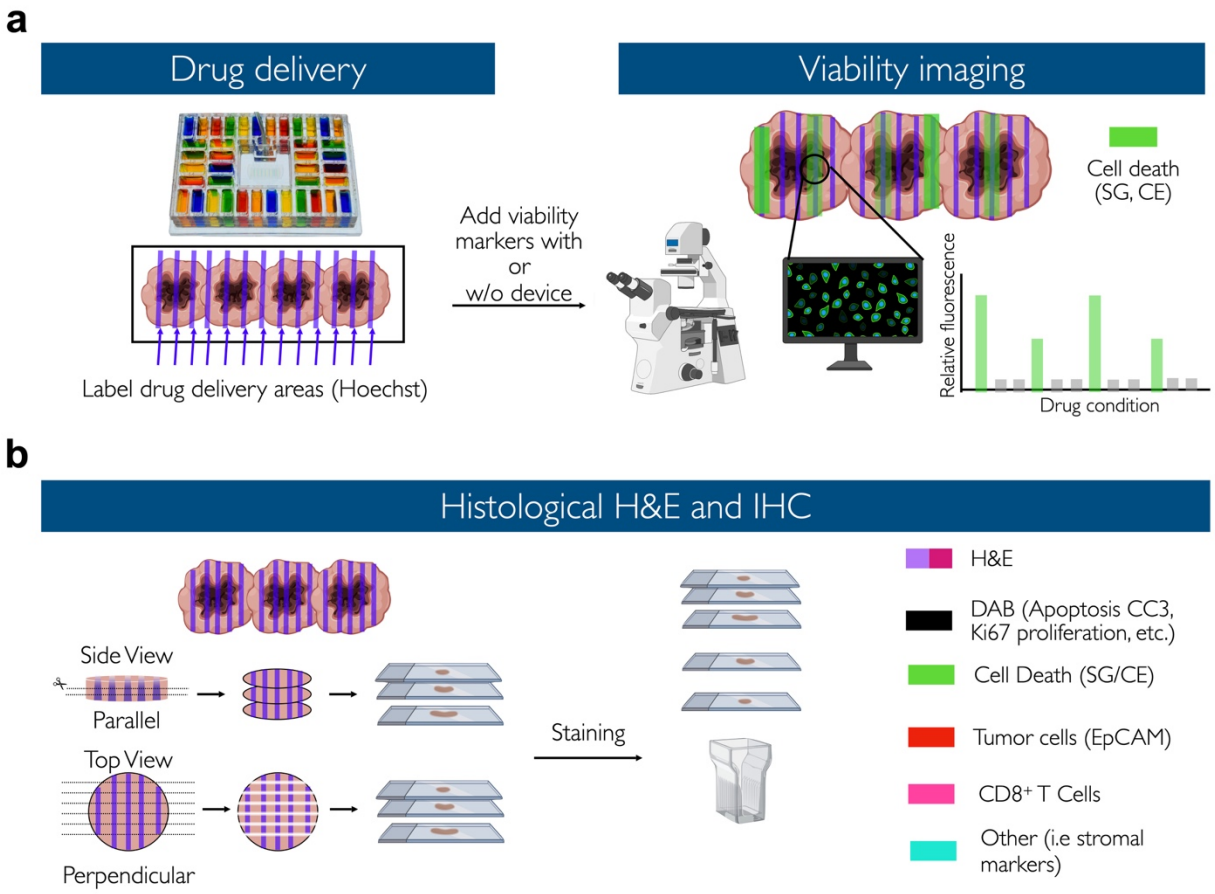

Figure 2.7 Device assay process schematic

(a) The device can be loaded with 40 different reagents. After drug delivery, delivery areas can be fluorescently labeled with a nuclear dye, such as Hoechst (blue). Similarly, cell death can be quantified using fluorescent cell viability markers such as Sytox Green and Cell Event (green). **(b)** Further tissue analyses can be made through histological H&E and IHC.

We evaluated drug responses to four different drugs with U87 xenograft tumors in prior experiments with the microfluidic device. We observed similar and reproducible response profiles independently of whether drug exposure was performed on the device or off the device in parallel control experiments.[123] In those experiments, the assay was performed at the end of drug exposure, off of the device with a single fluorescent cell death indicator.[123]

Here we explore the feasibility of on-device live tissue imaging and multiple, simultaneous cell response readouts. Using an expanded repertoire of drugs, we treated U87 flank xenograft slice cultures on the microfluidic device between day one and day three in culture (**Fig. 2.8**). As shown in Fig. 2.7a, for each device, we assayed each of the six drugs, a DMSO vehicle control, and negative buffer control (8 total delivery conditions) twice in different regions of the slices (**Fig. 2.8b**). This pattern resulted in 16 total treatments per device, each separated by buffer lanes. After 48 hrs of exposure, we exchanged the solution in the drug delivery channels to a solution containing the blue pan-nuclear dye Hoechst combined with either the green dead nuclear dye, SG, or both CellEvent and RedDot 2 (green apoptosis indicator and far-red dead nuclear dye).

After one hour, we performed live imaging with viability dyes on the device to analyze cell death drug responses. As demonstrated in the previous dye experiments (**Fig. 2.6**), the short incubation time with the fluorescent viability dyes labels only the region closest to the membrane. Therefore, we measure viability where the drug concentration is closest to that of the applied drug solution (applied over two days), and we minimize any out of focus fluorescence signal. For the first set of experiments using Hoechst and SG (**Fig. 2.8a, c, d**), we used two different devices to compare repeatability and drug response. We obtained a similar response in cell death across all drugs with both devices (**Fig. 2.8d**). For the second set of experiments using Hoechst, CellEvent, and RedDot2, we observed a similar response pattern using the same drug panel but different cell death indicators, CellEvent and RedDot2, that measure apoptosis and general cell death, respectively (**Fig. 2.8e**). To further confirm our results, we removed the slices from the device and took both high-power images (20x) and confocal images (20×) at all delivery areas (**Fig. 2.8f, k**). To quantify apoptosis and general cell death at multiple locations of each delivery area, we utilized an automated cellular analysis routine (**Fig. 2.8l**). As expected, we observed similar drug response

patterns with this high-resolution nuclear count as with the more straightforward real-time, low-resolution fluorescent intensity analysis. These drug response results also correlated with off-device drug responses seen previously.[123]

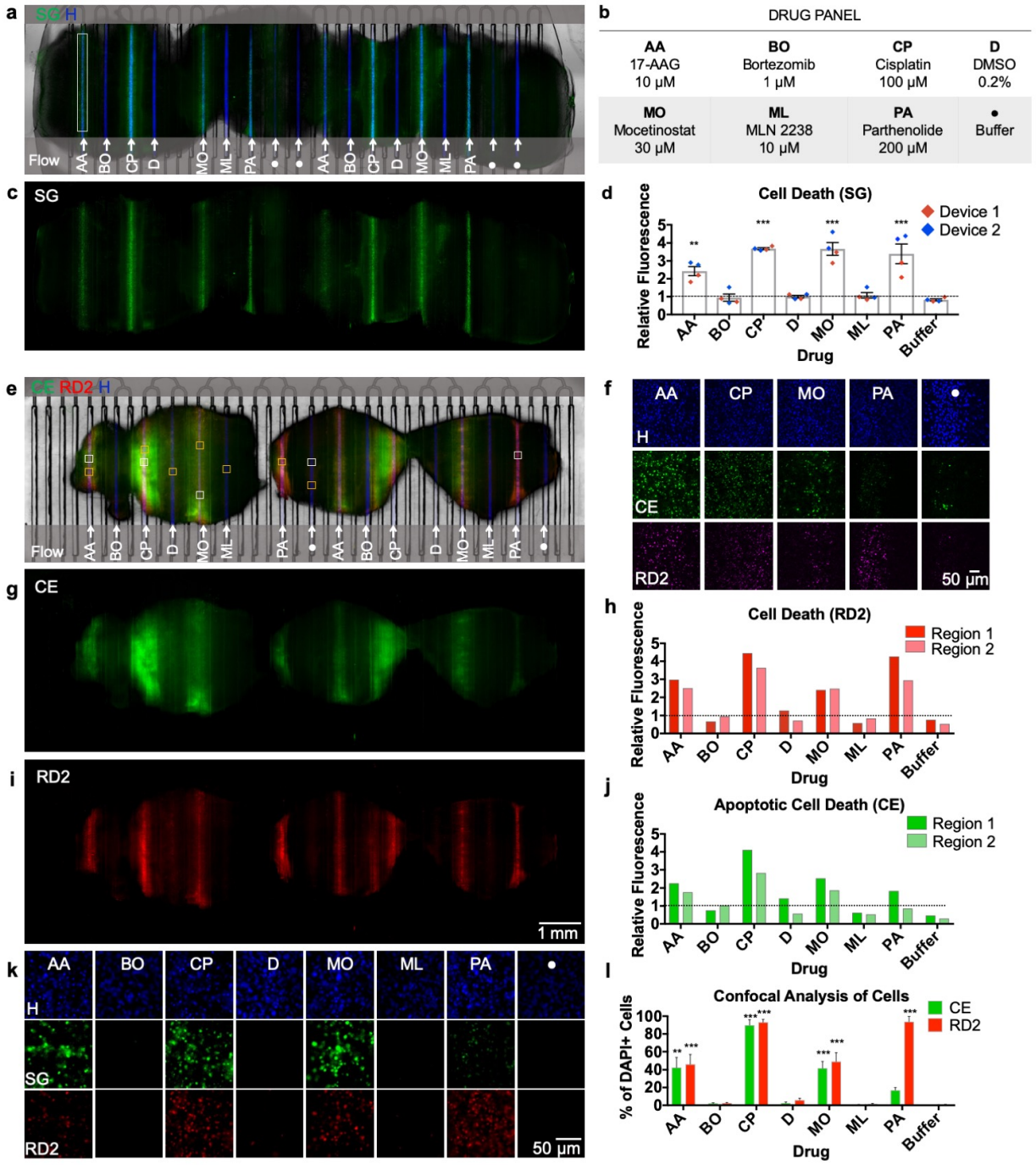

Figure 2.8. Multiplexed drug exposure of U87 GBM xenograft flank tumor slices

(a) On-device micrograph of U87 flank xenograft slices (3) after 48-hour drug exposure showing selective delivery and response to 8 different conditions **(b)**. Hoechst nuclear dye (blue) denotes areas of delivery and Sytox Green areas of cellular death **(c)**. **(d)** Drug response measured by relative fluorescence (to DMSO) obtained from two different devices running in parallel. **(e)** On-device micrograph of U87 flank xenograft slices (3) after 48-hour drug exposure, labeled with Cell Event (green, g) and RedDot 2 (red, i). f) Confocal micrographs (20×) of drugs showing response compared to negative control (samples taken from white boxes in **(e)**). **(h)** Apoptotic response is shown by Cell Event from two different tissue regions (dotted line = DMSO vehicle control baseline). **(j)** Necrotic and late apoptotic areas shown by RedDot 2 from two different tissue regions (dotted line = DMSO vehicle control baseline). k) 20× fluorescent micrographs for each condition (yellow boxes in **(e)**). **(l)** Cell Profiler cellular analysis showing % of DAPI+ cells positive for Cell Event/RedDot 2. n = 11 (AA), 5(BO & CP), 8(D & ML), 7(MO & Buffer), 6 (PA). Ave ± SEM. One-way ANOVA versus DMSO with Dunnett's multiple comparison test. *$p<0.05$, **$p<0.01$, ***$p<0.001$. Abbreviations: CE (Cell Event), SG (Sytox Green), RD2 (RedDot 2), H (Hoechst).

This set of studies demonstrated the versatility and potential of our microfluidic device. A complete assay, from drug delivery to live imaging (excluding confocal), could be performed on the platform. As shown, real-time imaging is feasible. As the cell death indicators are non-toxic to cells (except for Hoechst), in the future, one could perform continuous or intermittent measurements during drug treatments to create a more sensitive assay. The short timeframe for drug exposure and analysis (less than five days) demonstrated how the platform could potentially serve as a clinical decision-making tool after surgery by providing practical drug response information to guide patient therapeutic strategies. These studies also reflect the potential of the platform for early drug development stages.

2.3.7 *Dose-response comparison on and off the device*

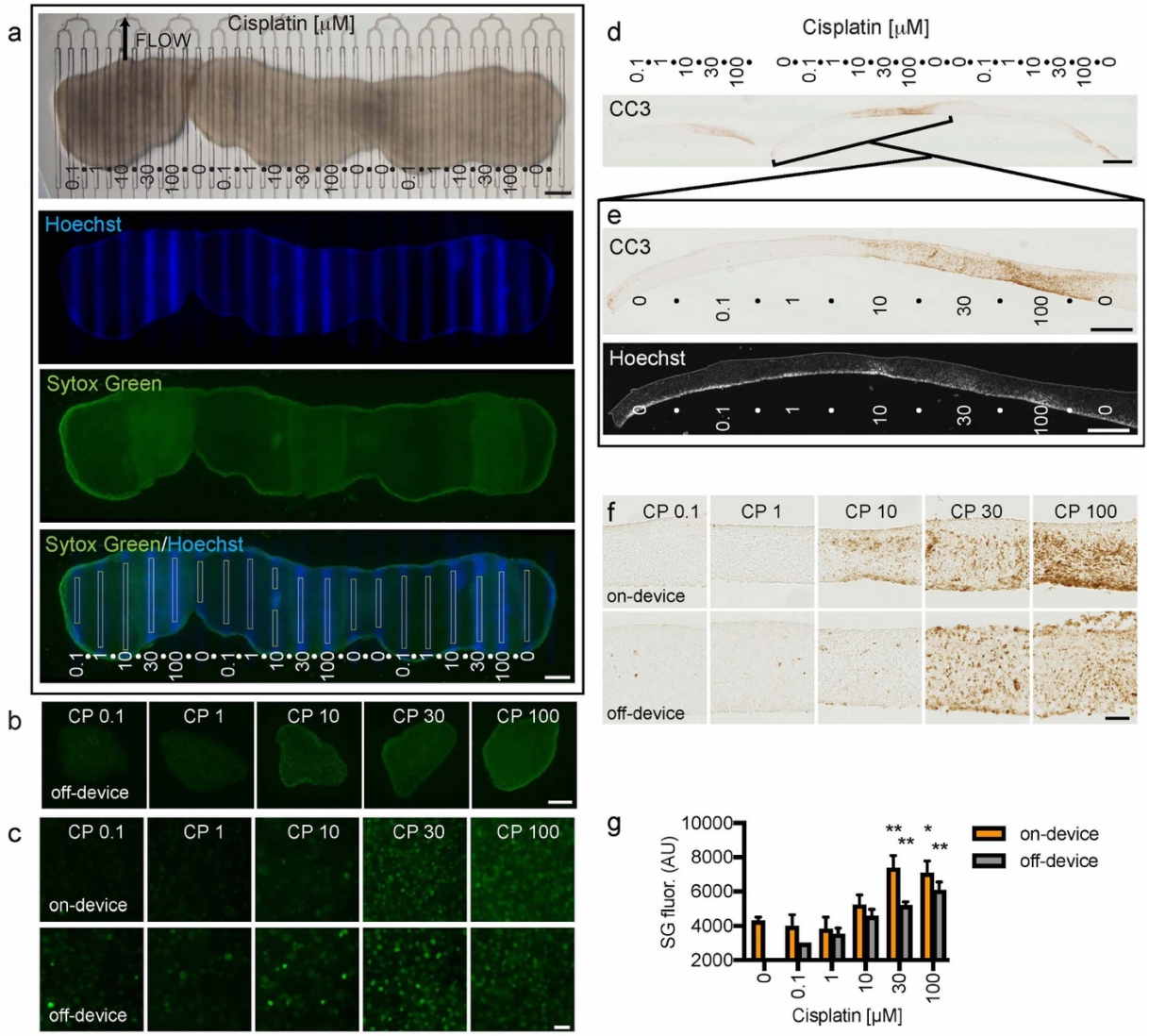

Figure 2.9 U87 slice dose-dependent drug response on and off the device

(a) Three U87 flank glioma slices on a microfluidic device were treated with different doses of cisplatin (doses in μM) from days 1-3, followed by Hoechst dye in the drug lanes, then SYTOX Green (SG) staining of the entire undersurface. Drug lanes were separated by buffer lanes (•). SG mean fluorescence intensity (boxed lane regions, 100 μm wide) was used to quantify cell death (bottom panel). **(b)** Low power images of SG staining from xenograft slices treated with drugs off-device in parallel. **(c)** High power images of SG staining of slices treated on-device or off-device. **(d,e)** Apoptotic cell death in cross-sections was detected by cleaved caspase 3 (CC3) staining. Lane locations were identified by alignment with Hoechst fluorescence. **(f)** Higher resolution images of CC3 staining

on-device or off-device. **(g)** Cell death in response to CP on or off-device, measured by SG mean fluorescence. Average ± SEM with n=3 (lanes/slices) except for n=4 for 0 and n=2 for 0.1 μM CP tested off-device. One-way ANOVA versus 0.1 μM with Dunnett's multiple comparison test separately for on- and off-device. *p<0.05. **p<0.01. Scale bars: 1 mm (a,b,d), 100 μm (c,f), 500 μm (e).[123]

We also investigated CP dose-response curves on the microfluidic device using U87 xenograft tumor slices (Fig 1.8). As shown in Fig. 2.9a, we exposed three slices placed adjacently to multiple CP concentrations on-device with alternating buffer lanes. After 48 hours of exposure, we ran Hoechst to mark drug delivery locations in the drug delivery channels. Afterward, we removed the membrane and slices from the device and exposed the whole tissue to SG to evaluate cell death (**Fig. 2.9a, c**). We treated off-device control slices with CP and SG in parallel (**Fig. 2.9b, c**). We observed significant SG cell death responses to the two highest CP concentrations on and off the device. Quantification of mean SG fluorescence (directly over the drug delivery channels on-device identified by Hoechst, as depicted in **Fig. 2.9a**) confirmed similar drug response patterns on and off the device. However, the responses on-device were higher at the two highest doses (**Fig. 2.9g**).

We also observed similar responses to the highest doses of CP, on-and-off- device, detected by CC3 immunostaining of cross-sections (**Fig. 2.9d-f**). We imaged Hoechst in the same or adjacent cross-section to identify drug delivery locations while dry before hydration. Control experiments on-device with widely spaced delivery of high CP concentrations showed cell death responses to CP (SG and CC3+). The highest dose cell death responses extended from above the treated lanes, past the first adjacent buffer lanes, but not above the second lane over (**Suppl. Fig. 2.4**). These data demonstrated the ability to assess dose responses of tumor slice cultures in our microfluidic platform and that on-device responses were similar to, or marginally more robust than, those obtained off-device.

2.3.8 *Patient GBM tumor slices on the microfluidic device*

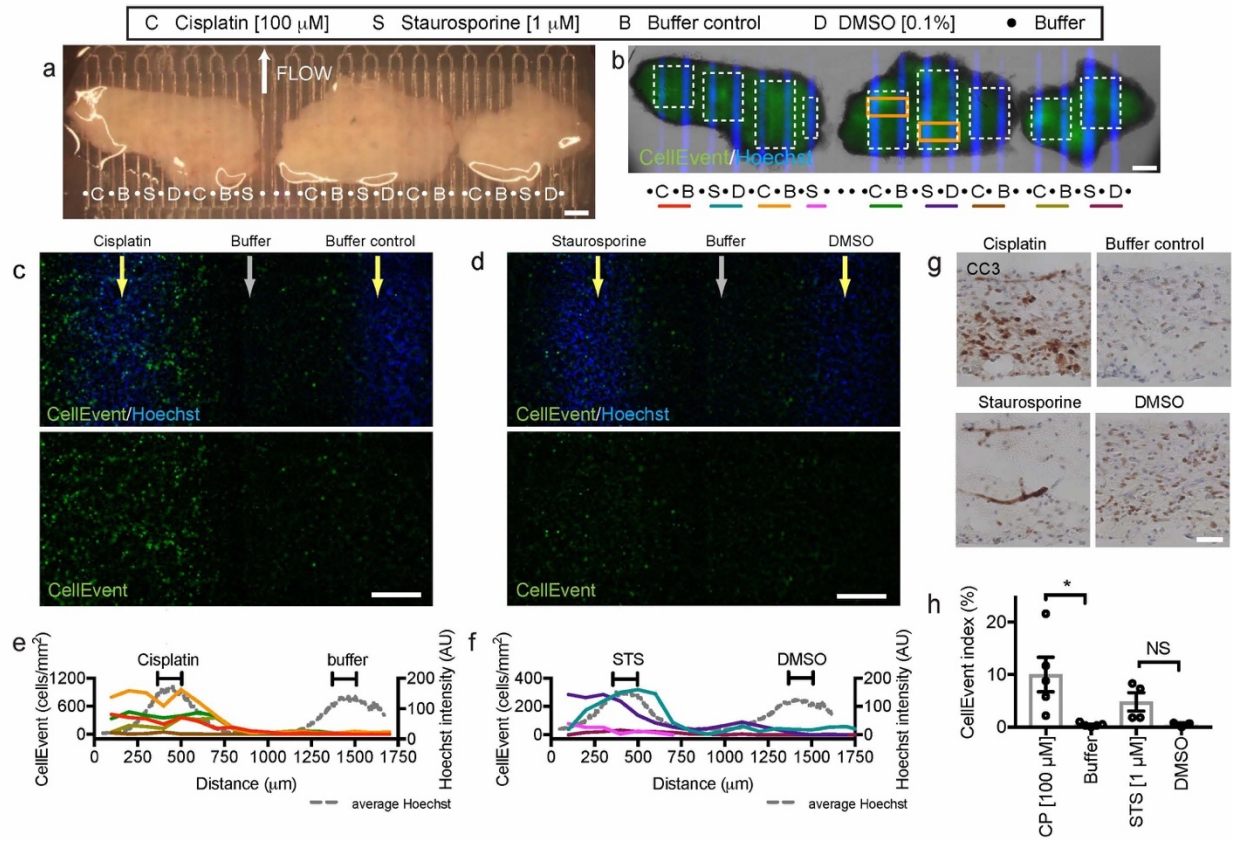

Figure 2.10 Patient glioblastoma multiforme drug responses on the device

(a) Human glioblastoma resection slices treated for 24h on-device with cisplatin (C), staurosporine (S, STS), DMSO (D, control for STS), or buffer (B) starting at d1. **b**) CellEvent staining for apoptosis, shown at higher power for orange boxes (**c,d**). **e,f**) CellEvent^{+} density (cells/mm^2, bins) across lane pairs (same-color underlines and white boxes in (**b**)). Hoechst signal (gray lines) indicates drug delivery lanes. **g)** Cleaved-caspase 3 (CC3) staining detects apoptosis in sections. **h**) CellEvent^{+} cell fractions over drug lanes (100 μm wide). Average ± SEM, individual points overlaid, n=5,5,4,3. Student's t-test for CP v Buffer and STS v DMSO, *p<=0.05. Scale bars: 1 mm (**a,b**), 200 μm (**c,d**), 500 μm (**e**), 50 μm (**g**)[123]

Looking forward to clinical application, we utilized the microfluidic device to assess drug responses in human cancer using slices obtained from glioblastoma (**Fig. 2.10a-h**). We cultured three slices from the patient's tumor overnight. The next day, we transferred the slices to the device and exposed them to CP for 24 hours (often used as a chemotherapy regimen alone or in

combination with temozolomide), buffer (control for CP), staurosporine (STS, a non-selective protein kinase inhibitor), or DMSO (vehicle control for STS), as shown in **Fig. 2.10a**). To account for the heterogeneity of the composition and baseline viability within patient tumors, we chose to use two different methods of apoptosis: CC3 immunostaining of sections and CellEvent for intact tissue applied underneath) the whole tissue immediately after drug exposure (as shown previously). We chose CellEvent instead of SG because the higher signal-to-noise for CellEvent helped with the high autofluorescence of the human GBM tissue.

As seen in Fig. 2.10b, Hoechst marks the drug delivery locations, but the native autofluorescence of human brain tumors makes the CellEvent staining challenging to visualize in low power. High power images revealed Hoechst^{+} nuclei over drug delivery channels and more isolated CellEvent^{+} dead nuclei over and next to the CP and STS locations compared to control drug channels (**Fig. 2.10c,d**). We did background subtraction to facilitate visualization and analysis of treated GBM slices. By measuring fluorescence directly over the drug delivery locations, we found a CellEvent index (% CellEvent+/total Hoechst+ nuclei) of ~10% apoptosis for the CP lanes and ~8% for the two STS-responsive lanes (**Fig. 2.10h**). The observed heterogeneity in response was consistent with the patterns of apoptosis and tissue histology seen for CP and some STS lanes by CC3+ staining (**Fig. 2.10g**). We also found baseline apoptotic signal in the control and DMSO regions, which was consistent with similar and variable CC3 staining seen in day 0 tissue that had been fixed immediately (**Fig. 2.10g**). In this test of the device with a clinical GBM, we successfully tested 17 conditions using only three slices, a critical advantage when faced with scarce availability of intact tissue samples.

2.3.9 *Semi-automated quantification of multi-parameter drug-responses in patient-derived colorectal cancer slice*

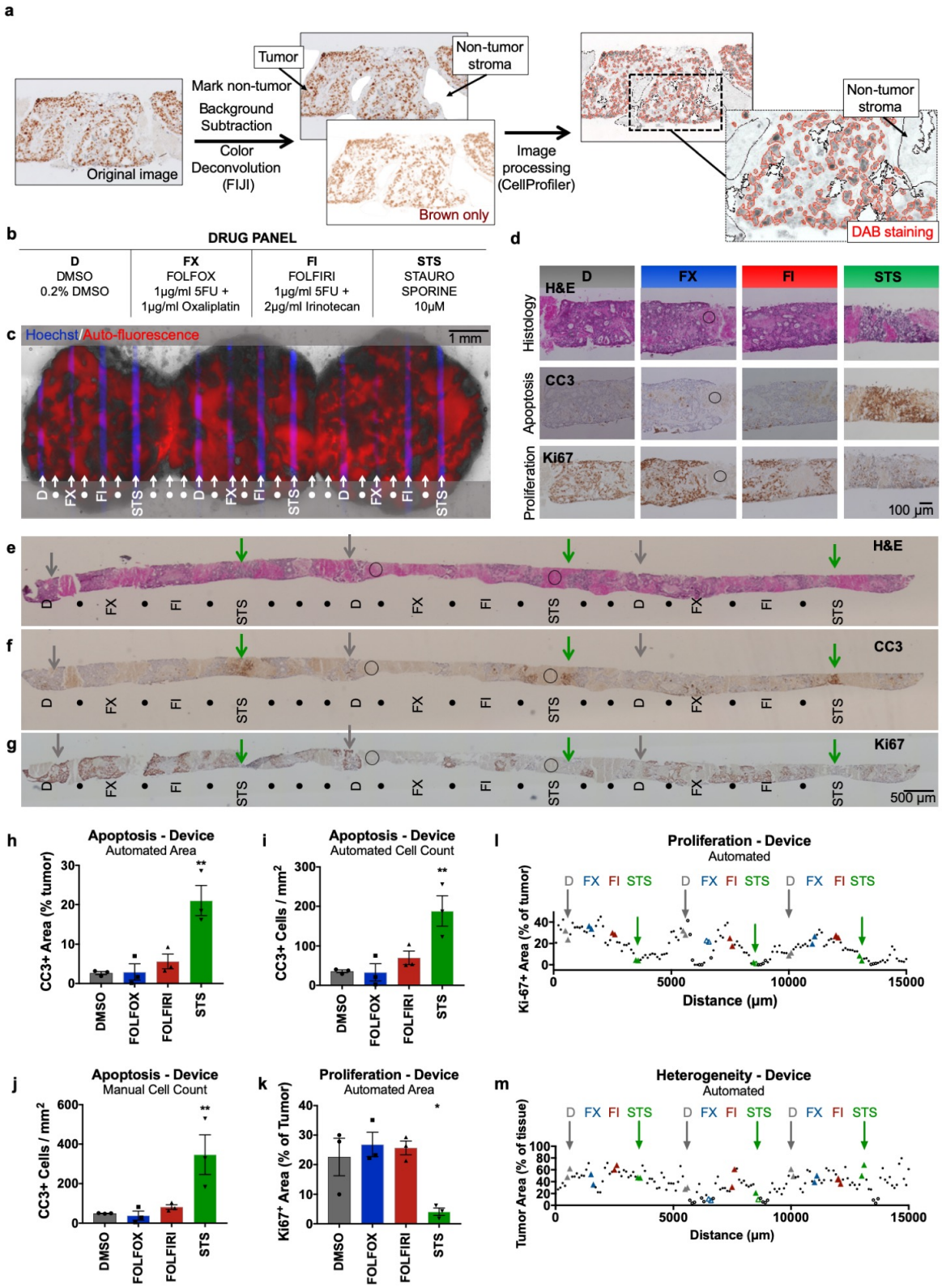

Figure 2.11 Semi-automated analysis of patient-derived liver metastasis slices from colorectal cancer (CRC) following drug exposure

Apoptosis and proliferation were quantified using immunostained metastasis slices derived from a prior experiment.[41] **(a)** Workflow for image analysis of brown DAB immunohistochemical staining of tissue sections by the FIJI program followed by a custom CellProfiler routine. **(b)** Drug panel including vehicle control (DMSO), de Gramont protocol (FOLFOX & FOLFIRI), and staurosporine (STS). **(c)** CRC tumor slices after drug exposure for two days (off-device controls for three days), showing selective delivery and response to 4 different conditions (n=3 for each, labeled with Hoechst) with alternating buffer (●). Prior analysis of CellEvent live fluorescent staining of these slices demonstrated apoptosis following STS treatment[41]. **(d-g)** Staining of perpendicular tissue sections from the bottom halves of the CRC slices **(c)** shows H&E appearance and identifies apoptosis (CC3) or cell proliferation (Ki-67) for each treatment. **(d)** Representative 20× micrographs of drug delivery areas. **(e-g)** Low power micrographs of perpendicular sections show indicated locations of drug delivery channels as inferred from the Hoechst staining of adjacent sections. DMSO control (D, grey arrows), STS (green arrows), and non-analyzable stromal areas (circles) are indicated for orientation. These images of CC3 and H&E staining in perpendicular sections resemble the images of staining previously seen in parallel sections taken from the top halves of the same CRC slices in Horowitz et al. Fig. 7.[41] **(h-j)** Apoptosis after drug treatment based on automated area analysis (**(h)**, % of tumor), automated cell count (i, CC3+ cells/mm^2 total area), or manual cell count (**(j)**, CC3+ cells/ mm^2 total area) of images that largely exclude stromal (non-tumor) regions. **(k,l)** Proliferation after drug treatment, based on automated area analysis (% of tumor). Images were subdivided into 100-μm-wide regions for analysis along with the entire tissue **(l)**, and drug treatment locations were analyzed over a 200-μm-wide area for **(k)**. **(m)** Heterogeneity of tumor area as % of total tissue averaged from all images analyzed for each 100-μm-wide region. n=3 locations per condition, with six sections (>100-μm apart), analyzed per location. Ave ± SEM. One-way ANOVA versus DMSO with Dunnett's multiple comparison test. *p<0.05, **p<0.01, ***p<0.001. Abbreviations: DAB (diaminobenzidine), HPF (high-power field).

To overcome a significant roadblock to our microfluidic platform application to test clinical samples, we developed a semi-automated, quantitative method to analyze multi-parameter drug-response and cell-specific readouts immunohistochemical staining in cross-sections taken of the

slices after fixation. Autofluorescence makes non-fluorescent DAB (diaminobenzidine) immunostaining the choice approach with many human tissues, but its quantitation is challenging and usually done manually.

Here, we show a semi-automated approach for quantitative image analysis of DAB staining for apoptosis and the proliferation of a clinical tumor sample (**Fig. 2.11a**). It is easy to perform and uses free software (FIJI and CellProfiler). We used data from a previous experiment in which we used the device to test the effects of different drug regimens on tumor slices from a patient with colorectal liver metastasis, then analyzed apoptosis by fluorescence and by DAB CC3+ staining, but without quantitation of the CC3+ staining.[123] In that experiment, before drug exposure, patient-derived tumor slices (~250 μm) were cultured off-device for three days, then tested for viability with an MTT assay. We selected viable slices for a comparative drug exposure experiment. We placed three slices on the device and treated each slice with four conditions for 48 hrs. Slices were treated with FOLFOX and FOLFIRI, two standard chemotherapy combinations for metastatic CRC (see Methods). These two regimens describe the de Gramont protocol, based on the infusion of fluorouracil (always combined with LV) plus either Oxaliplatin (FOLFOX) or Irinotecan (FOLFIRI), which has been standard first-line chemotherapy for metastatic CRC.[134,135] Before the tumor resection, the patient had received treatment with FOLFOX. Slices were also treated with staurosporine (STS, 10 μM) as a positive control and DMSO (0.2%) as vehicle control. Each slice was exposed to all four conditions at least once, with buffer channels in between. At the end of drug treatment, we delivered Hoechst through the drug delivery channels for 2 hrs to mark the areas of the tissue treated with drugs (**Fig. 2.11b, c**). Then we removed the slices from the device and treated the whole tissue with CellEvent to measure apoptosis and the red, dead nuclear dye, ethidium homodimer 1, to measure overall cell death (data not shown). We performed off-device

drug treatments in parallel, but with more prolonged drug treatment for three days instead of two days. The tissue's complex heterogeneity made it challenging to perform an initial chemosensitivity assessment from the tumor undersurface as we had done previously with the xenograft tumors. Most of the tumor slices had intense autofluorescent fibrotic stromal regions (**Fig. 2.11c**, red), likely resulting from the patient's prior neoadjuvant chemotherapy and radiation. Previously, we performed an initial fluorescent analysis of this experiment in which we detected a significant increase of CellEvent apoptosis signal after STS and a non-significant increase after FOLFIRI.[123] This analysis required image processing to remove autofluorescent areas.

To enable a more robust and flexible analysis for drug responses insensitive to background fluorescence, we developed quantitative assays for both apoptosis and loss of proliferation that utilize non-fluorescent immunostaining of tissue sections, the standard approach used in clinical pathology. After we sectioned the treated CRC slices, we performed CC3 immunostaining for apoptosis, Ki-67 immunostaining for proliferation, and H&E staining for histology (**Figs. 2.11d-g)**. We identified drug exposure areas in each slice section using the Hoechst signal in adjacent sections as a guide. Then we measured drug effects by a custom image analysis routine to identify the positively stained area or cells using FIJI and CellProfiler (**Fig. 2.11a, h-m**). We compared automated and manual CC3+ analyses of the same images for positive staining area and cell counts (**Fig. 2.11h-j**). We took images within the 200 μm centered over the drug delivery locations, avoiding non-tumor regions. We favor the area quantitation because the automated cell counting approach sometimes undercounts adjoining cells. As seen in Figs. 2.11h-j, CC3 immunostaining revealed a clear apoptotic cell death response at the regions of STS treatment and no response to the other two-drug combinations on-device, as well as off-device (**Suppl. Fig. 2.5b**). Similarly, an

MTA viability analysis of slices treated off-device showed reduced viability only with STS (**Suppl. Fig. 2.6a**).

To further automate DAB staining analysis, we performed analyses of proliferation and heterogeneity across the complete tissue sections (**as in Fig. 2.11k-m; Suppl. Fig. 2.5d, e**) taken as tiled 20× images. We performed Ki67+ area quantitation on consecutive 100 μm-wide images to reveal the proliferation patterns along all of the tissue, including all drug treatment conditions (**Fig. 2.11l**). We also evaluated only the 200 μm-wide region above the drug treatment location (**Fig. 2.11k**). Ki67 immunostaining revealed reduced proliferation (as expected in areas of drug effect, the opposite of CC3) that was strong at STS treatment regions (**Fig. 2.11k, l**). Interestingly, off-device, we observed a significant proliferation reduction for STS, FOLFIRI, and FOLFOX compared to vehicle controls (**Suppl. Figs. 2.5, 2.6**). This difference likely reflects the longer treatment time off-device than on-device and suggests that more prolonged treatment may be more sensitive to detecting drug responses. Although a longer treatment time did not increase apoptosis, it may have affected proliferation. The lack of a strong response to the chemotherapies may result from the patient's previous treatments with one drug regimen.

This analysis also helped quantitate and visualize the extent of tumor/stroma heterogeneity for sampling these CRC tumor slices. We found that our sections contained 40% ± 17% tumor (ave ±SD, range 4-80%, n=151 regions), averaged across the extent of the tissue (**Fig. 2.11m**). While the amount of tissue analyzed across the tissue remained approximately the same (**Suppl. Fig. 2.5d**), the total amount of tumor analyzed per region varied, demonstrating the need for increased sampling in some regions for this tumor (**Suppl. Fig. 2.5e**). These results demonstrate how this type of analysis can facilitate functional drug response readouts and address the impact of heterogeneity in clinical samples.

2.3.10 *Preliminary combination immunotherapy studies using patient pancreatic cancer slices*

In addition to multiplexed drug delivery, our microfluidic platform has also allowed us to investigate regioselective and gradient applications of immunomodulators/drugs to study the tumor immune microenvironment (TIME) while taking into account intratumoral heterogeneity. Pancreatic cancer is a challenging disease to treat, in part due to the complexity of its TME. Stromal myofibroblasts and regulatory immune cell populations inhibit effector T cell function through both direct cell-cell interactions and the creation of chemokine gradients that alter cell migration. Our preliminary studies combined our microfluidic device with established human pancreatic cancer organotypic slice cultures[136] to study the regionally localized effects of anti-PD-1 and AMD3100 (CXCR4 inhibitor) (**Fig.2.12**). We intend to expand on recent findings with these experiments showing that combination checkpoint immune inhibition activates resident T cells in human pancreatic slices.[137] CXCR4 inhibition with the small molecule AMD3100 led to the distribution of $CD8^+$ T cells from the stroma into the tumor compartment; furthermore, CXCR4 inhibition (**Fig. 2.12b**) synergized with anti-PD-1 antibody (**Fig. 2.12a**) blockade as measured by $CD8^+$ T cell proliferation and tumor cell death. [137]

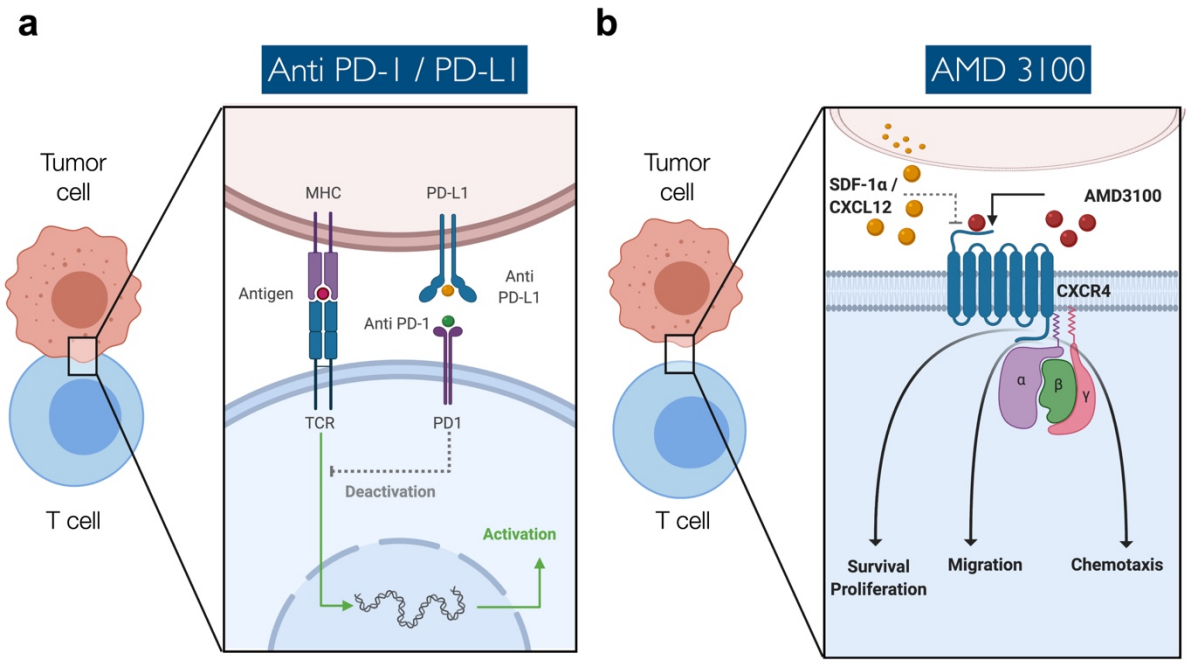

Figure 2.12 Schematic of anti-PD1/PD-L1 and CXCR4-CXCL12 axis blockade

(a) Blocking PDL-1 or PD-1 allows T cell killing of tumor cells **(b)** Blockade of the CXCR4-CXCL12 axis has shown to inhibit immunosuppressive elements such as survival/proliferation, migration, and chemotaxis.

Our first set of experiments focused on migration and activation in response to combinatorial treatment. We treated three patient pancreatic cancer slices for two days with the AMD3100 (**Fig. 2.12a, right**) or without (**Fig. 2.12a, left**) over the entire slice and localized delivery anti-PD-1 antibody. As with our previous experiments, we visualized areas of anti-PD-1 delivery with Hoechst dye (blue stripes). Frozen sections showed apoptotic cell death revealed by anti-cleaved caspase 3 ($CC3^+$) immunostaining of the section (**Fig. 2.13c, d).** Notably, apoptotic areas were mostly observed on tumor regions when compared to stromal regions. Future work will focus on a quantitative analysis of adjacent frozen sections to determine areas of apoptotic cell death and migration/activation of $CD8^+$ T cells to tumor areas.

`

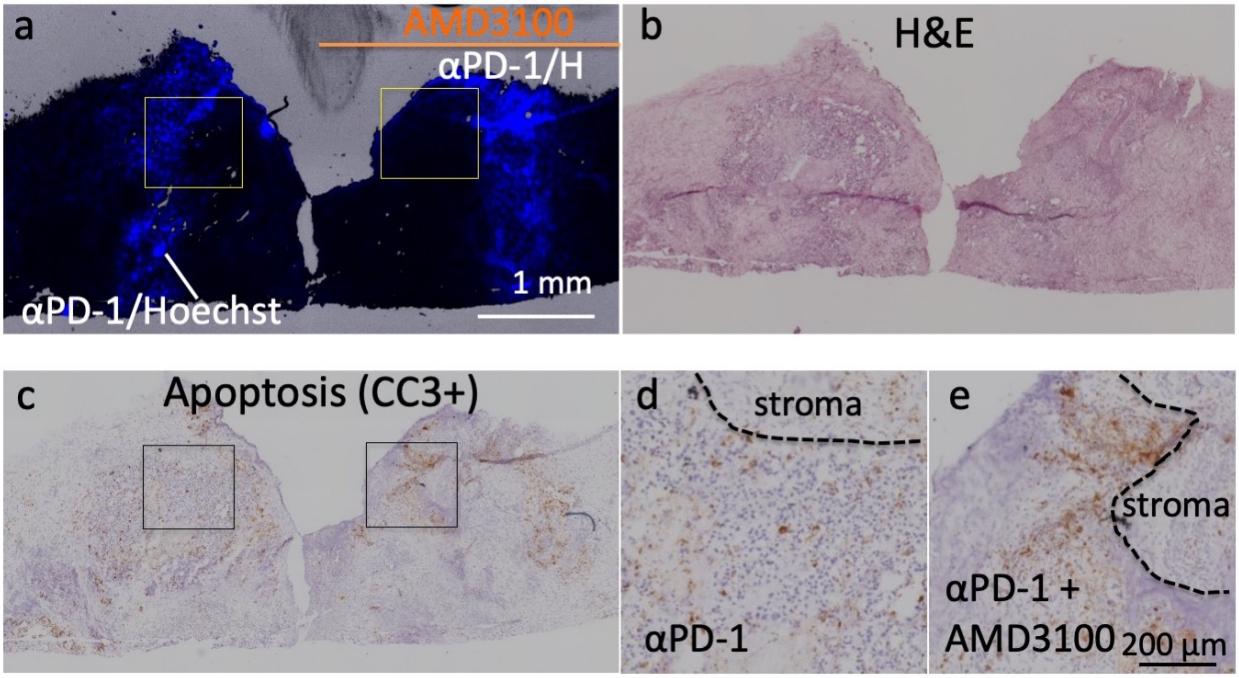

Figure 2.13 Combination immunotherapy on-device using human pancreatic adenocarcinoma slices.

(a) Slices were treated for two days with the AMD3100 (CXCR4 inhibitor) (right) or without (left) over the entire slice and with stripes of anti-PD-1 antibody (visualized at the end with Hoechst dye). **(b)** Apoptotic cell death was revealed by anti-cleaved caspase 3 (CC3+) immunostaining of the same section. **(c, d)** close-ups of boxed areas.

In addition to combinatorial immunotherapy, we intend to perform immunomodulator gradient studies on the device using CXCL12. Previous studies have found that blocking the binding of CXCL12 to its receptor CXCR4 on T cells permits their migration in human pancreatic cancer slices. Moreover, CXCL12 appears to play a crucial role in the TME-driven immune suppression of pancreatic cancer through its effects on CXCR4-expressing immune cells, particularly effector T cells. [138] Research into chemokine effects on immune cells has suggested a concentration at which chemoattractant, such as CXCL12, cab become chemorepellent.[139] Most of these studies have been performed in cell lines, organoids, or mouse studies, so the creation of gradients for T cell migration within the intact human TME represents a critical application for the

microfluidic device. Immunomodulator gradients should influence the distribution and activation of highly motile T cells. Therefore, to precisely define the impact of CXCL12 on chemotaxis in the TME, we will create artificial gradients of CXCL12 within the slice culture platform.

2.4 CONCLUSIONS

This chapter reports the redesign of a microfluidic platform for functional drug testing of live tumor slices. Fabrication of the new platform is based on CO_2 laser microfabrication and digital manufacturing of thermoplastics, which are fast and inexpensive. Cost-efficient manufacturing is crucial at the pre-clinical testing stages, where the platform needs to be disseminated to as many laboratories as possible. We demonstrated the microfluidic platform's functionality with characterization studies and multiplexed drug delivery to human GBM cell-derived xenograft slice cultures and CRC patient-derived tumor slices. We also present practical protocols for drug response readouts for cell death and proliferation, including on-device fluorescent live/dead analysis. Potential future improvements of the device could include dynamic control of flow by incorporating microvalve multiplexers[140] (e.g., for time-changing combinatorial mixing),[141] micropumps,[142,143] flow control actuators,[144] and real-time mixing elements.[145] These functional drug assays highlight the potential for future uses of our platform using clinical tumor samples for personalized medicine and utilizing intact human tissue for early stages of cancer drug development.

2.5 EXPERIMENTAL

2.5.1 *CO_2 Laser Micromachining*

The current version of our platform consists of a 40-well plate with an integrated channel network layer. We fabricated the platform by laser micromachining of PMMA substrates and thermal fusion and solvent bonding techniques. The device is composed of three layers: a 19 mm-thick PMMA bottomless 40-well "well plate" (1227T569, McMaster-Carr, Elmhurst, IL), a 300 μm-thick PMMA channel network layer (Astra Products, Baldwin, NY (11510103)) containing 40 closed microchannels that feed into 40 roofless microchannels ("delivery channels"), and a 125 μm-thick PMMA sealing layer (AFT00, SPolytech, Chungbuk, Korea). The device also has a customized base and a lid (1227T569, McMaster-Carr, Elmhurst, IL). The base raises the device from the surface to avoid scratches (thus maintaining optical clarity) and makes its dimensions compatible with conventional imaging stages. The lid prevents contamination and allows proper airflow for tissue culture. During operation, the roofless delivery channels are sealed with a porous membrane (see below).

The CO_2 laser system used (VLS3.60, Scottsdale, USA) has a wavelength of 10.6 μm and a maximum power of 30 W. We optimized the power and speed settings of the CO_2 laser to achieve specific widths and depths for the microchannels and to cut the outlines of the channel network and sealing layers. To develop the well plate, we utilized another CO_2 laser system (ILS12.150D, Scottsdale, USA), which has a maximum power of 150 W and the same wavelength. Multiple passes with this laser were needed to create smooth through-cuts for the wells of the well plate. We also cut out a hole in the plate to form the main outlet of the device. Finally, we engraved a shallow well around the outlet hole for tubing installation after assembly.

2.5.2 *Post-ablation processing*

Laser ablation of PMMA includes both polymer debris and reflow. To remove debris from the laser-cut substrates, we rinsed each of the device components with DI water and sonicated them in an IPA bath for 2 min. To reduce surface roughness and improve the optical quality, we exposed the channel network to chloroform vapor. We used a glass container (264 mm (L) × 213 mm (W) × 165 (T) mm) filled with 50 mL of chloroform and steel standoffs (6 mm) to elevate the laser-micromachined layers 3 mm above the chloroform surface. We exposed the channel network layer and the sealing layer to chloroform for 4 and 2 min, respectively.

Laser cutting of the well-plate caused the PMMA substrate to warp (~1 mm warpage over 113 mm length) due to the laser's thermal stresses during ablation. Assuming the PMMA substrate was placed in a vacuum chamber, with no heat sink and uniform heat distribution, it would absorb about 135,000 J of energy after laser cutting at 150W for 15 min. Considering that the laser platform has a heat sink (air assist and an aluminum pin table) and there is abundant heat loss due to a) reflected longwave radiation, b) re-radiated longwave radiation, and c) heat transmission, the actual heat absorbed by the PMMA plate should be much lower. Nevertheless, we observed that the prolonged laser ablation processes caused melting and deformation of the PMMA well plate. We were able to fix the plate's deformation after ablation by pressing at 1,000-1,500 psi and heating at 110 ˚C at the same time for 10 min in a thermal press (Carver Inc. 4126). Afterward, the plate was cooled down to room temperature for 10 min while still being pressed. The corrected well plate was then rinsed with DI water, sonicated with IPA, and exposed to the chloroform vapor for 30 min using the previously mentioned setup.

2.5.3 *Thermal fusion and solvent bonding*

Exposure to chloroform vapor also causes the PMMA to become slightly adhesive by inducing polymer reflow.[75,146] After chloroform vapor treatment, the surface of the PMMA substrates becomes soft due to polymer solvation. When two treated surfaces are placed in contact, a cohesive molecular bond is formed while excess vapor evaporates from the interface. For assembly, we exposed the channel network layer and the sealing layer to chloroform vapor. For thermal fusion bonding, we first hand pressed the sealing layer onto the channel network layer to form a weak bond. Then, to ensure uniform bonding, we sandwiched the two layers between two ~3 mm-thick PDMS slabs with the same outer dimensions as the channel network layer. Finally, we placed the whole ensemble in the heat press for 10 min between 120-160 psi at 60˚C.

Although it is possible to build complex microfluidic networks with laser-cut laminates using glue as the bonding layer,[147] biocompatibility concerns about the glue prompted us to adopt solvent-bonding, an adhesive-free approach. We used methylene chloride to bond the channel network layer to the 40-well plate (Weld-On 4, Durham, USA). This solvent also softens the PMMA substrates' surfaces, and it bonds the substrates together as it evaporates. For this bonding process, we directly exposed the plate's bottom to methylene chloride for 15 seconds. Immediately after, we blew nitrogen into the outlet tubing hole of the 40 well-plate to remove excess solvent; if left behind, this excess solvent can dissolve the channel inlets and outlet in the channel network layer during the bonding process. Then, we aligned the channel network layer with the outlet of the well-plate and hand-pressed them together. We placed a 500 μm-thick blank PMMA sheet with the same outer dimensions as the channel network layer on top of the channel network layer, and then we put all the layers in between two PDMS slabs for even pressure distribution. We then placed the whole assembly in the heat press at 200 psi for 5 min at room temperature. To build the

platform prototype that can accept Transwells, we followed the same pressing process, and we bonded the device with 3M™ 300 LSE transfer adhesive. We first bonded a set of two laser-cut 1/8" PMMA well-plates with the modified design channel layer. Finally, we added the connection tubing to the well-plate outlet and secured it into place by filling the empty well surrounding the outlet with ethyl cyanoacrylate glue (Gorilla Glue, Cincinnati, USA).

2.5.4 *Hydrophilization and sterilization*

After device assembly and before use, we treated each device with oxygen plasma for 5 min at 660 mTorr to increase the PMMA surfaces' hydrophilicity. Then, to prepare the device for use with biological samples, we placed the device in a tissue culture hood and filled the microchannels by pipetting sterile PBS into the well reservoirs and the central culture area. We covered the roofless channels with a PDMS membrane, and suction was applied to fill the microchannels. After filling the microchannels, we left the device under UV for 1 hr for sterilization.

2.5.5 *Device operation*

Before use, we filled the device with culture medium and transferred it to a cell culture incubator to allow the temperature and pH to equilibrate. After ~1 hr of incubation, we transferred the slices from the tissue culture insert by cutting out the PTFE membrane and placing it onto the device's roofless channels. After transferring the slices to the device, we imaged the central culture area to capture the tissue slices' position relative to the delivery channels. Then, we filled each well reservoir with either drug or buffer with at least one buffer lane between each drug delivery channel. We diluted drugs (MedChem Express) from DMSO stocks (10-200 mM), except for cisplatin (3M stock in dH_2O). We operated the device by connecting the outlet of the device to a

60 mL syringe (BD Bioscience, San Jose, CA) and syringe pump (Fusion 200, Chemyx Inc., Stafford, TX) at a flow rate of 1.5 mL/hr for xenograft drug studies and 2 mL/hr for vertical diffusion and CRC studies.

2.5.6 *Scanning Electron Microscopy*

We took scanning electron microscopy (SEM) images of the laser cut PMMA channels to evaluate the channels' topological changes due to chloroform exposure and the channels' dimensions (roofless and sealed). We prepared the samples by rinsing with DI water, sonicating with IPA for 2 min, and rinsing with DI water again. We utilized nitrogen gas to remove excess water and left the samples dry overnight. To image microchannel cross-sections, we prepared substrate samples through a freeze-fracture process involving immersion in liquid nitrogen. Finally, before SEM observation, we coated all samples with a thin, 19.5 nm-thick film of Au-Pd to prevent charging.

2.5.7 *Image acquisition*

We imaged the tissue slices for epifluorescence and brightfield imaging using a Nikon Eclipse Ti inverted microscope (Nikon Instruments, Melville, NY), except for where specified in Fig. 7l where we used a Nikon A1R Confocal system (Lynn & Mike Garvey Imaging Core, University of Washington). We acquired images using an automated XY stage and 4×, 10×, and 20× objectives. To generate images, we stitched all the images with 10% overlap. For controlled imaged acquisition, we used the Nikon NIS-Elements AR software.

2.5.8 *Lateral spread assessment using fluorescein*

We covered the roofless delivery channel area (19.70 mm × 5.42 mm) with a manually cut porous Millicell® polytetrafluoroethylene (PTFE) membrane (32 mm × 20 mm, 0.4 μm, Millipore). We filled the well reservoirs of 6 channels with 100 μM fluorescein, leaving the rest filled with phosphate-buffered saline (PBS). To analyze spread three channels in both directions (when possible), we intentionally separated each of the selected delivery channels by six channels.

After loading the device, we operated it at 0.1, 0.2, 0.3, 0.4, 0.75, 1, and 10 mL/hr. To determine the fluorescence profiles of fluorescein, we took images at each flow rate after waiting for equilibration for ~10 min. We also acquired images at 7 ms and 70 ms exposures for every flow rate. Then, we analyzed lateral diffusion in the middle, upstream, and downstream for each of the six channels of interest and the adjacent channels. We did a fluorescence profile along the delivery channels and their three adjacent channels in our first analysis. In the second analysis, we measured the relative fluorescence in each of the three channels adjacent to the delivery channel after background subtraction. For each flow rate, we averaged the values based on the channel's location: 7 ms for the delivery channel and 70 ms for one, two, or three channels away. We utilized relative fluorescence between the two exposures to obtain a correction factor to adjust the 7 ms data to match the 70 ms data. Finally, we normalized the data to the average fluorescence at the six delivery channels.

2.5.9 *Diffusion of fluorescent compounds in live tissue*

After seven days in culture, we transferred the U87 flank xenograft slices to the device, then exposed them to alternating delivery channels containing Hoechst (16 μM) and Doxorubicin (DOX, 10 μM) for four different periods (1, 2, 4, and 8 hrs). There were two lanes for 1 hr and

four lanes for 2, 4, and 8 hrs. After exposure, we rinsed the delivery channels with PBS for 10 min. We then immediately froze the exposed slices and analyzed them as dry cryosections (10 μm thick) to prevent any additional diffusion. We placed vertical profiles (100 μm wide) in the center of each delivery location for vertical diffusion analysis. We averaged three adjacent sections to yield profiles for each of 8 locations per period (2 locations on each delivery lane). We plotted the average and standard deviation (SD), with n=8 (except for n=4 for 1 hr).

2.5.10 *Diffusion constant estimation*

We applied Fick's laws of diffusion to understand the penetration of the drug within the tissue quantitatively. A solution to Fick's second law of diffusion in semi-infinite media and a constant concentration surface is given by:

$$\mathrm{C(x,t)} = \frac{\mathrm{C}_x - \mathrm{C}_0}{\mathrm{C}_s - \mathrm{C}_0} = 1 - erf\left(\frac{x}{2\sqrt{Dt}}\right) = erfc\left(\frac{x}{2\sqrt{Dt}}\right)$$

Equation 2.1 Fick's second law of diffusion

where *D* represents the effective diffusivity of Hoechst and doxorubicin in tissue, $C(x = 0) = CS$ is the concentration of doxorubicin at the PTFE membrane and tissue interface, and $C(x = \infty) = C_0$ corresponds to the initial concentration of doxorubicin on the top surface of the tissue. We assume that CS remains constant over time, and $C_0 = 0$ for the early time-periods (< 8 hrs) of drug application (that is, the drug has not traversed the entire thickness of the tissue). The characteristic diffusion length (L) at a given time (t) is defined as the distance at which the concentration of the diffusing species reaches ~50% of the source concentration (CS) and can be approximated by $L \approx \sqrt{Dt}$. We determined the diffusivity (D) of Hoechst and doxorubicin in the tissue from the experimentally observed diffusion length (L) at each time point (t).

2.5.11 *GBM xenograft slice culture*

We cultured U-87 MG cells (U87, ATCC) in DMEM/F12 (Invitrogen) supplemented with 10% fetal bovine serum and penicillin/streptomycin. We passaged the cells every 3-5 days at ~75% confluency. We handled mice experiments in accordance with a protocol approved by the University of Washington Animal Care and Use Committee. We injected male immunodeficient nude mice (Taconic, Foxn1^{nu}) aged 4-10 weeks subcutaneously in the flank (~1 million cells in 200 μL of serum and antibiotic-free medium). Before the flank tumor volume reached 2 cm (2-4 weeks), we sacrificed the mice. Once sacrificed, we removed the tumor, cut 250 μm-thick slices with a 5100mz vibratome (Lafayette Instrument), and cultured on top of PTFE, 0.4 μm pore membrane Millicell® cell culture inserts (Millipore) in 6-well plates. The slice culture medium underneath contained Neurobasal-A medium (Invitrogen) with 25% heat-inactivated horse serum (Sigma), Glutamax (Invitrogen), 2× penicillin/streptomycin (Invitrogen), and growth factors (EGF 20 ng/mL and FGF 20 ng/mL, Preprotech or Invitrogen). We changed culture medium three times per week.

2.5.12 *Patient-derived tumor slices*

We obtained metastatic rectal cancer tumor tissue with informed consent and treated it in accordance with Institutional Review Board approved protocols at the University of Washington, Seattle. We prepared CRC tumor slices from a 68-year-old male with metastatic rectal cancer post-neoadjuvant chemotherapy, resection, and radiation. Slices were treated with two different standard chemotherapy combinations for metastatic CRC: 1) Fluorouracil (5FU) and Oxaliplatin, 1 μg/mL each (termed "FOLFOX"), and 2) 5FU and Irinotecan, 1 μg/mL each (termed "FOLFIRI"). Before tumor resection, the patient had FOLFOX treatments for about seven months

(cycles sometimes excluded Oxaliplatin due to side effects). After chemotherapy, the tumor size was ~3.7 cm. We sectioned the CRC tumor from 6 mm core punches taken from the resected tumor. With the 6 mm cores, we cut 250 μm-thick slices with a vibratome (Leica) and placed them in culture with shaking. We have found that CRC slices maintain their histology, viability, and proliferation for up to 1 week in culture.[148] After three days of culture, we quantified the change in viability after drug exposure using CellTiter 96® Non-Radioactive Cell Proliferation Assay (MTT, Promega). We performed the MTT assays in a 48 well plate containing 400 μL culture media and 80 μL of MTS reagent in each well. After transferring the slices to each well with a sterile pipette tip, we placed the slices in a rocker inside the incubator for 3 hrs. After 3 hrs of incubation, we placed 200 μL from each well into a 96 well plate and read absorbance at 490 nm. For off-device analyses, we determined response through a viability comparison before and after treatment using fluorescence microscopy.

2.5.13 *Multidrug exposure data analysis*

We used the free Fiji[149] image analysis program for SG and CellEvent/RedDot2 image analysis on tiled 2× images taken with tumor slices on the microfluidic platform. For the device experiments, we selected a rectangular region (~130 μm wide) for each condition using the Hoechst channel to avoid ~25 μm of the slices' edge (see Fig. 6a). For background subtraction on both conditions, we used four circular regions outside the slices. We calculated the background by averaging all values for each fluorescent channel. After background subtraction, we calculated the total average fluorescence for each region relative to DMSO (here termed "vehicle control" because we solubilized drugs in DMSO; all solutions contained 0.1% DMSO independently of the drug concentration except for cisplatin). We analyzed the images acquired by confocal microscopy (20×) with CellProfiler (Broad Institute). We created a custom routine to identify all nuclei from

each channel (Hoechst, CellEvent, RedDot2) using a single manual threshold applied to all images for each channel.

For CRC experiments, we took 20× images of DAB staining for CC3 at all drug exposure areas from seven sections of the slice cut perpendicular to the membrane. To remove cell counting bias, the observer manually counted CC3+ or Ki67+ cells only in tumor+ areas was blinded to the experimental conditions (except for off-device experiments). For automated analysis of CC3+ or Ki67+ area, Fiji was used to remove non-tumor areas manually (Ki67), to perform background subtraction, to separate the brown staining (color deconvolution plug-in with "H DAB"), and to determine a single manual threshold for positive staining for all of the conditions. For Ki67 experiments, we took 10× images covering each section and used Fiji to divide the images into 100 μm wide images aligned on the center of treatment conditions. Then Cell Profiler[150] was used to determine the overall tissue area, tumor area, and positive staining area, using a previously determined single manual threshold for all images. We focused on 200 μm-wide regions centered on each treatment for each condition.

2.5.14 *Live-tissue staining and post-tissue processing*

For the experiments where we used the Transwell version of the device, we used Hoechst (Invitrogen, 16 μM), Cell Tracker Green CMFDA (Invitrogen, 10 μM), and Cell Tracker Orange CMRA (Invitrogen, 10 μM). After transferring the tissue culture insert containing slices, we aspirated growth medium from the wells, added each of the fluorescent dyes in alternating order, and ran the device at 1.5 mL/hr for 2 hrs.

We aspirated the drug from the well reservoirs 2 hrs before the end of the experiments for drug exposure studies. Subsequently, we filled the empty drug reservoirs with growth medium containing Hoechst (Invitrogen, 16 μM) and SYTOX Green (SG, Invitrogen 0.01 μM), or with

CellEvent (1/1000, Invitrogen) and RedDot 2 (1/400, Biotium), to label the areas that had drug exposure and to assay cell death. After exposure to these solutions for 2 hrs, we changed the medium in all the well reservoirs to PBS for a 30 min wash. After on-device imaging, we transferred the slices to a 6-well plate, fixed with 4% paraformaldehyde overnight, and then cryoprotected with 30% sucrose/PBS overnight two times.

Similarly, for the CRC device experiments, we exposed the slices to Hoechst in the drug delivery channels for the last 2 hrs on the device, then transferred to a 6-well plate and exposed them to CellEvent (1/1000, Invitrogen) for 1 hr. After fixation and cryoprotection as above, we cut the slices in half, perpendicular to the delivery channels, and processed them for cryosectioning (10 μm thickness). For immunostaining, we pretreated tissue sections with 0.6% hydrogen peroxide in methanol for 30 min, washed, and then processed for antigen retrieval by steaming for 30 min in 10 mM sodium citrate, 0.05% Tween 20 (Sigma), pH 6.0. After at least 30-min incubation in blocking solution (Tris-NaCl-blocking buffer or TNB buffer, Perkin Elmer, with 0.1% Triton X-100), we incubated the tissues with rabbit anti-active cleaved caspase 3 (CC3, 1/600, Cell Signaling) or Ki-67 (1/1,000, AbCAM, ab15580) primary antibodies (diluted in TNB) overnight at 4°C. Finally, we incubated the tissues with peroxidase polymers of the appropriate species for 30 min (rabbit from Vector Labs MP7401 or mouse from Biocare MM510) then with the chromogen 3,3'-Diaminobenzidine (DAB, Vector Labs) and lightly counterstained with hematoxylin. We performed all tissue washes with PBS.

We embedded fixed slices in paraffin for off-device CRC experiments, cut 4 μm-thick sections, and placed them on glass slides. After deparaffinization, rehydration, and quenching, we conducted antigen unmasking in 0.01 M citrate buffer of pH 6.0 in a microwave for 10 min. Subsequently, we incubated the slides with CC3 (1/200, Cell Signaling) and Ki67 (1/200, Dako)

primary antibodies. After incubation, we developed the sections with an avidin-biotin technique using the VECTASTAIN Elite ABC kit (Vector Laboratories, Burlingame, CA). Finally, we counterstained the slides with Hematoxylin QS and mounted them with Permount (Fisher Scientific, Santa Clara, CA).

2.6 SUPPLEMENTARY INFORMATION

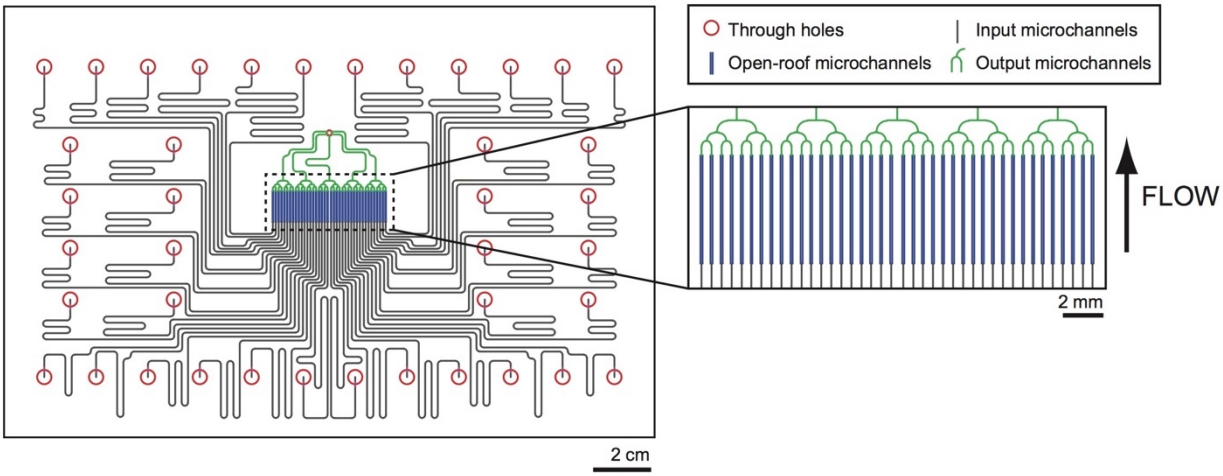

Suppl. Figure 2.1 Oncoslice device channel layer CAD drawings

CAD drawings show the device microchannel layer and the drug delivery area at higher magnification. Through holes (red circles), connect via input microchannels (grey) to the open-roof microchannels (blue), which will be covered and closed by the culture membrane and overlying tissue during device operation. Output microchannels (green) then combine into a single output.

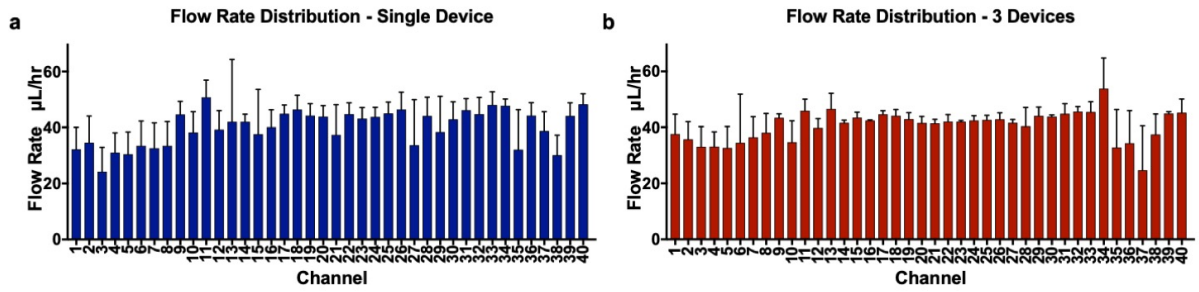

Suppl. Figure 2.2 Flow rate distribution for a single device

(a) Flow rate distribution for a single device. A single device was operated four different times at 1.5 mL/hr (37.5 µL/hr/well) for 10 hrs (error bars show SEM, n=4). **(b)** Flow rate distribution for a set of three devices. Each device was operated three different times at 1.5 mL/hr (37.5 µL/hr/well) for 10 hrs (error bars show SEM, n=9).

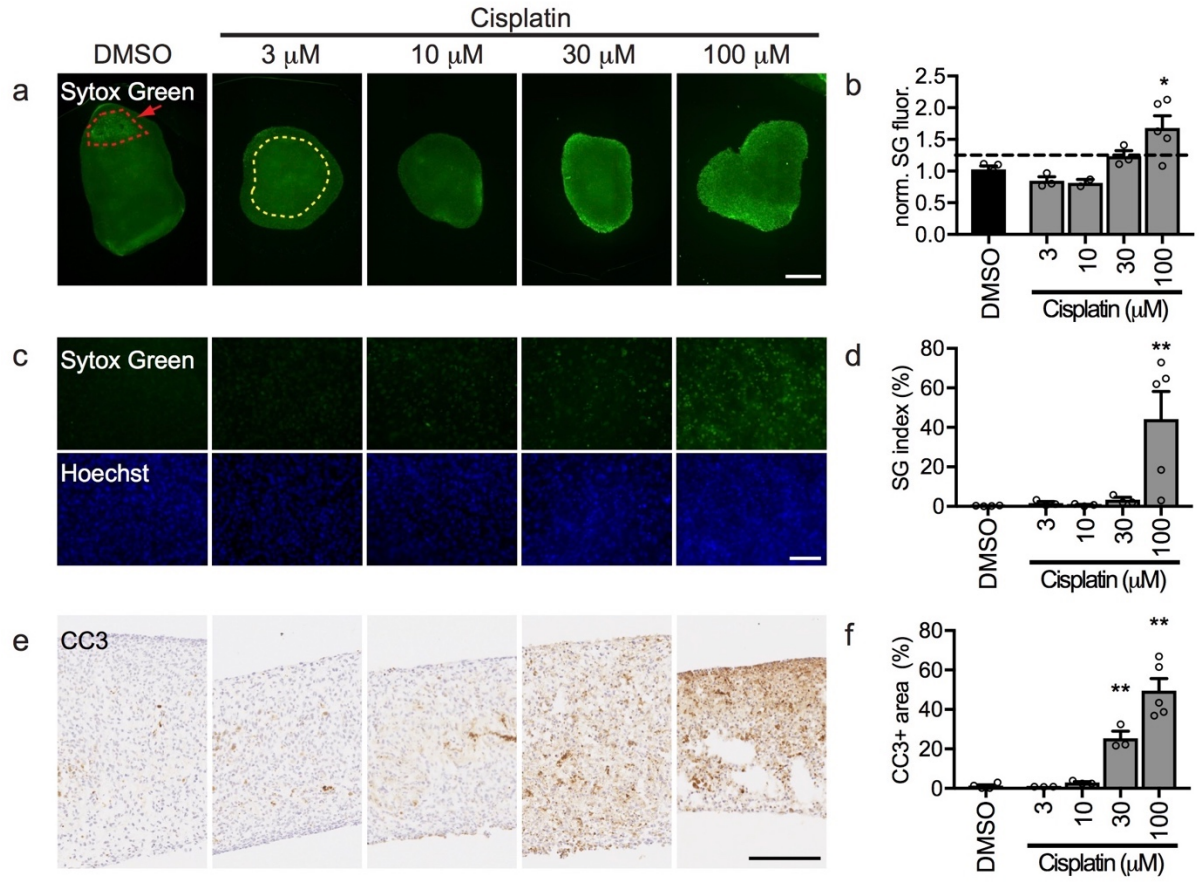

Suppl. Figure 2.3 Dose-dependent increase in cell death after cisplatin treatment of U87 slices in culture

U87 flank tumor slices treated with different doses of cisplatin (CP) from days 1-3 were then exposed to Sytox Green (SG, green dead nuclear stain) and Hoechst (blue nuclear stain) before washing and fixation. We assessed non-specific cell death in low power images (**a**) as overall fluorescence over the central area (dotted yellow line). A positive control crush lesion on the DMSO slice is outlined in red. Treatment with 100 µM CP led to increased cell death, measured as SG fluorescence normalized to DMSO control (**b**). (**c**,**d**) Analysis of high power images showed a similar increase in cell death at 100 µM CP, calculated as an SG index (% SG+ nuclei/all Hoechst+

nuclei). **e,f)** Apoptotic cell death was assessed by CC3+ immunostaining of cross-sections (**e**) and quantified as CC3+ area (**f**), revealing apoptotic cell death at 30 µM as well as at 100 µM CP. Average ± SEM; n=4,3,3,3,5 (**b,d,f)** except n=2 for 10 µM in (**b**). One-way ANOVA versus DMSO with Dunnett's multiple comparison test. *p<0.05, **p<0.01. Scale bar = 1 mm (**a**), 100 µm (**c**,**e**). [123]

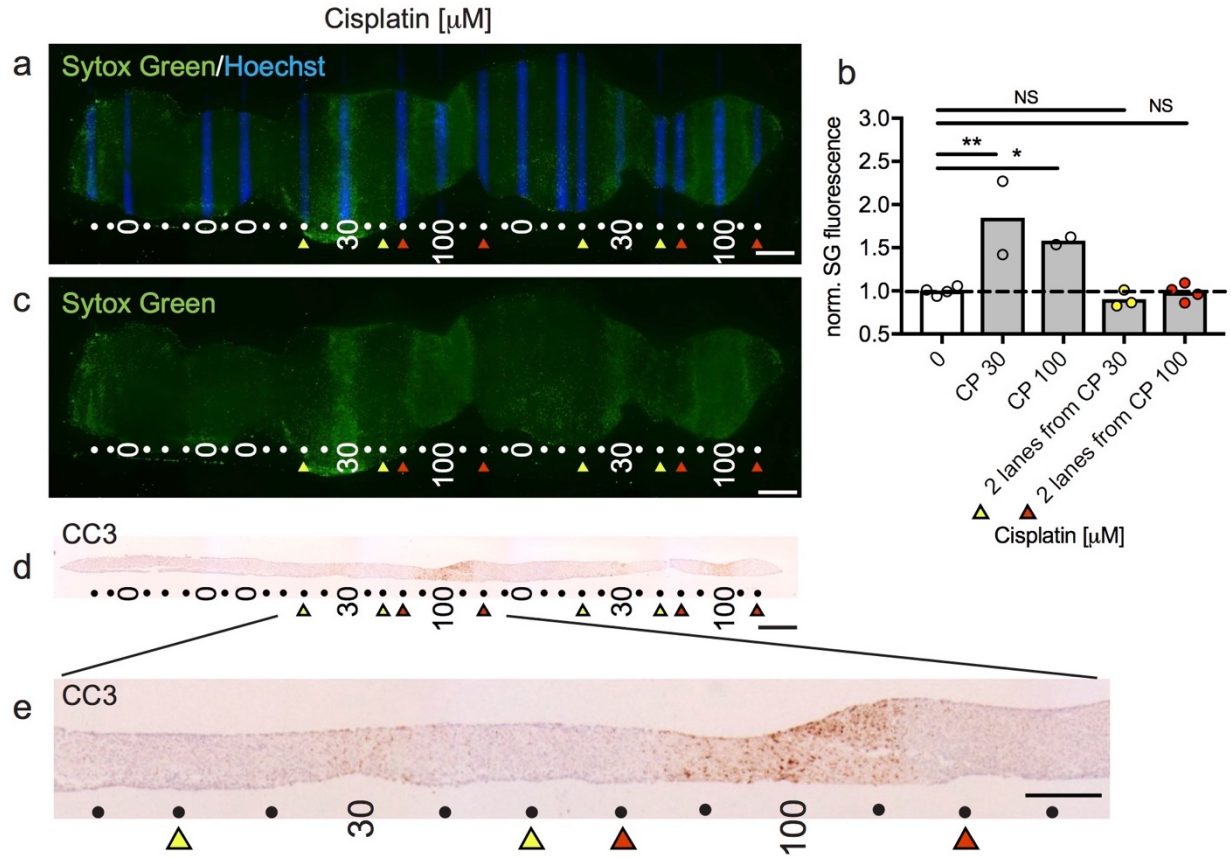

Suppl. Figure 2.4 Restricted lateral spread of cisplatin-mediated cell death in slice cultures on the device.

(a,c) U87 flank xenograft slices were treated with different cisplatin doses (indicated in µM) for 2 d on-device after 1 d off-device, followed by staining with Hoechst dye delivered through drug lanes and SYTOX Green (SG) staining over the entire slice. Yellow and red triangles identify lanes located two lanes over from drug delivery lanes. **(b)** Quantification of cell death by SG fluorescence, normalized to 0 (buffer alone), reveals a significant increase in cell death over drug delivery lanes, but not in lanes located two lanes away (identified by triangles as in panels a and c). **(d,e)** Apoptotic cell death, detected by cleaved caspase 3 (CC3) immunostaining, was limited largely to the drug delivery lane with an only modest lateral spread at the highest concentration tested (100 µM)

that does not reach two lanes away. The graph in **(b)** shows average and individual points. One-way ANOVA versus buffer control, Dunnett's multiple comparison test. *p≤0.05. **p≤0.01. Individual points and average. N=7,3,4,5,5. Scale bar = 1 mm **(a,c,d)**, 500 µm **(e)**.[123]

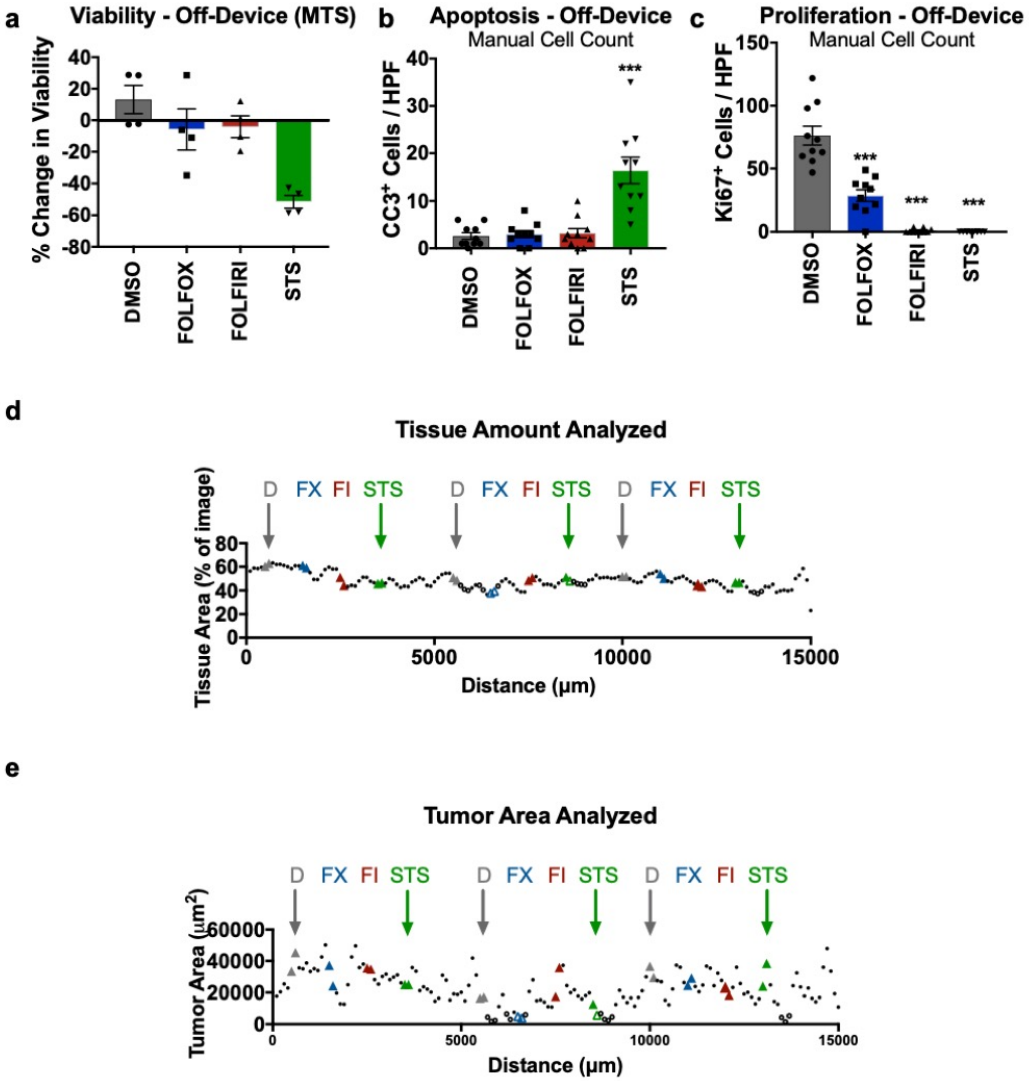

Suppl. Figure 2.5 Off-device analyses for CRC tumor slices

(a-c) Off-device analyses of **(a)** % change in viability as a function of cell metabolic activity (MTS), **(b)** apoptosis by manual cell count of cleaved-caspase 3 immunostaining (CC3), and **(c)** proliferation by manual cell count of Ki67 immunostaining for a colorectal cancer drug slices after three-day drug treatment with 1) (5FU), and

Oxaliplatin, 1 μg/mL each (FOLFOX, FX), or 2) 5FU and Irinotecan, 1 μg/mL each (FOLFIRI, FI). We used DMSO as vehicle control-and STS as a positive control. Four slices per drug condition. N=4 consecutive high-power fields (HPF) counted per condition. Ave ± SEM. One-way ANOVA-versus DMSO with Dunnett's multiple comparison test. *p<0.05, **p<0.01,–***p<0.001. **(d,e)** Tissue sampling from the automated immunostaining analysis of Ki67 in Fig. 8, with quantitation of average tissue area per image **(d)** and total tumor area **(e)** from all six images used for every 100 μm-wide region. Open circles represent less than 10,000 μm^2 for **(e).**

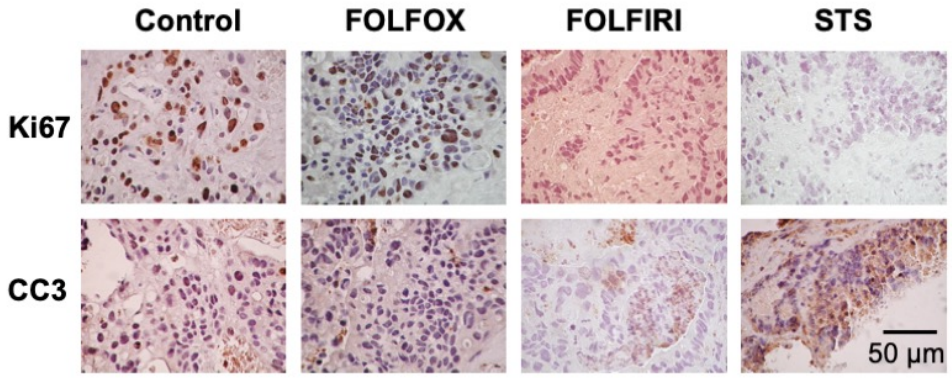

Suppl. Figure 2.6 CRC slice sections showing proliferation and apoptosis

Representative 40x micrographs of perpendicular tissue sections showing proliferation (Ki67) and apoptosis (CC3) for each condition performed off-device.

Chapter 3. "CUBOIDS" FOR MULTIPLEXED MICROFLUIDIC DRUG TESTING OF INTACT TISSUES

3.1 ABSTRACT

As preclinical animal tests often do not accurately predict drug effects later observed in humans, most drugs under development fail to reach the market. Hence there is a critical need for functional testing platforms that use human, intact tissues to predict drug responses. To allow for the multiplexed delivery of many drugs to one small biopsy, we have developed a method for the microscale sectioning of live tissues into large numbers of uniformly sized "cuboids" that feature well-preserved tissue microenvironments. Here we demonstrate the method to micro-dissect mouse liver and mouse xenograft tumors from U87 glioma and characterize the distribution in sizes, viability, and histology of the obtained cuboids. The size uniformity should be appealing to lower heterogeneity in future biological assays and automate their physical manipulation. We have designed a prototype platform consisting of a microfluidic circuit with hydrodynamic traps that allow for immobilizing the live cuboids in arrays at the bottom of a multi-well plate. We demonstrate the proof-of-concept application of model soluble compounds such as dyes (CellTracker, Hoechst) and the cancer drug cisplatin to small arrays of mouse tumor cuboids. The microfluidic platform and dissection method can potentially be upscaled to larger arrays and numbers of cuboids to directly test human tissues at high throughput, which could have an enormous impact on drug discovery and personalized medicine.

3.2 INTRODUCTION

Microdissected tissues (μDTs) from tumors have shown promise recently as an approach that preserves the TME.[23,27,151–153] In 2014, Jahnke et al. demonstrated drug responses in roughly

400 μm fragments manually prepared from patient melanomas (primary and metastases).[152] Two groups showed responses to immune checkpoint inhibitors in multiple cancer types with μDTs created by manually mincing with a scalpel. Kuo's group re-suspended the μDTs in collagen gel and cultured them in Transwells[25–27]. Jenkins and co-workers also re-suspended the μDTs in collagen gel but cultured them in microchannels.[22–24] However, mincing has shortcomings: a) as a manual technique, it results in very heterogeneous μDT sizes; while filtering is an option, it severely reduces the tumor mass available for testing; and b) the μDTs are typically seeded at random, which potentially confounds results (e.g., in secretion assays) because different wells or chambers can have different amounts of μDTs. To address these two issues, Astolfi et al. prepared regularly-sized cylindrical μDTs (380 μm-diam. cores punched from 300 μm-thick PDX tumor slices) and tested their response to a cytotoxic chemotherapy drug within a microfluidic device; they presented a metabolite transport model for μDTs cultured under flow (no hydrogel) in a design with five manually-loaded traps per microchannel and four channels per device.[21] They recently integrated their device (increased to 8 traps per microchannel) with tissue microarray histological analysis and confirmed the integrity of the μDT TME for up to 15 days in culture.[153] None of the above studies/approaches can be easily upscaled to drug testing of large numbers (hundreds) of drug conditions with homogeneously sized μDTs.

While microfluidic approaches to drug testing that use "reconstituted" organs or tissues from dissociated cells (i.e., organ-on-a-chip) have become quite sophisticated,[154–156] microfluidic approaches that use intact tissues remain less advanced.[157,158] We have developed microfluidic platform that miniaturizes functional drug testing on large numbers of live, intact tumor tissue fragments. Our microfluidic trap design is based on the hydrodynamic trap invented by Takeuchi to create arrays of beads,[159] and then adapted to trap single cells,[160] spheroids,[161] or small μDTs[162]

at high efficiency with PDMS devices. However, PDMS is not adequate for drug-based studies; both absorption into PDMS[45–52] and adsorption onto PDMS[53] can potentially alter experimental outcomes by changing the target concentrations and by partitioning molecules in undesired regions of a microfluidic device. Thus, we fabricated Takeuchi traps in poly(methyl methacrylate) (PMMA) laminates by laser cutting, an approach made feasible by the larger dimensions of our microchannels and traps. Furthermore, existing microchannel trap devices for cells or organoids remain closed after trapping,[157,163] and generally permit treatment of all trapped elements with the same medium/drug condition. While one could create multiple treatment conditions with valves and additional microfluidic circuitry to deliver different solutions, these approaches create even more complex devices and operations. In our device, the traps are only closed during loading; after trapping, removal of the trap roof layer opens a window above each cuboid. Subsequent application of a multi-well grid allows for top-loading each well with different drug treatment by simple pipetting. Here, we demonstrate the feasibility of the approach with an 8-well design capable of trapping three cuboids per well (total 24 cuboids). The design is potentially scalable to a 96-well (or larger) format, opening the possibility for large-scale drug testing with human donor tissue in the near future. **The work presented in this chapter has been reproduced from our Lab on a Chip publication[39] with permission from The Royal Society of Chemistry.**

3.3 Results and Discussion

3.3.1 *"Cuboid" sectioning procedure*

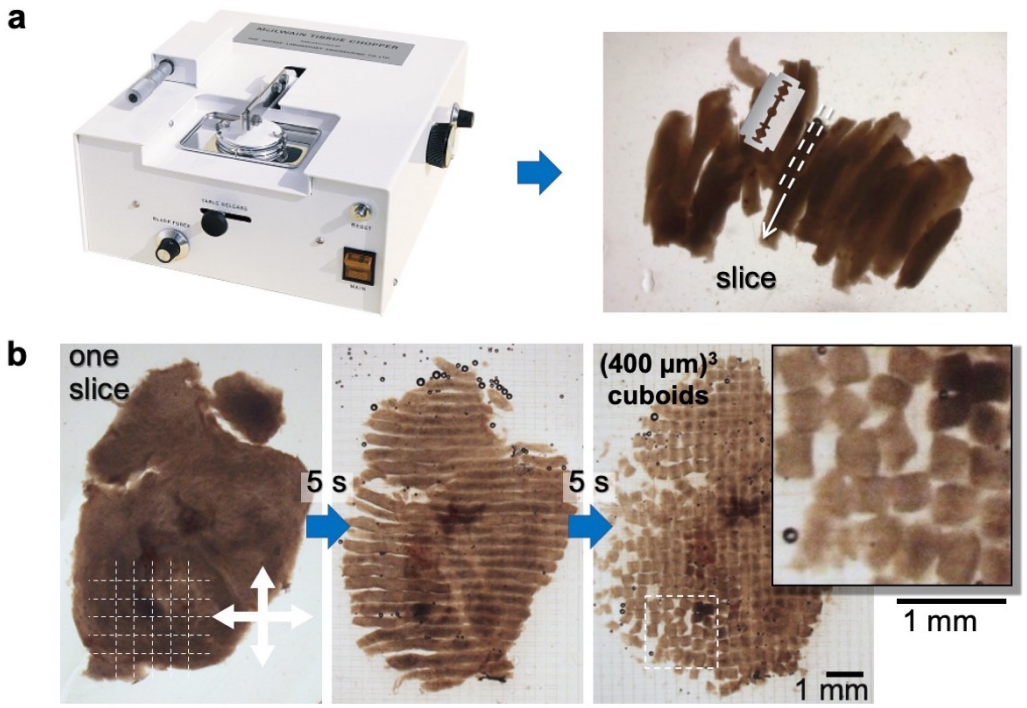

Figure 3.1 "Cuboid" sectioning procedure

a) McIlwain-type tissue chopper and example of ~ 400 µm – thick glioma slices. b) Cuboid sectioning procedure showing consecutive orthogonal slicing procedure starting with a single 400 µm – thick slice.

We have developed a procedure to micro-dissect live biopsy specimens (i.e., tumor resection) into thousands of similarly sized, cuboidal-shaped tissue pieces (named "cuboids"). The method consists of placing a tissue sample onto the specimen plate of a mechanical (McIlwain-type) tissue chopper and performing a series of cuts: the first one generates slices (**Fig. 3.1a**); all the slices from the first cut are next placed flat on the cutting plate and sliced in one direction, then immediately in the orthogonal direction (**Fig. 3.1b**). In this tissue slicer, the blade comes down and retracts fast enough, such that the process can be performed in a few minutes (ensuring optimal tissue viability) to produce hundreds of cuboids of homogenous size. The number of cuboids obtained depends on the initial sample volume and the target size of the cuboids.

We have focused on studying cuboids that are ~ 400 μm × 400 μm × 400 μm because, from organoid literature, organoids between 300-600 μm have been utilized for a variety of solid tumor types with success.[20,164] Larger and smaller cuboids can also be made with this process and could also be of interest, e.g., to understand the effect of hypoxia (larger cuboids) and to obtain higher throughputs (smaller cuboids). However, here we chose a size that maximally preserves the features of the TME but still maintains viability from nutrient delivery and minimizes the development of necrotic cores. Additionally, the accuracy of the initial cut of a chuck of tissue to slices (best with height less than 4 mm and aspect ratio <1) was less accurate at 400 μm, such cuboids of smaller size would be more precisely generated by vibratome sectioning for this first step. We chose to make symmetrical cuboids to facilitate use with microfluidics. **Table 1** shows the number of expected cuboids per cm^2 as a function of their size. Thus, a small tumor from which four or more 1 cm-diam. slices could be obtained on the first cut theoretically would yield up to a few thousand cuboids $(400\ \mu m)^3$ in volume. Finally, passage through mesh filters of defined dimensions can enable enrichment for pieces of a particular size range by preferentially removing pieces that are too big (e.g., remain attached) or too small (e.g., from the edges from pieces that break up during processing).

Table 3.1 Total number of cuboids per unit area

Cuboid size	$(200\ \mu m)^3$	$(300\ \mu m)^3$	$(400\ \mu m)^3$	$(500\ \mu m)^3$
# cuboids / cm^2	2,500	1,111	625	400

`

3.3.2 *Mouse liver and glioma cuboid analyses*

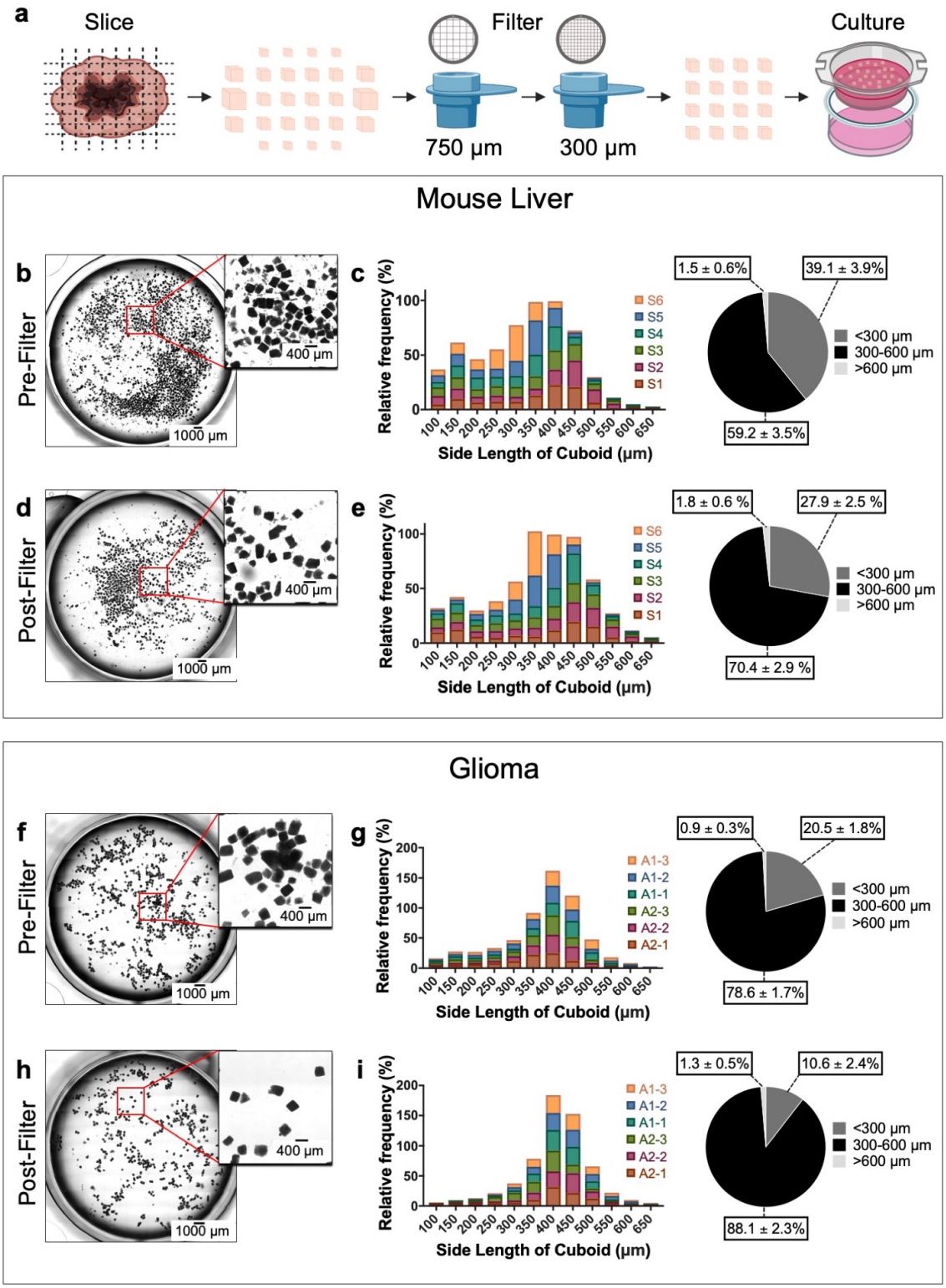

Figure 3.2 Mouse liver and glioma cuboid size analysis

(a) Cuboid slicing and filtering process overview. Size distribution analysis of mouse liver **(b-e)** and glioma cuboids **(f-i)**. Sample images showing cuboids before **((b)** mouse liver, **(f)** glioma) and after filtering (**(d)** mouse liver, **(h)** glioma**).** Summary of size distribution shown as relative frequency (%, histogram) and as frequency average of all samples (%, pie chart) for sizes <300 μm, 300-600 μm, >600 μm before (**(c)** mouse liver**, (g)** glioma) and after (**(e)** mouse liver, **(i)** glioma)**).** Each "sample" consisted of a set of 11-17 slices (~1 cm^2 total area) that were processed together, from cutting further into cuboids and to filtering, with up to 3 samples per tumor/liver. The total number of cuboids pre-filtering per sample ranged from 650-1150 for liver and from 500-900 for glioma. N=6 samples each for both mouse liver and glioma. Pie chart data shows averages ± SEM.

We aimed to characterize the distribution of cuboid sizes and yield of our microdissection process (**Fig. 3.2a**). For this purpose, we analyzed freshly microdissected mouse liver (**Fig. 3.2b-e**) U-87MG (U87) glioma cell-derived xenograft flank tumors (**Fig. 3.2f-i**) before and after filtering. We focused our interest on cuboids in a size range of 300-600 μm, as previous studies have used organoids within this size range.[20,164]

Notably, we observed different size distributions between mouse liver and glioma cuboids, probably due to the differences in consistency and density between liver and glioma. For mouse liver samples, we observed large quantities of liver tissue fragments before filtering and found that 39.1 ± 3.9% of the cuboids were smaller than 300 μm, while 59.2 ± 3.5% were in the desired size range (300-600 μm) (**Figs. 3.2b, c**). The filtering steps shifted the size distribution to the size of interest by removing 11.3 ± 5.7% of the small liver cuboids and fragments **(Figs. 3.2d, e**). Accordingly, we found that 70.4 ± 2.9% of the remaining liver cuboids were in the size of interest. We observed a small percentage of liver cuboids bigger than 600μm before (1.5 ± 0.6%) and after filtering (1.8 ± 0.6%).

On the other hand, for glioma cuboids, we observed that a smaller percentage (20.5± 1.8%) had a size below 300 μm and 78.6 ± 1.7% were in the desired size range before filtering (**Figs. 3.2f, g**). Compared to mouse liver samples, we did not observe as much tissue fragmentation during

the microdissection process, as with the liver, the filtering steps isolated 9.96 ± 1.46% of the small glioma cuboids. Consequently, we found that 88.1 ± 2.3% of the remaining glioma cuboids were in the desired 300-600 μm size range. As with mouse liver cuboids, a small percentage of glioma cuboids were larger than 600 μm before (0.9 ± 0.3%) and after filtering (1.3 ±10.6%).

In addition to size distribution, we investigated how much of the initial mouse liver and the glioma tissue sample is lost in each microdissection step of the process (**Suppl. Fig.3.2**). We found that, in the end, cuboids of the desired 300-600 μm size range represented 34.2 ± 4.3% and 48.2 ± 8.4% of the initial mouse liver and glioma tissue samples, respectively (**Suppl. Fig 3.2b, c**). Our data indicate that the mechanical microdissection step had similar tissue loss for both mouse liver (20.1 ± 4.1%) and glioma (21.1 ± 10.5%). Similarly, we found that the filtering step resulted in an additional 32.4 ± 8.0% tissue loss for mouse liver and 24.7 ± 2.7% for glioma samples. As expected, most of the sample was lost after the dissection and filtering steps, attributing to a total of 52.5 ± 3.0% and 45.9 ± 9.4% tissue loss of the initial mouse liver and glioma samples, respectively. Finally, to further understand the filtering process's effectiveness, we also investigated how much of the initial pool of 300-600 μm cuboids were retained after filtration. We found that there was a 51.2 ± 2.7% and 70.0 ± 5.0% 300-600 μm cuboid retention for mouse liver and glioma, respectively.

Our results indicate that we can create microdissected cuboids from intact tissues within the desired size range. We highlight the importance of size distribution and sample yield as we look forward to biological experiments with our microfluidic platform. Having a pre-selected pool of cuboids with homogenous size and shape is critical to mitigate variability in cytotoxicity testing.[165,166] With the current cuboid sectioning procedure, we had a high percentage of cuboids within the desired size range, and we can demonstrate the potential of this approach in later

sections. We were also able to pinpoint steps in the procedure that need optimization. Our microdissection process needs improvement to decrease the percentage of cuboids outside our desired size range. Cuboids with dimensions smaller than 300 μm and bigger than 600 μm pose risks associated with the performance of our microfluidic device (shown below). We have found that tissue fragments with sizes between 100-150 μm could directly impact cuboid trapping efficiency by obstructing and clogging the microchannels connecting the traps to the bypass channel. Additionally, cuboids with sizes between 150-250 μm would potentially allow trapping of multiple cuboids as their size is not big enough to fill the traps. On the other hand, cuboids larger than 600 μm can block the bypass channel curves, resulting in cuboid congestion and aggregation.

To solve the challenges associated with small cuboids and fragments, we can further optimize our filtering procedure. Our results indicate that the filtering process only had a slight reduction of cuboids smaller than 300 μm for both mouse liver and glioma tissues. Additional filtering stages can be incorporated to improve our procedure. By following a similar analysis to the one presented above, we could identify if repeated filtering promotes a higher decrease in the percentage of small cuboids. On the other hand, we found that cuboids larger than 600 μm resulted mainly from tissue aggregation and partial dissections. This problem can be solved by adding gentle enzymatic treatments such as collagenase or DNase.[20,27] Overall, we expect to improve our cuboid microdissection to increase size homogeneity while maximizing sample yield with the proposed solutions.

3.3.3 *Characterization of the cuboid microenvironment*

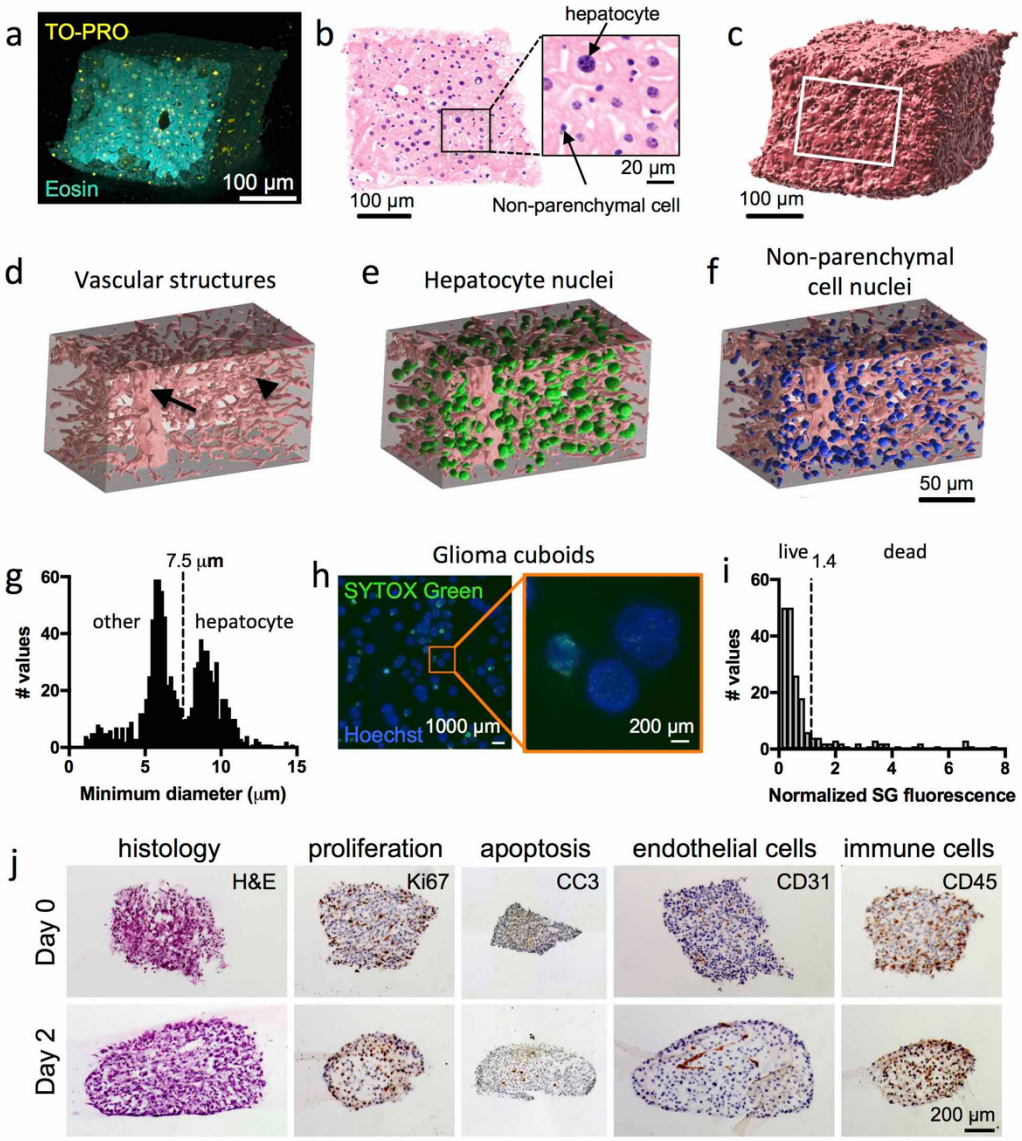

Figure 3.3 Characterization of the cuboid microenvironment

(a-f) 3D imaging of liver cuboid by light-sheet microscopy (TO-PRO, yellow; eosin, blue). **(a)** 3D rendering**.** **(b)** False-colored H&E of top view slice showing parenchymal cell hepatocytes (arrows) and smaller, non-parenchymal cells in the inset. **(c)** 3D rendering of the surface of a cuboid. **(d)** 3D rendering of the vascular space ("vascular "structures) within a central region of the cuboid as indicated by a white box in **(c)**. Large vessel (arrow) and smaller vascular structures (arrowheads). **(e)** 3D rendering of the larger nuclei ("hepatocyte")

superimposed on the vascular space. **(f)** 3D rendering of the smaller nuclei ("non-parenchymal") superimposed on the vascular space. **(g)** Histogram of nuclear size distribution from the same liver cuboid, using the diameter along the shortest axis of a bounding box. **(h)** Viability staining of live U87 glioma cuboids after three days in culture. Dead nuclei stain with SYTOX green (SG, green) and all nuclei stain with Hoechst (blue). **(i)** Histogram of mean SG fluorescence after normalization to average (N=188). The dotted line indicates a fluorescence threshold of 1.4. **(j)** U87 glioma cuboids before (day 0) and after time in culture in collagen hydrogel (day 2), showing histology and immunostaining for proliferation, apoptosis (cleaved-caspase 3, CC3), endothelial cells, and immune cells. Representative images from experiments on three different tumors.

To visualize the 3D tissue microenvironment inside the cuboids, we performed open-top light-sheet (OTLS) microscopy of fixed and optically cleared liver cuboids (**Fig. 3.3a-f**). OTLS microscopy offers high-throughput 3D imaging in a configuration easily compatible with culture dishes or devices[167–169]. Vibratome slices of liver were cut into cubes with the tissue chopper, suspended in collagen, and fixed after gelation. We performed staining with far-red fluorescent TO-PRO 3 nuclear dye and fluorescent eosin, ethyl cinnamate clearing, and LSM as according to refs.[168,169]. Optical clearing, which often involves tissue dehydration and solvent exchange, can significantly shrink the tissue (potentially ~50%[170]). The fluorescent images revealed that while the cuboid's outer edges had ~1-3 layers of dead or dying cells (an expected acute response of the fragile liver to the cutting procedure), most of the cuboid interior appears undamaged (Fig. 3a). All sides were similar, suggesting that chopping did not cause worse tissue damage than the gold-standard vibratome. Using simple image processing, one may generate false-colored images that mimic the traditional H&E (hematoxylin and eosin) stain[171] (**Fig. 3.3b**). The large hepatocytes (parenchymal cells), nuclei of smaller non-parenchymal cells (including Kupffer cells, stellate cells, and endothelial cells, among others), along with the liver sinusoids and other vascular structures, can all be observed (**Fig. 3.3a,b**). By 3D image analysis of three cuboids with a

combination of FIJI and Imaris, we identified the cuboid surface, vascular spaces, and cell nuclei (**Fig. 3.3c-f**). We limited our analysis to the central regions for the vascular spaces and nuclei as the morphology was altered in the areas nearer the surface. With this approach, we could quantify the number of cells (nuclei) per cuboid, which could be valuable for normalizing the mass in pharmacological assays and their relative location, which could be exploited for spatial assays with labeled cells. Using the Imaris surface module, we calculated an average volume of the three cuboids of 0.025 ± 0.002 mm^3. In the smaller central regions of the cuboids (0.0028 ± 0.00014 mm^3), the vasculature occupied 7.9 ± 2.2% of the volume, and the nuclear density was 311,000 ± 17,000 nuclei/mm^2. Using the bimodal size distribution of the nuclei from the two cuboids with best-preserved morphology (**Fig. 3.3g**), we classified the larger nuclei as hepatocytes (parenchymal cells) and the smaller nuclei as non-parenchymal cells (size threshold of 7.5 μm). This division was consistent with the nuclear size ranges and locations we observed for hepatocyte and non-parenchymal cells in the original 2D images. For the three cuboids, hepatocytes represented 44 ± 4% of the nuclei, not far from the ~52% reported in a 2D study of mouse liver sections[172]. In the future, fluorescently labeled cells and other fluorescent labels (endogenous or exogenous) can be added to provide additional biological readouts, both for fluorescent 3D analysis of fixed tissue (as performed here) or for two-photon/confocal microscopy of living tissues.

We next evaluated the viability and microenvironment of U87 glioma cuboids after two days in culture. For these experiments, we cultured the cuboids within a collagen hydrogel layer on top of a Transwell insert, with an air interface above and medium below, as described by Neals et al. for microdissected tumor pieces[27]. By day 2, the cuboid shape relaxed to that of a spheroid. First, we performed live viability staining of the cuboids using the green, fluorescent dead nuclear

stain, SYTOX green (SG), and the blue fluorescent pan-nuclear stain, Hoechst (H), after three days in culture (**Fig. 3.3h).** Most of the cuboids show minimal SG dead stain (fluorescence normalized to the mean), but ~15 % were relatively green (dead) (two separate experiments with ~16% at day three and day 4) (**Fig. 3.3h,i, Suppl. Fi. 3.2**) The threshold for death was the mean increase (1.4) seen after a-day maximal drug treatment (100 μM Cisplatin) (**Suppl. Fig. 3.2**). After fixation, staining of thin histological sections also revealed preservation of the cuboid viability (**Fig. 3.3j**). Traditional H&E staining showed similar histology between the cuboids and the initial tumor. Immunostaining revealed continued proliferation (Ki-67) and minimal apoptosis (anti-cleaved caspase 3, CC3), usually central if present. Finally, immunostaining for different cells of the microenvironment demonstrated the continued presence of endothelial cells (CD31) and immune cells (CD45) (**Fig. 3.3j**). These results support the potential of cuboids as an intact tissue model for drug testing.

3.3.4 *Microfluidic device design and operation*

The regular, small size of the cuboids makes them amenable to microfluidic hydrodynamic trapping. To trap the cuboids, we chose the Takeuchi design[173] because it traps nearly every particle entering the network until all of the traps are filled (**Fig. 3.4a,b**). Flow diverts particles from the main channel into individual trap channels when they are empty and not filled. Alternative versions by others, all made in PDMS, can trap cells[160] or spheroids of less than 200 μm diameter[42,43]. To iterate the design of our first prototypes and to rapidly test various trap and chip layouts, we used stereolithographic 3D Printing until we settled on our final trap and chip design (see **Suppl. Fig. 3.3**). To avoid resin leaching issues and to facilitate the integration of removable layers (which are needed for hydrodynamic seeding of the cuboids), we fabricated the final design

in PMMA laminates, following our published laser-cutting and PMMA bonding protocols[32]. A 3D CAD drawing (**Fig. 4c**) shows the PMMA microfluidic channel network and traps' basic design.

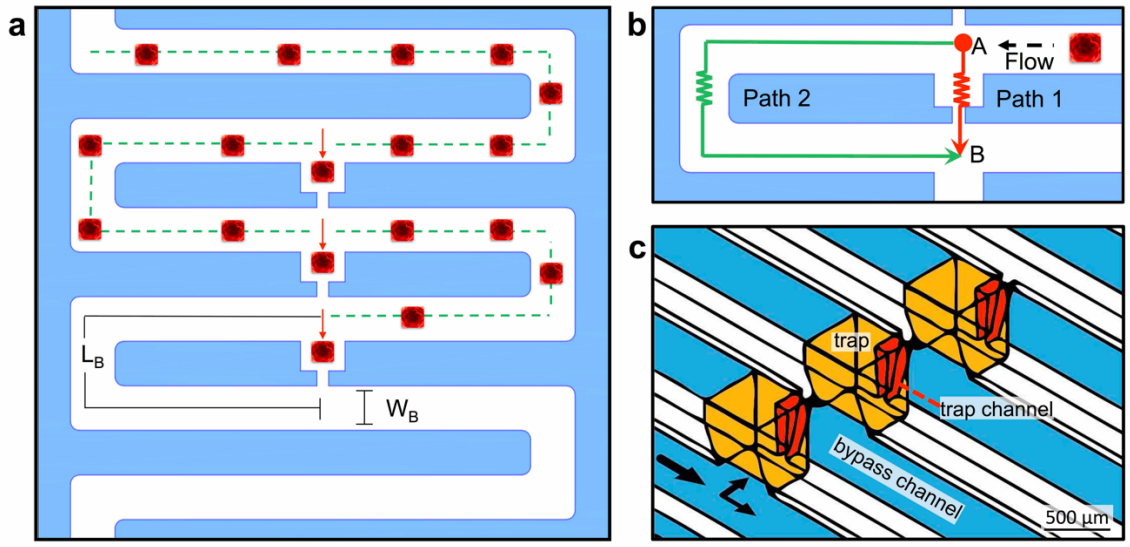

Figure 3.4 Microfluidic trap design

(a) Schematic representation of the trap design corresponding to one well and its three traps. The traps' flow resistance is lower than that of the bypass channel, but if a cuboid (red) becomes trapped, the next cuboid in the flow will continue through the bypass channel. The width and length of the bypass channel are W_B and L_B, respectively. **(b)** Close-up of one trap. Lower hydraulic resistance through path 1 (R_T in the trapping channel) versus through path 2 (R_B in the bypass channel) leads to greater flow from point A to point B through the trap. **(c)** 3D CAD drawing of the traps and microchannels in the PMMA device, with a closeup view of three adjacent traps.

Our microfluidic device enables the trapping of intact cuboidal micro-tissues into addressable wells/traps for culture and multi-drug exposures (including cell-based therapies). The multistage design consists of a loading stage and a culture stage (**Fig. 5**a). The device comprises four functional components for both operation stages, not including the lid and a base for culture. These components are: 1) a removable polysil silicone adhesive roof (for the loading stage) or a

bottomless 8-well plate (for the culture stage, attached after loading), 2) a microfluidic channel layer, 3) a sealing layer for the bottom surface of the channel network, and 4) a set of inlets.

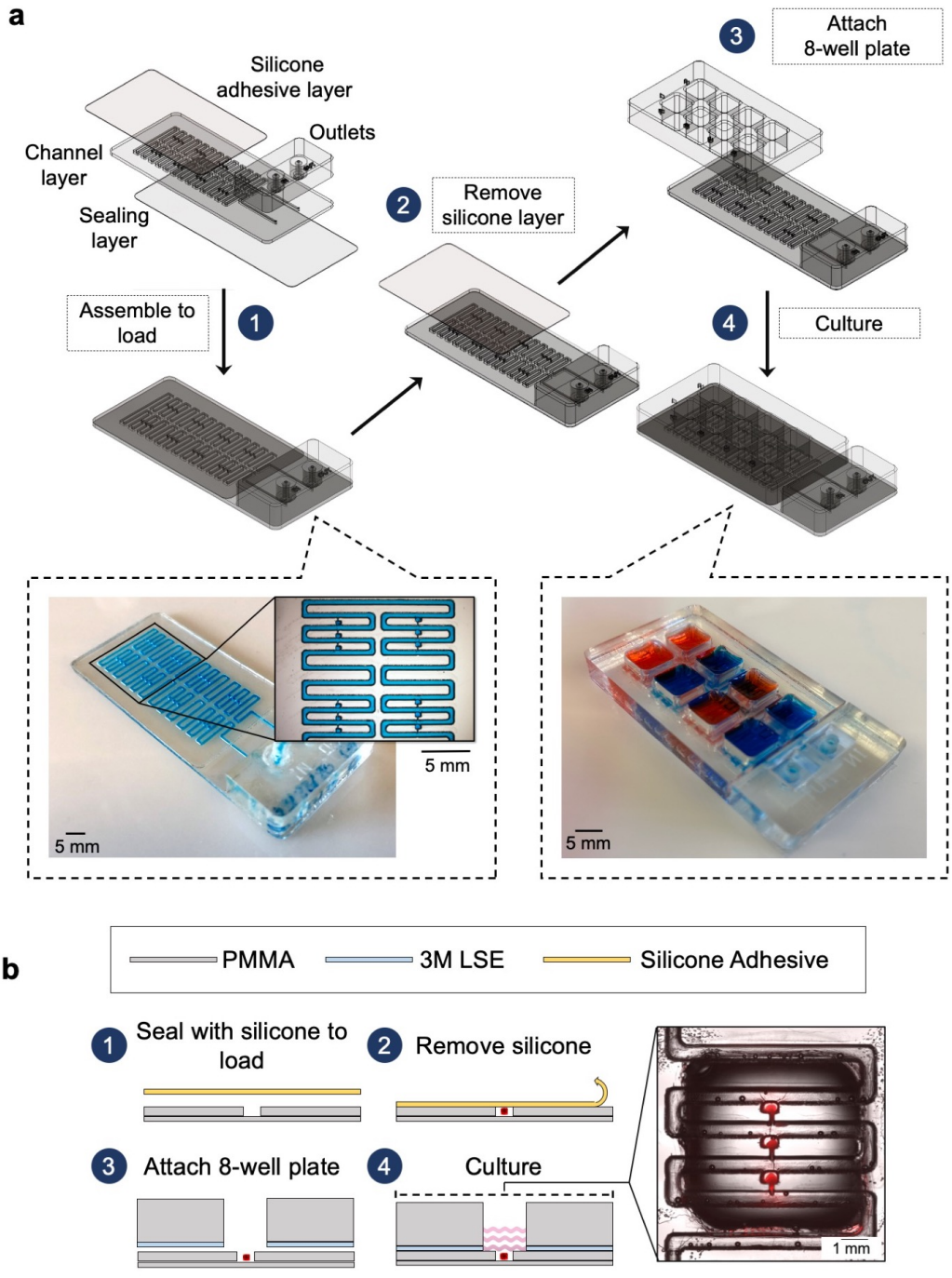

Figure 3.5 Microfluidic device design and operation

(a) Multistage design of the microfluidic device, with a loading stage (**1**-**2**) and a culture stage (**3**-**4**). 3D renderings of device components, as well as micrographs of a device ready for loading (filled with blue dye) and of a device ready for culture (wells filled with red and blue dyes). **(b)** Cross-sectional view of the same multi-step operational

procedure as in **(a)**. Inset shows a top view of trapped glioma cuboids (fluorescently labeled with CellTracker-red) in a single well of the microfluidic device.

We fabricated the device using a combination of CO_2 laser micromachining, solvent bonding, thermal bonding, and transfer adhesive techniques. For CO_2 laser micromachining, we determined different optimal CO_2 laser power and speeds for each specific width and depth of the cuboid traps and microchannels (**Suppl. Fig. 4**). Chloroform treatment before bonding promoted the PMMA components' bonding and improved the optical clarity and reduced surface roughness (**Suppl. Fig. 5**, **Suppl. Fig. 6**)[75,132]. The irreversible bonding procedure for the PMMA components (except for the silicone adhesive) produced a leak-proof platform.

The microfluidic device design necessitates two stages of operation. The main microchannel connects the eight wells in series. Each well contains three cuboid traps in the final culture configuration that each open from the top to the well and remain connected to the main microchannel. Due to this incompletely closed channel architecture (the traps are open to the atmosphere), effective flow through the microchannels necessitates the closure of the trap roofs. Therefore, before we load the traps with cuboids via the microchannels, we temporarily seal the open traps with removable silicone adhesive tape to enable flow (**Fig. 5**a). We then load the cuboids in a collagen suspension, which, once gelled, immobilizes them and creates the collagen/hydrogel culture environment. After loading, we remove the silicone tape and replace it with the bottomless 8-well plate (containing adhesive), leaving the traps open. Note that, while it would be technically possible to load each trap manually in our small prototype device by pipetting into each trap, we seek a high-throughput solution that could potentially solve the problem of loading thousands of cuboids.

We based our microfluidic approach for cuboid entrapment on Takeuchi's design, which exploits hydrodynamic principles to achieve the serial entrapment of particles, initially performed

on beads[174]. Our microfluidic design (**Fig. 4**a,b) consists of a continuous bypass channel (W_b = 315 ± 9 μm, W_t = 721 ± 12 μm, h = 672 ± 10 μm) and a series of lower resistance trapping channels. These trapping channels contain a trapping section/well (W= 737 μm, h = 1,000 μm) and a narrower channel (W_b = 99 ± 5 μm, W_t = 181.6 ± 0.1 μm, h = 712 ± 54 μm). The top and bottom dimensions reflect the approximately trapezoidal profiles created by our laser-cutting protocol (**Suppl. Fig. 6**). With this microfluidic network design, flow "prefers" to go through the open traps (**Fig. 4**b, path 1) but, when flow brings a particle into a trap, the particle blocks the flow and diverts the flow to the next trap (**Fig. 4**b, path 2). The hydraulic resistance ratio of the two fluidic paths governs the relative flow rates (Q_B & Q_T) through the fluidic circuits. The hydraulic resistance (R) is directly related to the geometric parameters of the channel. Channels made with CO_2 laser engraving have a trapezoidal geometry with a constant depth and (h), defined by the laser cutter's power and speed parameters.

As reported by Takeuchi et al., we applied the Darcy-Weisbach equation to approximate the resistance of the trapezoidal microchannels:

$$\Delta P = \frac{fL\rho V^2}{2D}$$

Equation 3.1 Darcy-Weisbach pressure drop equation

where f is the Darcy friction factor, L is the length of the channel, ρ is the fluid density, V is the average velocity of the fluid, and D is the hydraulic diameter, respectively[173,174]. D for a trapezoidal microchannel can be further expressed as

$$D = \frac{h(W_b + W_t)}{W_b + 2\sqrt{\frac{W_t - W_b}{2} + h^2}}$$

Equation 3.2 Hydraulic diameter of a trapezoidal microchannel

where h is the height and W_b and W_t are the bottom and top widths of the microchannel, respectively. The Darcy friction factor, f, is related to the aspect ratio of the microchannels (W_b / W_t) and the Reynolds number:

$$Re = \frac{\rho V D}{\mu}$$

Equation 3.3 Reynold's number

where μ is the fluid viscosity. The following expression[175] has been widely used to predict the friction constant for fully developed laminar flow in rectangular microchannels of aspect ratio α (width/height):

$$fRe = 96(1 - 1.3553\alpha + 1.9467\alpha^2 - 1.7012\alpha^3 + 0.9564\alpha^4 - 0.2537\alpha^5)$$

Equation 3.4 Laminar friction constant equation for rectangular microchannels

Similarly, other groups have investigated a similar expression to estimate the friction constant for trapezoidal microchannels. Cheng et al. experimentally obtained the following expression[176] to correlate the laminar friction constant of trapezoidal microchannels in terms of the cross-sectional aspect ratio (W_b / W_t):

$$fRe = 11.43 + 0.80 \exp\left(\frac{2.67\ W_b}{W_t}\right)$$

Equation 3.5 Laminar friction constant estimation of trapezoidal microchannels

Since the traps in our microfluidic device have a rectangular shape, we utilized both expressions to estimate the pressure drop along path 1. After applying the Darcy-Weisbach equation, we were able to calculate the hydraulic resistance along the two paths and found that $R_B/R_T = 1.26$, implying that the flow rate through the trapping path (Q_T) will be ~1.26x higher than the flow rate through the bypass path (Q_B).

`

These results prompted us to find alternative methodologies to predict the pressure drop in our trapping system. Culham et al. describe an alternative method to calculate the pressure drop of fully developed laminar flow in microchannels of arbitrary cross-section (within 8% accuracy).[177] This model is only a function of geometrical parameters of the cross-section (i.e., area, perimeter, and polar moment of inertia). This approximation was achieved because torsion beams and fully developed laminar flow in ducts are similar, as shown by Poisson's equation. Their pressure drop approximation is based on the solution for an elliptical duct due to the unique geometrical property of its velocity solution and polar moment of inertia about its center:

$$\Delta P = \frac{16\pi^2 \mu V}{A} I_p^*$$

Equation 3.6 Polar moment of inertia of elliptical geometry

where $I_p^* = I_p / A^2$ is a non-dimensional geometrical parameter known as the specific polar moment of inertia. For a trapezoidal microchannel, the area, perimeter, and polar moment of inertia (about its center) are:

$$A = \frac{h}{2}(W_b + W_t)$$

$$P = W_b + W_t + 2h$$

$$I_p = \frac{h}{144(W_t + W_b)}\{(W_t + W_b)[3(W_t + W_b)^2 + 4h^2] + 16h^2 W_t W_b\}$$

Equation 3.7 Polar moment of inertia of a trapezoidal microchannel

The polar moment of inertia can be simplified by incorporating the aspect ratios ε and β where

$$\in \equiv \frac{W_t + W_b}{2h}$$

`

$$\beta \equiv \frac{4W_t W_b}{(W_t + W_b)}$$

resulting in:

$$I_p^* = \frac{I_p}{A^2} = \frac{2(3\,\epsilon^2 + 1) + \beta(1 - 3\,\epsilon^2)}{36\,\epsilon}$$

Equation 3.8 Simplified moment of inertia of a trapezoidal microchannel

We calculated the pressure drop and along the two paths with this model and found that the hydraulic resistance ratio $R_B/R_T = 2.67$. This result still implied a preferential flow (Q_T) through path 1, as expected.

Although these two models resulted in different predictions, we could still successfully trap cuboids in our microfluidic device (Fig 2.4h). These two models could be easily applied for future iterations of the device. The relative flow rate through the trapping path could increase the resistance through the bypass path and decrease the trapping path's resistance. In principle, this could be achieved by merely altering the channel's width and height. Table 2.2 shows an example of an alteration to the bypass and trap channels' heights, respectively.

Table 3.2 Hydraulic resistance ratios (RB/RT) after geometrical channel alterations

	1	**2**	**3**
Height Bypass	650 µm	650 µm	650 µm
Height Trap Channel	750 µm	800 µm	850 µm
RB/RT: Darcy-Weisbach	1.64	1.92	2.37
RB/RT: Calhum et al. Ellipse	3.14	3.39	3.63

Because laser cutting yields channels with complex geometry, we turned to more realistic finite volume modeling of fluid flow in the device to inform key decisions related to the design and operation of the device. In particular, we wanted to more accurately assess the path taken by

the cuboids for each of the three traps (**Fig. 6**a-c). We created a 3D AutoCAD model of our device (**Fig. 6**a) using measurements from assembled devices (**ESI. Fig. S6**). Using Ansys Fluent, we modeled the velocity and flow profiles over the whole device assuming a trap configuration with groups of three adjacent traps (**Fig. 6**a), as well as a control configuration with traps separated by an extra length of microchannel (**Fig. 6**b). Using the Ansys model, we incorporated the complex 3D geometry and hydrodynamic properties of the fluid, including viscosity and flow rate. Prior studies that utilized the Takeuchi method calculated the ratio of resistance in the two paths (bypass and trap) to predict the relative flow ratios[159,174,178] – an approach that did not take into account the influence of downstream traps. Calculation of the flow ratio Q_T/Q_B for the first three traps revealed dramatically different results for the two different configurations (**Fig. 6**c,d). The Q_T/Q_B ratio for the control configuration was 0.72 for all three traps, which suggested that the traps would not function. In contrast, the Q_T/Q_B ratios for the adjacent-trap configuration were over 1 (1.16, 1.39, 1.22), which suggested functional traps and that the second trap would be the most efficient of the three traps. A key factor for experiments with intact-tissue cuboids is their high density (higher than that of cells), which causes a high speed of sedimentation and can lead to settling and friction at the bottom of the microchannel. Note that because of their rectangular profiles they do not roll, as would spheroids. Therefore, use of denser solutions (which also tend to be more viscous), such as collagen (1.013 g/mL and ~50 mPa.s[179]) or polyethylene glycol (PEG) solutions (20% PEG is 1.04 g/mL, μ = 15 mPa.s[180]), might minimize sedimentation and friction and improve trapping efficiency. If high viscosity becomes a problem, Percoll solutions could, in principle, be used for trapping to make solutions with high-density and relatively low-viscosity (1.05 g/mL and $\mu \approx 2.5$ mPa.s[181]), as used previously to hydrodynamically trap stem cell-derived cellular aggregates.[182]

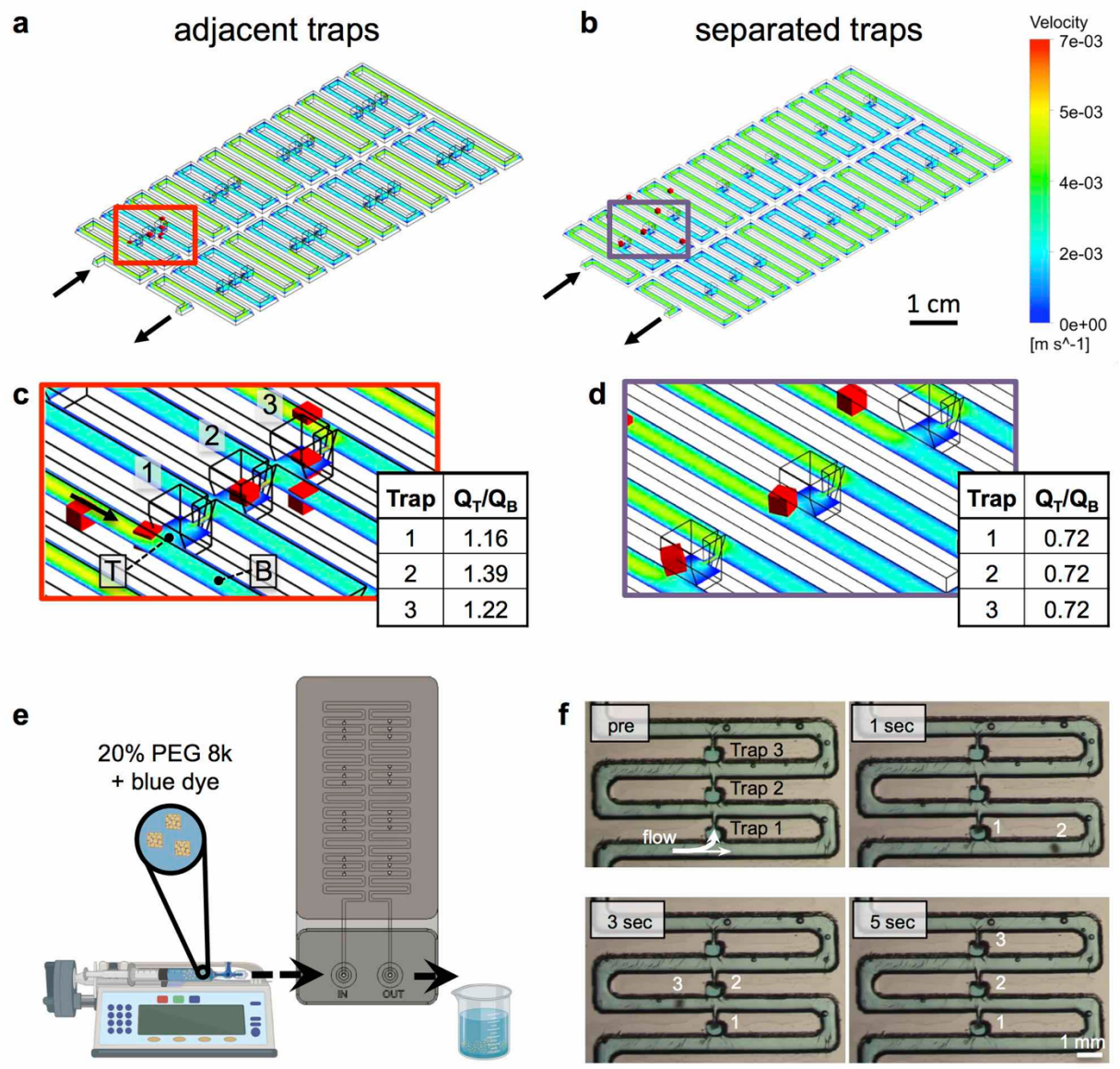

Figure 3.6 Finite volume modeling and cuboid loading into the microfluidic device

(a,b) 3D schematics of the microfluidic device with adjacent traps **(a)** and version with separated traps **(b)**, showing a 2D cross-section of the 3D velocity profile performed with Ansys Fluent (point particles in red). First well (three traps) outlined with a box. (c,d) Closeup views of the first well region with locations at which flow was measured in a plane perpendicular to flow indicated for the trap (T) and the bypass channel (B). Flow (Q) ratios given for each trap. **(e)** Experimental setup. **(g)** Still images of device loading with fixed U87 cuboids (labeled 1,2,3) in a 20% PEG solution with blue dye. Flow rate of 20 mL/h.

We next experimentally evaluated the loading efficiency of cuboids into the trap under relatively controlled conditions. For these experiments (setup in **Fig. 3.6e**), we used sparse, fixed U87 glioma cuboids manually selected for similar size (~300-500 μm). In preliminary experiments, we observed that cuboids tended to rapidly settle to the bottom of the channels, which affected the trapping efficiency and could cause clogging. We could only achieve successful trap loading with medium or PBS if we loaded manually using a syringe while applying transient bursts of pressure. In contrast, manual loading with a collagen solution worked relatively smoothly without clogging. However, syringe pump loading with collagen proved impractical due to its high cost (limiting the volume we could use) and its irreversible gelation (a threat during extended loading if the solution is not kept cold in the whole fluid path, including the syringe, tubing, and device). Therefore, we suspended the cuboids in a 20% PEG solution (lightly colored with blue dye), which was dense enough to slow the settling of cuboids at rest. For these experiments, we controlled the flow rate (20 mL/h) with a syringe pump. We found that cuboids would indeed fill the traps (**Fig. 3.6d**), but with less than 100% efficiency and with occasional sticking (that could be overcome by a brief, abrupt change in flow rate). Therefore, to quantitate trapping efficiency, for each of the two devices, we evaluated the filling of the first trap while all other traps were empty (to minimize any confounding effects on resistance). Cuboid removal by manual flow in reverse permitted us to perform multiple trials on the same trap. We found that the trapping efficiency was 84% (26/31) for device 1, and 69% (22/32) for device 2. Interestingly, for the cuboids not trapped by the first well, the trapping efficiency was 100% at the second well (5/5 for device 1 and 10/10 for device 2), consistent with the prediction by finite volume modeling that trap 2 would have a higher efficiency than trap 1.

When we performed manual loading of live cuboids in collagen (as in **Fig. 3.6e**), cuboids filled 83 ± 4% of the 24 traps of each of 4 different devices (AVE ± S.E.M.). Cuboids were at a low concentration to minimize interference between them, with excess cuboids to maximize filling (~300 cuboids in 1.5 mL, not accounting for loss from manipulation). All but one of the unfilled traps (17%) were blocked by air bubbles present during loading. Furthermore, air bubbles nucleate and grow in the collagen solution (initially at 4ºC) because as it warms up, dissolved gases lose their solubility. These problems could potentially be mitigated by improvements in fluid handling or by addition of a bubble trap element. Despite filtering, one empty trap was plugged by a tissue piece too large to pass through the trap channels and too small to be in the target size range. Of the traps filled with cuboids, (17 ± 3%) were filled by more than one cuboid. These touching cuboids fused over time in culture and were thus considered as one cuboid for later analysis. Removal of the silicone layer did not disturb the cuboids, which were held in place by collagen gel. In these preliminary experiments, our goal was to demonstrate the successful loading of a multi-trap device. This loading procedure was arguably wasteful, but we envision that in the future, one could recycle most of the untrapped cuboids and load multiple devices with the result of one micro-dissection.

We designed our microfluidic trapping device and loading procedure to preserve as much precious tissue material as possible. One can compare our microfluidic traps (with 3 traps per well) to a straightforward alternative, random seeding into multi-well plates. In principle, the microfluidic design would trap every cuboid, though variability can arise from occasional multiple cuboids caught in a trap or from bubbles blocking traps (as discussed above). Using a Poisson distribution with an expected rate of occurrences of 3 cuboids, we estimate that random seeding into multi-well plates should yield 22% of wells with 3 cuboids, 42% with less than 3, and 35% with more than 3. With this first iteration of our microfluidic device, counting traps occupied by

1-2 cuboids, we observed that our microfluidic devices yielded 63% of wells with 3 traps occupied per well (calculated for 32 wells over 4 devices). Looking at total cuboids per well, 85% had 2-4 cuboids per well, and 100% had 1-4 cuboids per well, as compared to 61% and 76% predicted for random seeding; none had more than 4 total cuboids per well in all traps, and none had no cuboids per well, as compared to 18% and 5% predicted for random seeding. Thus, the microfluidic device had a 39% better yield of wells within a target range of 2-4 cuboids. Further improvements with reductions of bubbles such as bubble traps would improve the yield. Additionally, while random seeding places cuboids haphazardly throughout the well, the microfluidic traps arrange the cuboids into an array with defined positions that should facilitate improved readouts, notably of single cuboids or for imaging.

3.3.5 *Diffusion and spread*

To evaluate potential crosstalk between the device wells, we performed experiments with a fluorescent dye (fluorescein, MW = 332 g/mol). An open channel ~30 mm long (x) connects the last trap of one well to the narrow opening of the first trap of the next well. We measured the diffusion of fluorescein (1 mM) from one well in a device filled with collagen over 72 hrs (**Fig. 3.7**). To prevent the bulk flow of fluid that would confound results, we sealed all other traps' openings to other wells with silicone tape, plugged the inlet and outlet, and sealed the top of the fluorescein well with tape. From images taken at different time intervals, we measured the fluorescence intensity at different distances from the last open trap of the fluorescein well towards both sides (**Fig. 3.7b-d**). After 42 hrs, we found that at ~30 mm along the microchannel from the last trap under the fluorescein well (ending at a point halfway between the small and large openings of the closest trap of the neighboring well), the fluorescence reached approximately 10% of the

initial value. Beyond the first neighboring trap, the levels were much lower, with no apparent increase in fluorescence.

Next, we applied Fick's second law of diffusion to calculate for our experiments the effective diffusivity of fluorescein in collagen-filled microchannels:

$$\frac{\partial C}{\partial t} = D\frac{\partial^2 C}{\partial x^2}$$

A solution to Fick's second law of diffusion in semi-infinite media and a constant concentration source is given by:

$$C(x,t) = \frac{C_x - C_0}{C_s - C_0} = 1 - \mathrm{erf}\left(\frac{x}{2\sqrt{Dt}}\right) = erfc\left(\frac{x}{2\sqrt{Dt}}\right)$$

where D represents the effective diffusivity of fluorescein in collagen, $C(x=0) = C_s$ is the concentration of fluorescein at the source, and $C\ (x = \infty) = C_0$ corresponds to the concentration at the first trap of the next well. We assume that C_s remains constant over time, and $C_0 = 0$. The characteristic diffusion length (L) at a given time (t) is defined as the distance at which the concentration of the diffusing species reaches 50 % of the source concentration (C_s) and can be approximated by $L \approx \sqrt{Dt}$. With a similar rationale, the solution for D can be approximated using 15% of the source concentration instead, with $L \approx 2.04\sqrt{Dt}$. Using this relationship, we used a quadratic fit to estimate the effective diffusivity of fluorescein at $C\ (x,t) = 0.15$ using the experimental $\partial C/\partial t$ curves for different locations (10 and 12.5 mm away from the source) over the first 16 hours (**Fig. 3.7c**). This calculation yielded an effective diffusivity of fluorescein in collagen for our system of 6.04 x 10^{-10} m^2/s, close to the reported diffusion constant of fluorescein (D = 4.25 x 10^{-10} m^2/s)[183]. However, at longer time points (> 16 hours), the fluorescein movement appeared to be approximately 4-fold faster. Thus, we suspect there must be an alternative transport mechanism, such as residual flow caused by hydrostatic pressure or evaporation (the sealing of

outlet and the open well was incomplete), that disrupted the assumption of a stationary medium in Fick's laws of diffusion. In future devices, we could ensure a stationary medium at any given point in time with physical barriers such as valves.

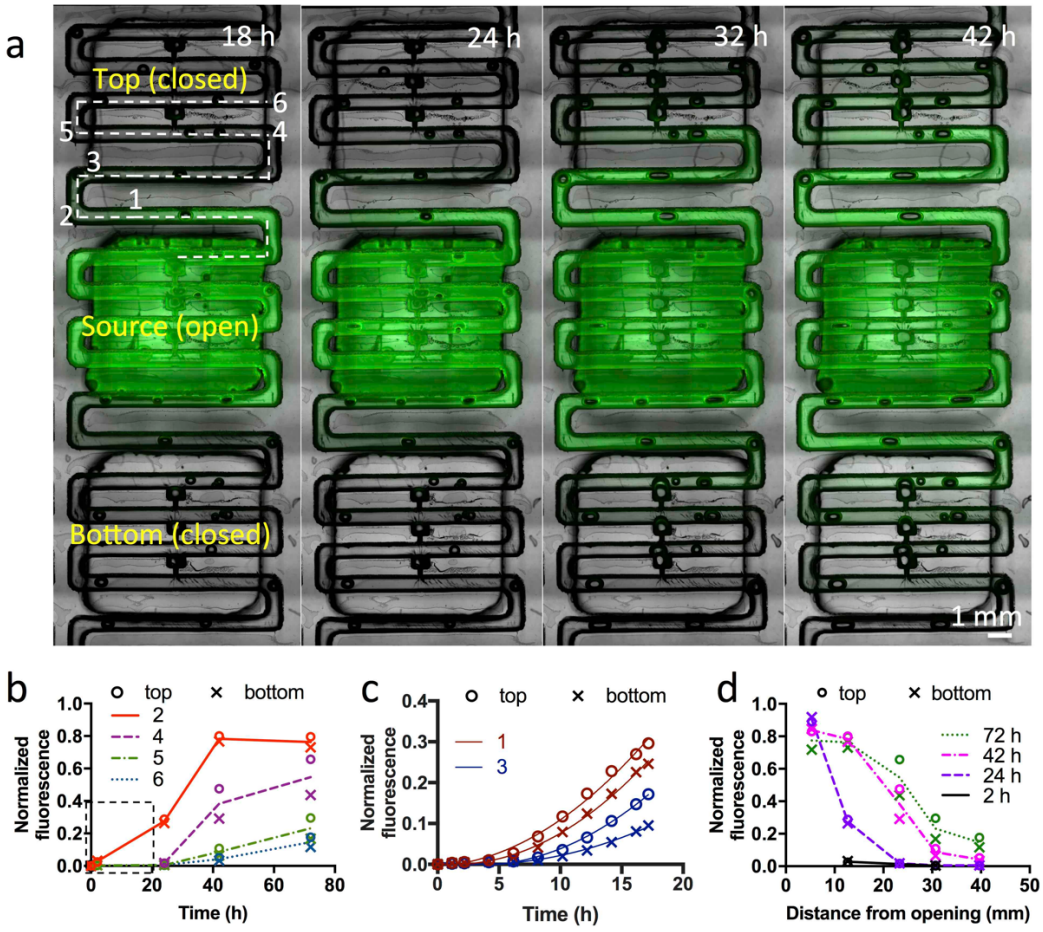

Figure 3.7 Diffusion and spread analysis

(a) Overlay of fluorescent and brightfield images of a collagen-filled device loaded with fluorescein (green) dye in a source well. Only traps in that well are open; the rest are sealed. At different times, fluorescent measurements were taken at different distances in both the "top" and the "bottom" directions, as indicated by the numbers along the dotted line. **(b)** Graph of fluorescence versus time, measured at different locations (numbers in **(a)**). Line represents the average value of the top and bottom directions. (c) Graph of fluorescence over the first 16 h (boxed area in **(b)**) as measured in two locations as indicated in **(a)**. A quadratic fit is shown. **(d)** Graph of fluorescence versus distance along the dotted line in **(a)**, measured at different times. Line represents the average value in the

top and bottom directions. After background subtraction, fluorescence was normalized to maximal fluorescence, as measured in the channels between the traps of the source well.

3.3.6 *Device operation and fluorescent dye delivery using collagen loaded glioma cuboids*

We performed experiments to demonstrate the culture of cuboids and selective dye application in the device (**Fig. 3.8**). For these experiments, we manually loaded U87 glioma cuboids in collagen gel immediately after cutting. After gelation, we labeled live cells in the cuboids for one hour with alternating patterns of green and red live fluorescent dyes (CellTracker Green and CellTracker Orange) (**Fig. 3.8a**). Imaging after PBS washes that day (data not shown) and after two days (**Fig. 3.8c**) show robust labeling of both dyes, indicating continued viability of the cuboids and no evidence for crosstalk between wells. To further confirm the cuboids' viability on day 2, we additionally stained the CellTracker Orange-labeled wells with the cell death nuclear marker, SYTOX green, and the pan-nuclear marker, Hoechst, while Hoechst alone was added to the CellTracker Green wells. As shown in Figure 3.8 d-f, SG staining revealed minimal cell death. If desired, confocal imaging or similar (combined with tissue clearing) could give a cellular level analysis of viability.

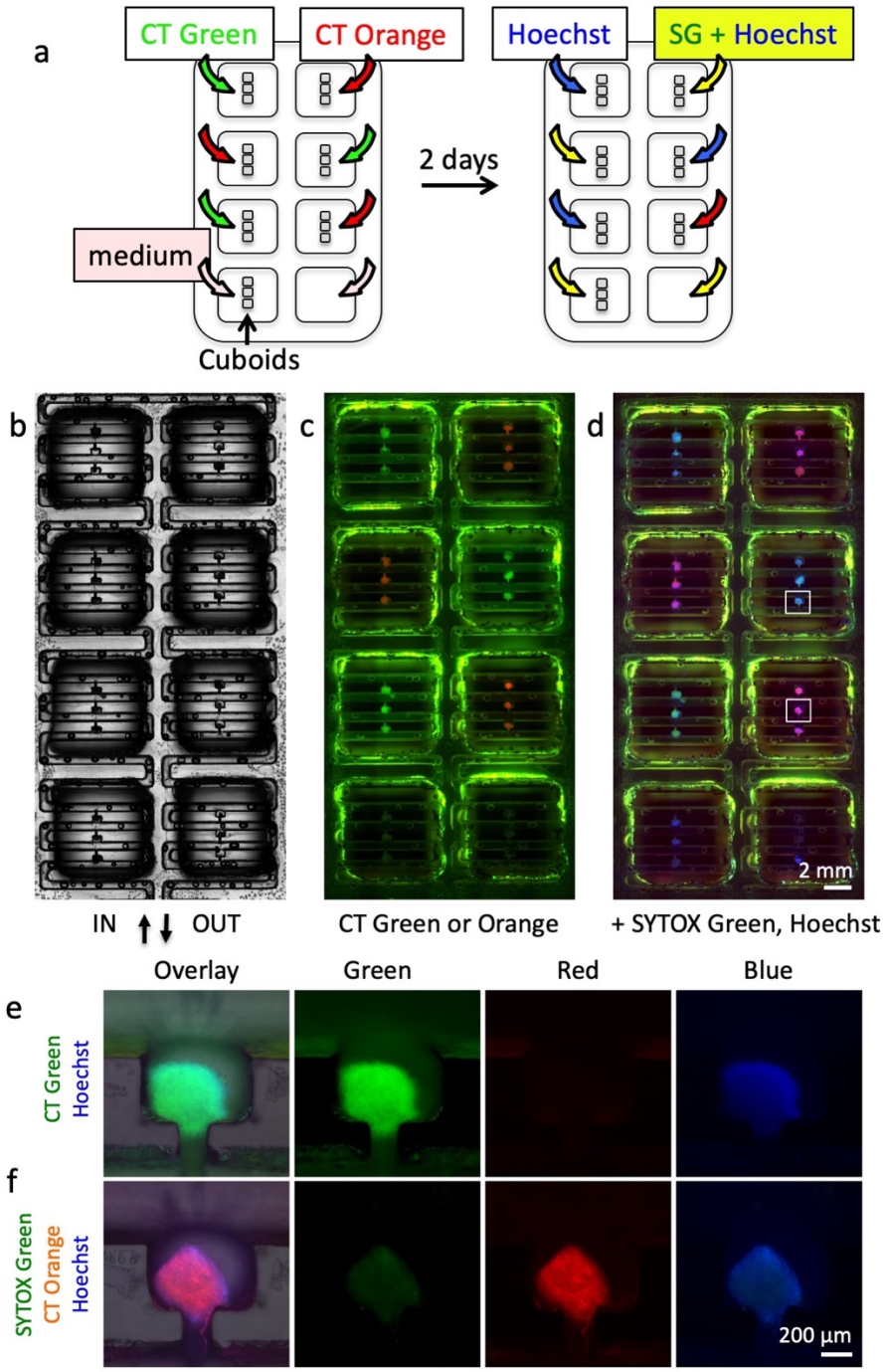

Figure 3.8 Device operation and on-device fluoresce labeling of glioma cuboids

(a) Schematic of the procedure. After loading of live U87 cuboids in collagen into the device and application of wells, cuboids were labeled with fluorescent CellTracker (CT) dyes (one hour in culture medium) in the pattern indicated for two devices in parallel with similar results. The bottom well was only exposed to medium. These dyes label live cells. After two days in culture, the cuboids were imaged, then exposed to the pan-nuclear blue dye

Hoechst. Wells with CellTracker Red were additionally exposed to the nuclear cell death indicator SYTOX Green (SG). **(b)** Brightfield image indicates the direction of cuboid loading. c) CellTracker fluorescence after two days indicates continued cell viability. **(d)** Additional cell death staining with SG and Hoechst was performed. e) Closeup of CT Green-labeled cuboid in **(d)**. **(f)** Closeup of CT Orange-labeled cuboid in **(d)**, also showing minimal cell death by SG staining

3.3.7 *Drug delivery*

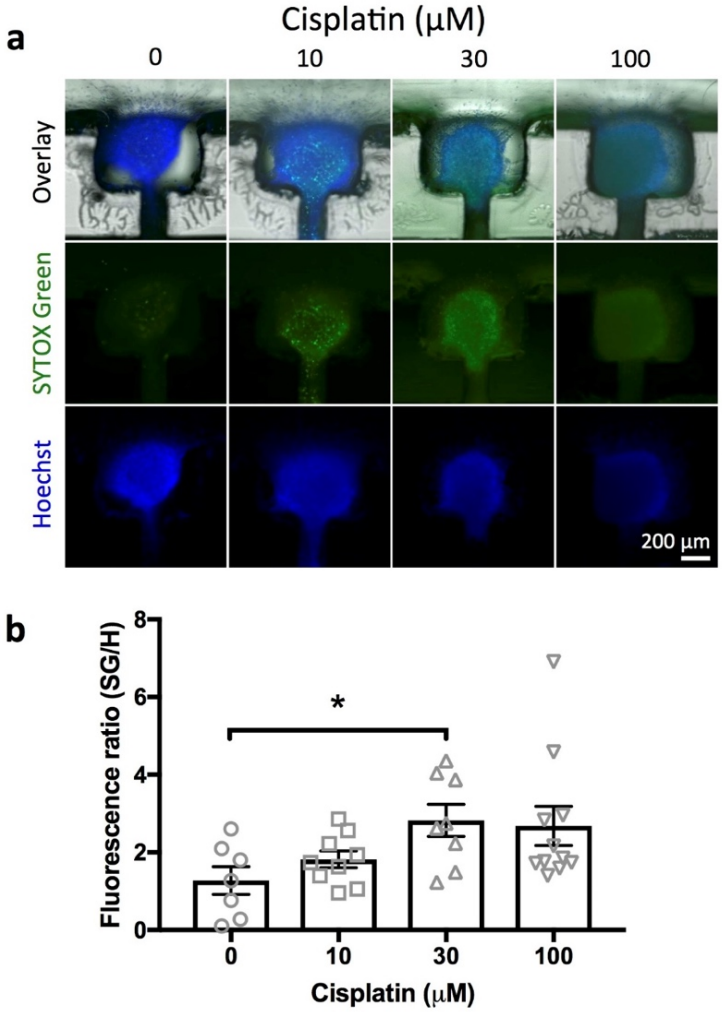

Figure 3.9 Preliminary drug delivery of CP to intact glioma cuboids

Drug treatment with the device**.** a) Cell death in U87 cuboids after treatment for two days with different concentrations of Cisplatin. Representative images from two devices with two wells each per concentration. SYTOX Green (green nuclear death stain) and Hoechst (blue pan-nuclear stain). b) Quantitation of cell death by

mean fluorescence ratio of SYTOX Green (death) to Hoechst (all), after each normalized to mean fluorescence in control conditions. Individual points and ave ± s.e.m. N=7-11. Student t-test * $p < 0.05$.

As a first test of drug treatment with the device, we exposed U87 cuboids in the device with different concentrations of a cytotoxic chemotherapy drug, cisplatin (**Fig. 3.9**). In each of two devices, we treated two wells with each concentration of cisplatin (0, 10, 30, 100 μM) for 2 days from day 1 to day 3 (**Fig. 3.9a**). As a straightforward, simple measure of cell viability, we measured the mean fluorescence ratio in epifluorescence images of SG dead nuclear fluorescence to Hoechst pan-nuclear fluorescence (**Fig. 3.9b**). We found a statistically significant response to 30 μM cisplatin, with 100 μM showing a trend. The weak SG staining at higher concentrations was accompanied by concomitant weak Hoechst staining, consistent with breakdown of nuclei in later stages of cell death. Note the variability in responses, not unexpected due to the small size of the cuboids as well as some of the baseline viability noted without drug treatment (~15% as seen in **Fig. 3.3i, Suppl. Fig. 3.2**). Off-device experiments performed in parallel with 100 μM cisplatin also showed cell death (**Suppl. Fig. 3.2**). We did not exclude any statistical outliers here. However, future experiments could increase the sensitivity of the assay by incorporating pre-treatment viability tests to exclude from analysis the already less viable cuboids without treatment. These results were similar to our previous experiments with U87 glioma slices on and off a microfluidic device that showed cell death in response to 30 and 100 μM cisplatin by SG/H live viability staining.[31] These high cisplatin concentrations reflect the known sensitivity of the U87 cell line and are at least 10 fold higher than clinical doses in patients.[184] While confocal imaging could provide a more precise evaluation, it is more time consuming. This device platform is also compatible with analysis of the supernatant in the wells for cell death, e.g., LDH levels by fluorescent assay, but would require more manipulation and would lose the independence of measurements for individual cuboids. Lastly, tumor heterogeneity poses a challenge to drug testing

because different parts of the tumor respond differently to drugs. By histological measures on their μDT microfluidic platform, Simeone et al. determined that 15 PDX μDTs could encompass the heterogeneity of the original tumor.[153] Their methodology could help inform the minimum number of cuboids and wells required in upscaling our device to a high-throughput multi-well platform.

3.4 CONCLUSIONS

This chapter demonstrates a unique method to develop and culture intact cuboidal microtissues ("cuboids") along with a microfluidic platform that miniaturizes functional drug testing. With this set of studies, we understood the fundamental properties of both the cuboid microdissection process and the functionality of the microfluidic device. The gathered results will allow us to further optimize the size homogeneity of microdissected cuboids and the device's trapping efficiency. Future work for this project will be focused on a thorough investigation of the fluid dynamics of the trapping system with computational fluid dynamics. The design and fabrication method makes the microfluidic device scalable to a 96-well plate (or larger) format, opening the possibility for large-scale functional testing with human donor tissue in the near future.

3.5 EXPERIMENTAL

3.5.1 *Cell culture and drug screening*

U-87 MG (U87) cells (ATCC) were grown in DMEM/F12 (Invitrogen) supplemented with 10% fetal bovine serum (VWR) and penicillin/streptomycin (Invitrogen). We passaged the cells twice a week.

3.5.2 *Xenograft mouse model*

Mice were handled in accordance with protocols approved by the University of Washington Animal Care and Use Committee. To generate xenograft tumor mice, male athymic nude mice (Taconic, Foxn1^{nu}) aged 4-10 weeks were injected subcutaneously in the flank (0.5-1 million cells in 200 µL of DMEM-F12 serum and antibiotic-free medium). Mice were sacrificed before tumor volume reached 2 cm^2 (2-4 weeks). Livers from male nude mice without tumors (2-4 months old) were used for the intact cuboid imaging. For the chopping quantitation experiments, we used livers from adult (3 months old) C57BL6-derived mice (C57BL6-*Sntb1*$^{tm2fl/fl\ SCF}$, functionally wild-type) were kindly provided by M. Adams and S. Froehner, University of Washington.

3.5.3 *Micro-dissection procedure and cuboid culture*

To microdissect tissue cuboids, we used a standard McIlwain tissue chopper (Ted Pella, Inc.) set to 400 µm slice thickness. We first cut 400 µm-thick slices by mounting ~1 cm × 1 cm tissue samples (mouse liver or glioma) onto a ¼" PMMA disc using cyanoacrylate glue (Krazy glue). This procedure resulted in ~20-25 tissue slices, which we manually separate as needed. Then, we manually transferred the slices into ice-cold solution in a dish using a razor blade. When possible, we kept the live tissue in ice-cold solutions, with mouse liver and slices in Belzer UW Cold Storage Solution (Bridge to Life), and with glioma tissue in DMEM/F12 supplemented with HEPES. Note that the blade leaves indentations in the PMMA surface with each cut. After leveling the blade again to ensure maximum contact, we cut the slices into cuboids as follows. We placed 400 µm-thick slices onto a relatively smooth (unused or used only once prior) ¼" PMMA disc and removed excess fluid to prevent movement. After the first series of cuts, we rotated the disc 90° and repeated the cutting procedure. After cutting, we transferred the cuboids to a dish. To separate

the cuboids, we gently pipetted up and down and used other tools if necessary (i.e., dissecting scissors). Then, we filtered the cuboid solution through a 750 μm filter followed by a 300 μm filter (Pluriselect, USA), keeping the cuboids retained by the smaller filter. Cuboids were maintained and washed with DMEM-F12 with HEPES. Before loading into devices, we manually removed unwanted particles (i.e., excess glue, unwanted pieces). For experiments with liver cuboids for intact imaging, we did the first cut of the liver into 400 μm-thick slices using a 5100mz vibratome (Lafayette Instrument) in ice-cold Krebs-Heneseleit solution (Alfa Aesar), bubbled with carbogen (95% O_2, 5% CO_2).

U87 cuboids were cultured in collagen hydrogel. We prepared 80% collagen (Corning rat tail collagen type 1, 354236, 3-4 mg/mL), 10 % 10x PBS, and 10% serum-free medium. We then used filtered-sterilized 1M NaOH to neutralize the pH to ~7.2. For culture in 6 well plates, cuboids were cultured in 1 mL collagen on top of a 0.4 μm filter Transwell PFTE membrane insert (PICMORG50, Millipore) with 1.3 mL culture medium placed below. Cuboids were cultured both with and without an additional layer of pre-gelled 1 mL collagen below with similar histology and staining observed, apart from a relatively flatter shape often seen without the extra collagen layer. The culture medium contained Neurobasal-A medium (Invitrogen) with 25% heat-inactivated horse serum (Sigma), Glutamax (Invitrogen), 2× penicillin/streptomycin (Invitrogen), and growth factors (EGF 20 ng/mL and FGF 20 ng/mL, Preprotech or Invitrogen). Cisplatin (3 mM stock in dH20, MedChem Express) was diluted in cell culture medium for the drug treatment experiment.

3.5.4 *Cuboid size analyses*

During microdissection, each set of slices cut at once (400 μm-thick, 11-17 slices, ~100 mm^2) represented one set of cuboids. After dissecting each set of slices (as described above), we

isolated the resulting cuboids in a 6-well plate. We took tiled 2x images of each set of cuboids before and after filtering.

We utilized the free Fiji[149] image analysis program to investigate cuboid size distribution and sample yield for both mouse liver and intact glioma tissues. First, we converted each image to an 8-bit binary format. After binary conversion, we did background subtraction (100-200 pixel rolling ball radius) and manually adjusted brightness and contrast, if necessary. In addition to background subtraction, bubbles and other imperfections (such as objects out of focus) were eliminated from the images utilizing a background-colored brush. After cleaning, we adjusted the threshold to isolate the tissues (cuboids and slices, black) from the background (white, **Suppl. Fig. 1**a).

We converted binary images to masks to isolate cuboid aggregations and performed a watershed (1px line width). Each image was carefully inspected to ensure proper watershed. By comparing it to the original image, we distinguished areas of imperfections and did manual corrections as necessary. We adjusted the scale (μm/px) of each image and analyzed the area (μm^2) of cuboids/slices, by setting a size range of $(100\ \mu m)^2 – (650\ \mu m)^2$ and $> (300\ \mu m)^2$, respectively.

To estimate each cuboid's dimensions, we assumed that cuboids had a cuboidal shape and took the square root of the obtained area value. We utilized GraphPad Prism 8 to investigate each cuboid set's size distribution (relative frequency) using a 100 – 650 μm bin range with a 50 μm bin width. Similarly, we utilized a 100 – 750 μm bin range for cumulative size range distribution analyses with a 300 μm bin width and averaged the relative frequency for all data sets (n=6, for both mouse liver and glioma).

To estimate the % of the original sample left after dissection and filtering (**Suppl. Fig. 1**b&c), we computed the total area of each slice set. Then, we aggregated the total cuboid tissue

area for each set before and after the filtering step and the total area of cuboids within the range of 300 – 600 μm. Finally, we divided each data set by the total slice area. The same process was performed for both mouse liver and glioma tissues.

3.5.5 *Live staining and microscopy*

Live cuboids were stained for 1 hour, 37°C, with the following dyes (individually or in combination) diluted in culture medium: Cell Tracker Green CMFDA (Invitrogen, 10 μM), Cell Tracker Orange CMRA (Invitrogen, 10 μM), Hoechst (H; Invitrogen, 16 μM), and SYTOX Green (SG; Invitrogen, 0.01 μM). We performed epifluorescence and brightfield microscopy of the cuboids with a Nikon Eclipse Ti inverted microscope (Nikon Instruments, Melville, NY) at 2x and 4x. For SG analysis, we used FIJI as follows. We performed background subtraction from empty areas. Cuboid regions were created from the Hoechst channels by thresholding the watershed on a binary image, followed by Analyze Particles. Mean SG fluorescence was normalized to the average value of untreated cuboids.

3.5.6 *Immunostaining*

After imaging, off-device cuboids were fixed with 4% paraformaldehyde overnight then cryoprotected with 30% sucrose/PBS overnight two times. Cryosections (14 μm thickness) were then processed for H&E or immunostaining. For immunostaining, we pretreated tissue sections with 0.6% hydrogen peroxide in methanol for 30 min, washed, and then for some antibodies (processed for antigen retrieval (by steaming for 30 min in 10 mM sodium citrate, 0.05% Tween 20 (Sigma), pH 6.0. After at least 30-min incubation in blocking solution (Tris-NaCl-blocking buffer or TNB buffer, Perkin Elmer, with 0.1% Triton X-100), we incubated the tissues with primary rabbit antibodies (diluted in TNB) overnight at 4°C: active cleaved caspase 3 (CC3, 1/600,

Cell Signaling), Ki-67 (1/1,000, AbCAM, ab15580), CD31 (1/200, AbCAM ab28364), or CD45 (1/1,000, AbCAM, ab10558). Finally, we incubated the tissues with peroxidase polymers of the appropriate species for 30 min (rabbit from Vector Labs MP7401 or mouse from Biocare MM510) then with the chromogen 3,3'-Diaminobenzidine (DAB, Vector Labs) and lightly counterstained with hematoxylin. We performed all tissue washes with PBS.

3.5.7 *Clearing and staining for light-sheet microscopy*

Liver cuboids embedded in collagen were stored in a 30% sucrose solution before staining and clearing. Cuboids were first dehydrated in graded steps to a 70% ethanol solution (v/v in water). Samples were then stained with a fluorescent H&E analog consisting of a 1:500 dilution of TO-PRO3 Iodide (Cat: T3605, Thermo-Fisher) and 1:4000 dilution of Eosin-Y (Cat: 3801615, Leica Biosystems)[169]. Following staining, samples were fully dehydrated in 100% ethanol and then cleared and stored in ethyl cinnamate at room temperature before and after imaging (Cat: 112372, Sigma-Aldrich)[170].

3.5.8 *Open-top light-sheet microscopy imaging*

Collagen-Collagen-embedded liver cuboids were imaged on a multi-resolution OTLS microscope[168,169]. Embedded cuboids cleared in ethyl cinnamate were mounted intact on a flat sample holder (Ultem 1000), mounted onto a motorized XYZ stage, and immersed in an ethyl cinnamate-based immersion bath. Specimens were illuminated at a 45-degree angle with a Gaussian light sheet (NA = 0.09, 2.75-µm FWHM light-sheet thickness) at 488 nm and 660 nm to excite eosin and TO-PRO3, respectively. The specimen was translated through the light sheet such that a series of adjacent 2D "optical sections" were imaged to generate a 3D dataset (0.65-µm lateral resolution). The fluorescence signal was imaged through a band-pass filter onto an sCMOS

camera (ORCA Flash 4.0). A volume of approximately 0.10 mm^3 was imaged for each cuboid at an approximate volumetric imaging rate of 0.07 mm^3/min (for a 2-channel dataset). Raw images were de-skewed by 45 degrees and subsequently stored in a Hierarchical Data Format (HDF5) with a B3D compression filter, as has been previously described[169,185]. BigStitcher was utilized to fuse these datasets, which were then visualized volumetrically in Imaris[186]. Additionally, to visualize datasets in a palette that mimics H&E histology, a false-coloring algorithm (based on Beer-Lambert Law absorption) was applied using a Python script[187,188]. The TIFF images of cleared cuboids obtained from OTLS microscopy were imported to Imaris software (Imaris 9.5.0, Bitplane AG) to perform the 3D reconstruction. Imaris analysis was done using three channels: the original TO-PRO3 (nuclei), the original eosin (for surface volume), and a binary version of the eosin channel representing the voids (vasculature). For the analysis using the cuboid's central region (vasculature and nuclei), we cropped the images to remove the outer regions with signs of unhealthy tissue (condensed nuclei and pale eosin staining). For nuclear analysis, nuclei labeled with TO-PRO3 were reconstructed into 3D surfaces using the 'surpass module' and "surface creation" feature, including steps of region-of-interest (ROI) selection, background subtraction, thresholding, and water-shedding. The diameter for each nucleus was measured for the three sides of the bounding cube, and the shortest length was used to segregate nuclei according to their size distribution. We removed from analysis the nuclei on the edges (inaccurate size as cut by the border) and the few "nuclei" that were too large (>15 μm) or too small (<1 μm with volume < 5 μm^3) to be nuclei. For the vasculature analysis, with FIJI, we converted the eosin images from 32 bit-TIFF to 8-bit, used Auto-local-threshold to isolate the vasculature, including gaps between the cell and sinusoids, and saved as a binary image (inverted). After importing to Imaris with the other two channels, we used the 'surface creation' feature to construct a 3D cuboid vasculature.

Thresholding was performed on each cuboid individually to optimize the capture of the nuclear and vascular features. *(*This work was done by Ph.D. students Lindsey Barner and Kevin Bishop from Prof. Jonathan Liu's lab Gargi Mishra in Dr. Taranjit Gujra's lab*).*

3.5.9 *CO_2 laser micromachining*

The current version of our microfluidic consists of an 8-well plate with an integrated channel network layer. We fabricated the device by laser micromachining of PMMA substrates, thermal fusion, and adhesive bonding. The device is composed of four layers: a 1,000 µm-thick PMMA channel network layer (Astra Products, Baldwin, NY (11510103)) containing the trapping microchannel connected in series to 8 sets with 3 traps/set, a 200 µm-thick PMMA sealing layer (AFT00, SPolytech, Chungbuk, Korea), a 76 µm-thick removable polysil double-coated silicone adhesive tape (S1001-1DC1, Adhesive Applications, Easthampton, MA), and an insertable 6.35 mm-thick PMMA bottomless 8-well "well plate" (1227T569, McMaster-Carr, Elmhurst, IL) lined with a 50 µm-thick 3M™ High-Strength Acrylic Adhesive 300LSE. In addition to the main components, the device also has a customized base and a lid (1227T569, McMaster-Carr, Elmhurst, IL). The base raises the device from the surface to avoid scratches (thus maintaining optical clarity) and makes its dimensions compatible with conventional imaging slide stages. The lid prevents contamination and allows proper airflow for tissue culture.

The CO_2 laser system used (VLS3.60, Scottsdale, USA) has a wavelength of 10.6 µm and a maximum power of 30 W. We utilized AutoCAD 2017 for device design (**Suppl. Fig. 3**) and optimized the power and speed settings of the CO_2 laser to achieve specific widths and depths for the microchannels and to cut the outlines of the channel network and sealing layers. We manually lined the bottomless well-plate with the high-strength acrylic 300LSE adhesive before laser cutting for optimal alignment.

3.5.10 *Post ablation processing*

Laser ablation of PMMA includes both polymer debris and reflow. To remove debris from the laser-cut substrates, we rinsed each of the device components with DI water and sonicated them in an IPA bath for 30 sec. To reduce surface roughness and improve the optical quality, we exposed the channel network to chloroform vapor. We used a glass container (264 mm (L) × 213 mm (W) × 165 (T) mm) filled with 50 mL of chloroform and steel standoffs (6 mm) to elevate the laser-micromachined layers 3 mm above the chloroform surface (**Suppl. Fig. 2**). We concurrently exposed the channel network layer and the sealing layer to chloroform for 5 min.

3.5.11 *Solvent and adhesive bonding*

We performed a combination of thermal bonding, solvent bonding (which we refer to as "thermal solvent bonding"), and adhesive bonding Exposure to chloroform vapor also causes the PMMA to become slightly adhesive by inducing polymer reflow.[75,146] After chloroform vapor treatment, the surface of the PMMA substrates becomes soft due to polymer solvation. When two treated surfaces are placed in contact, a cohesive molecular bond is formed while excess vapor evaporates from the interface. For assembly, we exposed the channel network layer and the sealing layer to chloroform vapor. For "thermal solvent bonding," we first hand-pressed the sealing layer onto the channel network layer to form a weak bond. Then, to ensure uniform bonding, we sandwiched the two layers between two ~3 mm thick PDMS slabs with the same outer dimensions as the channel network layer. Finally, we placed the whole ensemble in the heat press for 4 min at 150 psi and 60˚C.

Before cuboid loading, we sealed the trap openings with the removable polysil double-coated silicone adhesive tape using the same pressing setup at room temperature. After loading,

we manually removed the silicone adhesive from the channel network. To bond the bottomless 8-well plate to the channel layer, we removed the 3M300LSE liner and manually pressed both components together.

3.5.12 *Hydrophilization and bubble removal*

After device assembly and before use, we treated each device with oxygen plasma for 5 min at ~950 mTorr (60 watts, Diener RF plasma oven) to increase the PMMA surfaces' hydrophilicity. Then, to prepare the device for use, we manually filled the device with 100% ethanol to remove bubbles from trapping areas. Once the device was bubble-free, we manually injected sterile DI water into the microchannels, followed by sterile PBS.

3.5.13 *Device operation*

The device is designed to be operated in two main stages: 1) cuboid loading with the polysil double-coated silicone adhesive tape; and 2) cuboid culture after manual removal of the silicone adhesive tape and attachment of the bottomless 8-well plate. Before loading, we ensured that the trap openings were completely bubble-free and filled the device with ethanol, then water, then PBS. Devices to be utilized for culture were sterilized with 70% ethanol and followed by sterile solutions. Cuboid loading was accomplished by manual injection or by pump infusion.

For our loading efficiency experiments, we manually suspended fixed glioma cuboids in a 5 mL syringe containing 20% 8k-PEG (P2139, Sigma-Aldrich). To load the cuboids, we connected the inlet of the device to the 5 mL syringe and used a syringe pump (Fusion 200, Chemyx Inc., Stafford, TX) at a flow rate of 20 mL/hr. For our live glioma cuboid experiments, we suspended glioma cuboids in a 5 mL syringe containing collagen. We manually loaded the cuboids after connecting the inlet of the device to the 5 mL syringe. After loading, we peeled the silicone

adhesive from the channel layer and bonded the bottomless 8-well plate using the adhesive on its bottom surface and firm manual pressure. Then we carefully added reagents to each well (usually 0.2 mL/well).

3.5.14 *Dye diffusion experiment*

We manually filled the device with collagen as above. After gelation of the collagen, we replaced the silicone adhesive tape with tape that had a window cut over only one well, keeping all other wells closed. Then we glued the wells on top and clamped the inlet and outlet shut with clips. After pipetting 200 µL of 1 mM fluorescein into the one well with exposed traps, we covered the well with clear tape to prevent evaporation. We left the device on the microscope at room temperature and took tiled 2x brightfield and fluorescent images at different intervals over three days. We subtracted the fluorescence background over similar regions not exposed to fluorescein from the mean fluorescence measured at intervals along the diffusion path.

3.6 SUPPLEMENTARY INFORMATION

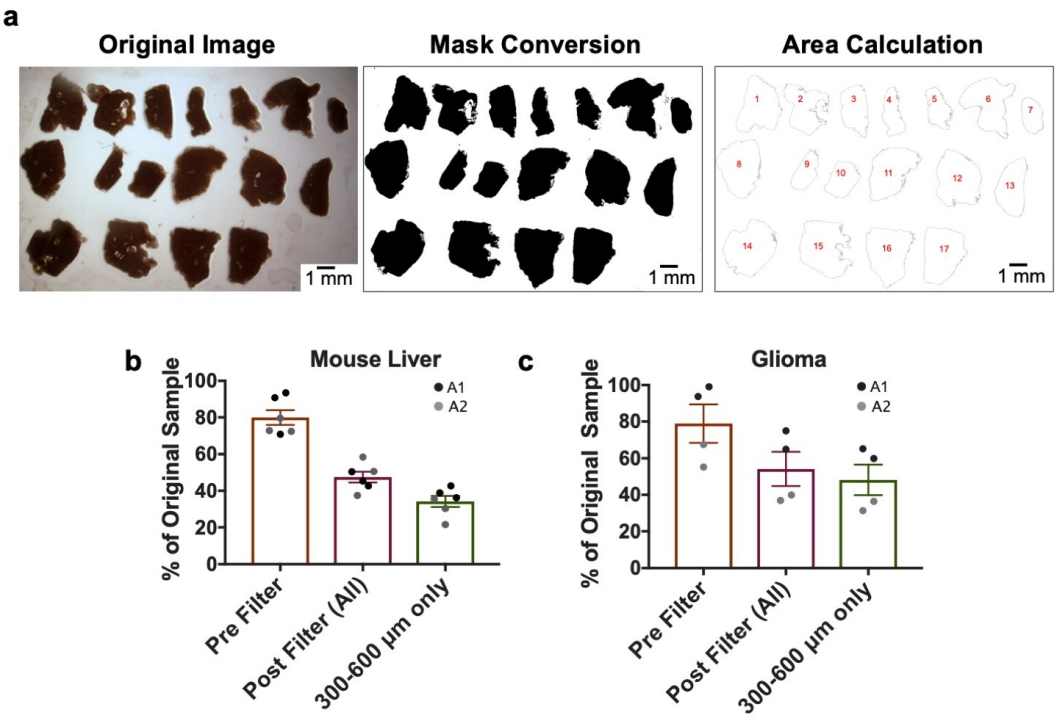

Suppl. Figure 3.1 Sample yield analysis

(a) Image processing for total area calculation of slice samples (showing mouse liver slices). The % yield from the initial sample was estimated by taking the ratio of the total cuboid area after each step of the cuboid dissection process. Graphs show mouse liver **(b)** and glioma **(c)** cuboid sample yield pre-and post-filtering and the total area of cuboids between 300-600 µm.

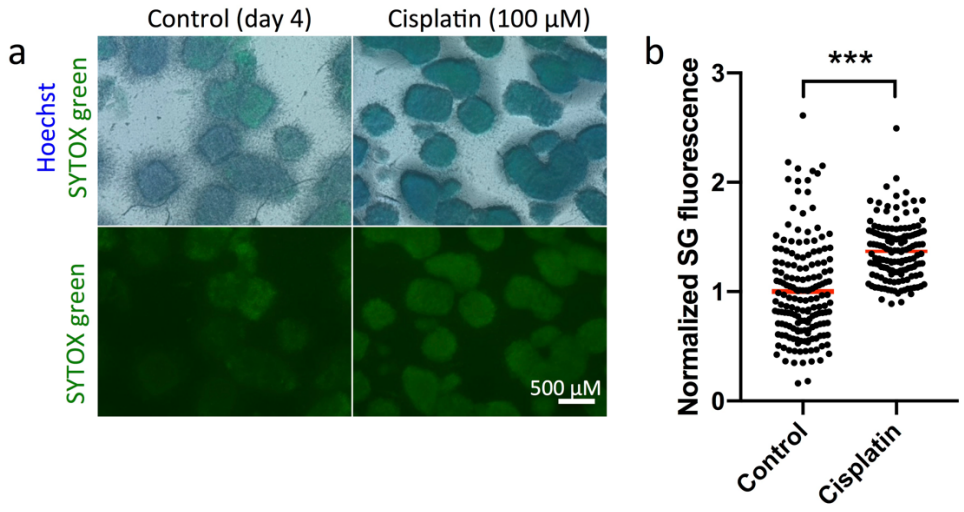

Suppl. Figure 3.2 Cuboid drug treatment off-device

(a) Cuboids (no size filtering) after treatment with Cisplatin for 48 hours from day 2 to day 4 in culture. SYTOX green (SG) green nuclear stain and Hoechst blue nuclear stain overlayed on brightfield, or SG alone. **(b)** Graph of mean SG fluorescence normalized to average fluorescence of controls. Control (N=169) and cisplatin (N=145). Individual points and average. Student's t-test with Welch's correction. ***P<0.001 (** *Gargi Mishra did this analysis in the Folch lab***)

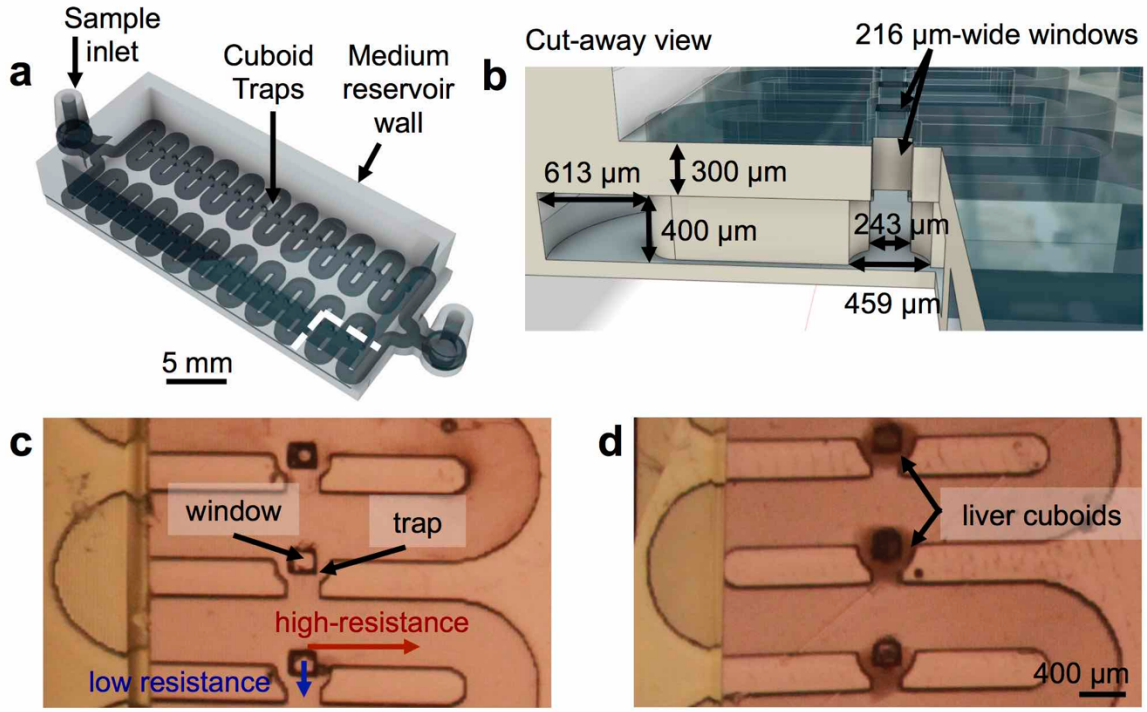

Suppl. Figure 3.3 3D-Printed cuboid device

(a) Oblique projection of the device rendered in Fusion 360. The initial straight channel bifurcates into two serpentine channels with cuboid traps, combining into a single outflow channel. Walls create a medium reservoir. (b) Cut-away closeup view, with the area, removed demarcated in (a) by a white dotted line. The puncture-to-open wells have a narrow window in the roof (not drawn). Once the cuboids are loaded, one can puncture the window with a needle to provide access to culture medium from the overlaying reservoir. (c) Top view of an empty region of the device, 3D printed using the Asiga Pico2 HD (pixels 27 µm x 27 µm, Z layer thickness 25 µm). The high and low flow resistance paths enable trapping. Once a cuboid is captured in a trap, blocking flow through the trap, the next cuboid flows along for capture in the next trap. (d) Region after trapping of 400 µm fixed liver cuboids, subsequent collagen application, and finally, placement of medium in the overlying reservoir. (**_This work was done by Allan Au-Yeung in the Folch lab_**)

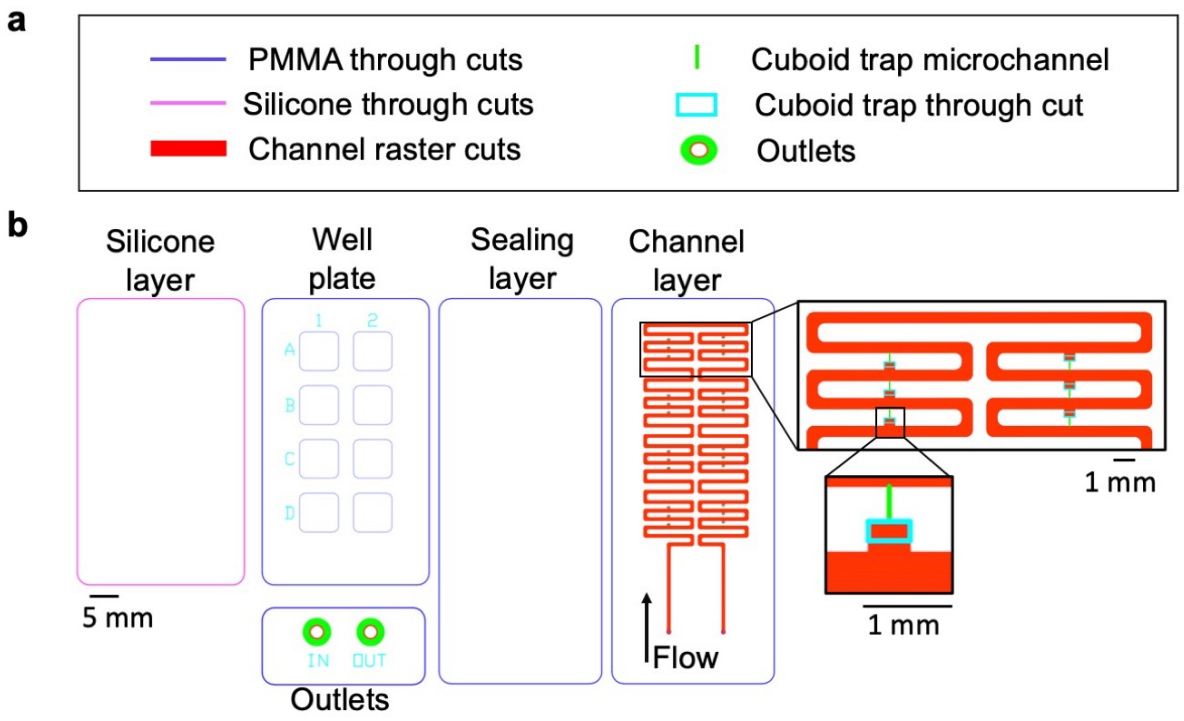

Suppl. Figure 3.4 CAD Drawings

(a) Various laser-cutting elements are used to make the microfluidic device layers**. (b)** CAD drawings showing the silicone adhesive layer, bottomless-well plate, and outlets, sealing layer, and channel layer of the device with a magnification of the trapping areas.

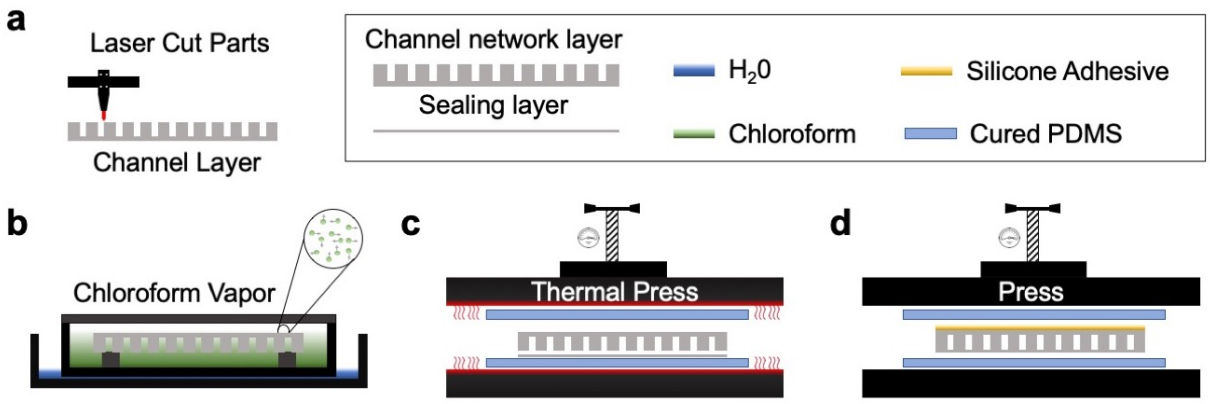

Suppl. Figure 3.5 Fabrication process overview

General overview of the device fabrication process. The overall fabrication of the device consists of **(a)** laser cutting/engraving and cleaning each of the laminates and components that compose the microfluidic device (10 min); **(b)** chloroform vapor exposure (5 min); **(c)** thermal fusion bonding (2 min); **(d)** adhesive bonding of double-sided polysil silicone adhesive (1 min); outlet installation (step not shown); and removal of silicone and insertion of bottomless 8-well plate (step not shown).

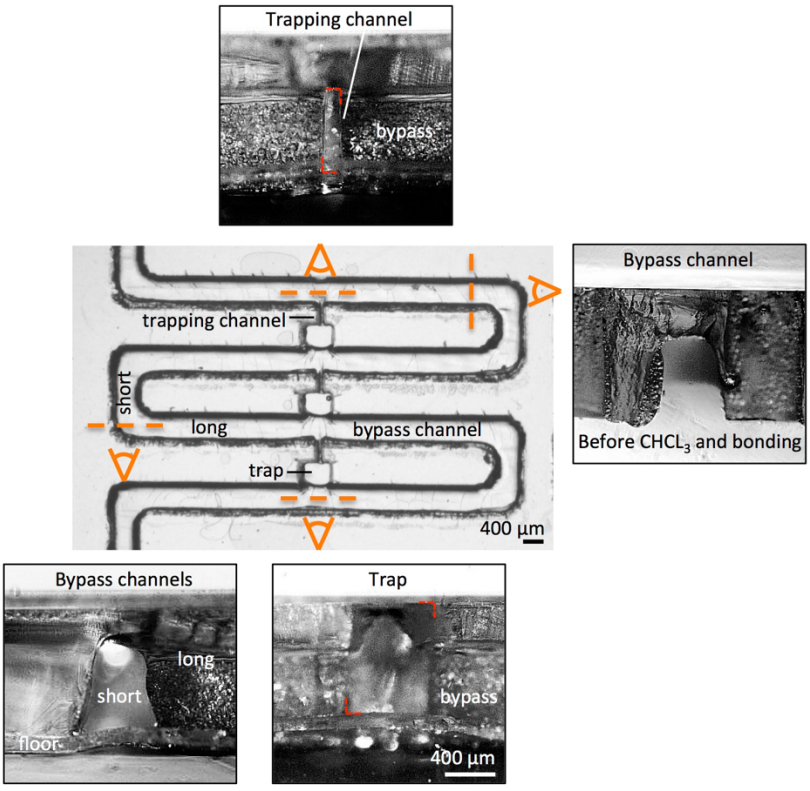

Suppl. Figure 3.6 Microfluidic device geometry

Top-view and cross-sectional views of the device after making various breaks to expose the features. Representative locations of the breaks (dotted lines) and point-of-view (eye symbol) are shown. A cross-section of the extended portion of the bypass is shown before chloroform ($CHCL_3$) treatment and bonding. Other cross-sections are shown after $CHCL_3$ treatment and bonding to the floor. Red brackets delineate feature borders for the trap channel and the trap (transition to trap channel visible inside).

BIBLIOGRAPHY

1 Herper M. The Truly Staggering Cost Of Inventing New Drugs. 2012.https://www.forbes.com/sites/matthewherper/2012/02/22/the-truly-staggering-cost-of-inventing-new-drugs-the-print-version/#325e9c7f25f8.

2 Prasad V, Mailankody S. Research and development spending to bring a single cancer drug to market and revenues after approval. *JAMA Intern Med* 2017; **10065**.

3 Siddiqui M, Rajkumar SV. The high cost of cancer drugs and what we can do about it. *Mayo Clin Proc* 2012; **87**: 935–943.

4 Harrison RK. Phase II and phase III failures: 2013–2015. *Nat Rev Drug Discov* 2016; **15**: 817–818.

5 BIO industry analysis. Clinical development success rates 2006-2015. *Bio Ind Anal Rep* 2016; : https://www.bio.org/sites/default/files/Clinical%2.

6 Shanks N, Greek R, Greek J. Are animal models predictive for humans? *Philos Ethics, Humanit Med* 2009; **4**: 1–20.

7 Provocative Questions. 2011.

8 Letai A. Functional precision cancer medicine—moving beyond pure genomics. *Nat Med* 2017; **23**: 1028–1035.

9 Letai A. Functional precision cancer medicine-moving beyond pure genomics. *Nat Med* 2017; **23**. doi:10.1038/nm.4389.

10 Hanahan D, Weinberg RA. Hallmarks of cancer: The next generation. *Cell* 2011; **144**: 646–674.

11 Junttila MR, de Sauvage FJ. Influence of tumour micro-environment heterogeneity on therapeutic response. *Nature* 2013; **501**: 346–354.

12 Sachs N, De Ligt J, Gerhardus R, Vries J, Cuppen E, Clevers Correspondence H. A Living Biobank of Breast Cancer Organoids Captures Disease Heterogeneity. *Cell* 2018; **172**: 373–386.

13 van de Wetering M, Francies HE, Francis JM, Bounova G, Iorio F, Pronk A *et al.* Prospective Derivation of a Living Organoid Biobank of Colorectal Cancer Patients. *Cell* 2015; **161**: 933–945.

14 Baker LA, Tiriac H, Clevers H, Tuveson DA. Modeling Pancreatic Cancer with Organoids. *Trends in Cancer* 2016; **2**: 176–190.

15 Boj SF, Hwang C Il, Baker LA, Chio IIC, Engle DD, Corbo V *et al.* Organoid models of human and mouse ductal pancreatic cancer. *Cell* 2015; **160**: 324–338.

16 Clevers H. Modeling Development and Disease with Organoids. *Cell* 2016; **165**: 1586–1597.

17 Gao D, Vela I, Sboner A, Iaquinta PJ, Karthaus WR, Gopalan A *et al.* Organoid cultures derived from patients with advanced prostate cancer. *Cell* 2014; **159**: 176–187.

18 Huang L, Holtzinger A, Jagan I, BeGora M, Lohse I, Ngai N *et al.* Ductal pancreatic cancer modeling and drug screening using human pluripotent stem cell– and patient-derived tumor organoids. *Nat Med* 2015; **21**: 1364–1371.

19 Nash CE, Mavria G, Baxter EW, Holliday DL, Tomlinson DC, Treanor D. Development and characterisation of a 3D multi-cellular in vitro model of normal human breast: a tool for cancer initiation studies. *Oncotarget* 2015; **6**: 13731–41.

20 Pauli C, Hopkins BD, Prandi D, Shaw R, Fedrizzi T, Sboner A *et al.* Personalized In Vitro and In Vivo Cancer Models to Guide Precision Medicine. *Cancer Discov* 2017; **7**: 462–477.

21 Astolfi M, Péant B, Lateef MA, Rousset N, Kendall-Dupont J, Carmona E *et al.* Micro-dissected tumor tissues on chip: An ex vivo method for drug testing and personalized therapy. *Lab Chip* 2016; **16**: 312–325.

22 Aref AR, Huang RY-J, Yu W, Chua K-N, Sun W, Tu T-Y *et al.* Screening therapeutic EMT blocking agents in a three-dimensional microenvironment. *Integr Biol* 2013; **5**: 381–389.

23 Jenkins RW, Aref AR, Lizotte PH, Ivanova E, Stinson S, Zhou CW *et al.* Ex vivo profiling of PD-1 blockade using organotypic tumor spheroids. *Cancer Discov* 2018; **8**: 196–215.

24 Aref AR, Campisi M, Ivanova E, Portell A, Larios D, Piel BP *et al.* 3D microfluidic ex vivo culture of organotypic tumor spheroids to model immune checkpoint blockade. *Lab Chip* 2018; **18**: 3129–3143.

25 Ootani A, Li X, Sangiorgi E, Ho QT, Ueno H, Toda S *et al.* Sustained in vitro intestinal epithelial culture within a Wnt-dependent stem cell niche. *Nat Med* 2009; **15**: 701–706.

26 Li X, Nadauld L, Ootani A, Corney DC, Pai RK, Gevaert O *et al.* Oncogenic transformation of diverse gastrointestinal tissues in primary organoid culture. *Nat Med* 2014; **20**: 769–777.

27 Neal JT, Li X, Zhu J, Giangarra V, Grzeskowiak CL, Ju J *et al.* Organoid Modeling of the Tumor Immune Microenvironment. *Cell* 2018; **175**: 1972-1988.e16.

28 Vaira V, Fedele G, Pyne S, Fasoli E, Zadra G, Bailey D *et al.* Preclinical model of organotypic culture for pharmacodynamic profiling of human tumors. *Proc Natl Acad Sci* 2010; **107**: 8352–8356.

29 Murry BP, Blust BE, Singh A, Foster TP, Marchetti D. Heparanase mechanisms of

melanoma metastasis to the brain: Development and use of a brain slice model. *J Cell Biochem* 2006; **97**: 217–225.

30 Chang TC, Mikheev AM, Huynh W, Monnat RJ, Rostomily RC, Folch A. Parallel microfluidic chemosensitivity testing on individual slice cultures. *Lab Chip* 2014; **14**: 4540–4551.

31 Horowitz LF, Rodriguez AD, Dereli-Korkut Z, Lin R, Castro K, Mikheev AM *et al.* Multiplexed drug testing of tumor slices using a microfluidic platform. *npj Precis Oncol* 2020; **4**: 12.

32 Rodriguez A, Horowitz LF, Castro K, Yeung RS, Rostomily RC, Folch A. A microfluidic platform for the delivery of panels of drugs to live tumor slices. *Lab Chip* 2020; **20**: 1658–1675.

33 Wang M, Yao L-C, Cheng M, Cai D, Martinek J, Pan C-X *et al.* Humanized mice in studying efficacy and mechanisms of PD-1-targeted cancer immunotherapy. *FASEB J* 2018; **32**: 1537–1549.

34 Jonas O, Landry HM, Fuller JE, Santini JT, Baselga J, Tepper RI *et al.* An implantable microdevice to perform high-throughput in vivo drug sensitivity testing in tumors. *Sci Transl Med* 2015; **7**: 284ra57.

35 Klinghoffer RA, Bahrami SB, Hatton BA, Frazier JP, Moreno-Gonzalez A, Strand AD *et al.* A technology platform to assess multiple cancer agents simultaneously within a patient's tumor. *Sci Transl Med* 2015; **7**: 284ra56.

36 Chang TC, Mikheev AM, Huynh W, Monnat RJ, Rostomily RC, Folch A. Parallel microfluidic chemosensitivity testing on individual slice cultures. *Lab Chip* 2014; **14**: 4540–51.

37 Folch A, Monnat RJ, Chang C, Horowitz L, Sip CG, Rostomily RC. Microfluidic Assay Apparatus and Methods of Use. 2016.https://patents.google.com/patent/US20140113838.

38 Horowitz LF, Rodriguez AD, Dereli-Korkut Z, Lin R, Castro K, Mikheev AM *et al.* Multiplexed drug testing of cancer slice cultures using a microfluidic delivery platform. *Nat Precis Oncol* 2020; **accepted**. doi:10.1038/s41698-020-0117-y.

39 Horowitz LF, Rodriguez AD, Au-Yeung A, Bishop KW, Barner LA, Mishra G *et al.* Microdissected 'cuboids' for microfluidic drug testing of intact tissues. *Lab Chip* 2021; **21**: 122–142.

40 Zhang Z, Nagrath S. Microfluidics and cancer: Are we there yet? *Biomed Microdevices* 2013; **15**: 595–609.

41 Sackmann EK, Fulton AL, Beebe DJ. The present and future role of microfluidics in biomedical research. Nature. 2014; **507**: 181–189.

42 Hong JW, Quake SR. Integrated nanoliter systems. Nat. Biotechnol. 2003; **21**: 1179–1183.

43 Whitesides GM. The origins and the future of microfluidics. Nature. 2006; **442**: 368–373.

44 Ren K, Zhou J, Wu H. Materials for microfluidic chip fabrication. *Acc Chem Res* 2013; **46**: 2396–2406.

45 Berthier E, Young EWK, Beebe D. Engineers are from PDMS-land, Biologists are from Polystyrenia. *Lab Chip* 2012; **12**: 1224.

46 Toepke MW, Beebe DJ. PDMS absorption of small molecules and consequences in microfluidic applications. *Lab Chip* 2006; **6**: 1484.

47 Regehr KJ, Domenech M, Koepsel JT, Carver KC, Ellison-Zelski SJ, Murphy WL *et al.* Biological implications of polydimethylsiloxane-based microfluidic cell culture. *Lab Chip* 2009; **9**: 2132.

48 Moore TA, Brodersen P, Young EWK. Multiple Myeloma Cell Drug Responses Differ in Thermoplastic vs PDMS Microfluidic Devices. *Anal Chem* 2017; **89**: 11391–11398.

49 Halldorsson S, Lucumi E, Gómez-Sjöberg R, Fleming RMT. Advantages and challenges of microfluidic cell culture in polydimethylsiloxane devices. *Biosens Bioelectron* 2015; **63**: 218–231.

50 Wang JD, Douville NJ, Takayama S, ElSayed M. Quantitative Analysis of Molecular Absorption into PDMS Microfluidic Channels. *Ann Biomed Eng* 2012; **40**: 1862–1873.

51 van Meer BJ, de Vries H, Firth KSA, van Weerd J, Tertoolen LGJ, Karperien HBJ *et al.* Small molecule absorption by PDMS in the context of drug response bioassays. *Biochem Biophys Res Commun* 2017; **482**: 323–328.

52 Shirure VS, George SC. Design considerations to minimize the impact of drug absorption in polymer-based organ-on-a-chip platforms. *Lab Chip* 2017; **17**: 681–690.

53 Delamarche E, Bernard A, Schmid H, Bietsch A, Michel B, Biebuyck H. Microfluidic networks for chemical patterning of substrates: Design and application to bioassays. *J Am Chem Soc* 1998; **120**: 500–508.

54 Mukhopadhyay R. When PDMS isn't the best. Anal. Chem. 2007; **79**: 3249–3253.

55 Naderi A, Bhattacharjee N, Folch A. Digital Manufacturing for Microfluidics. 2019. doi:10.1146/annurev-bioeng-092618.

56 Zhou Z, Xie S, Chen D. *Fundamentals of Digital Manufacturing Science*. Springer London: London, 2012 doi:10.1007/978-0-85729-564-4.

57 Walsh DI, Kong DS, Murthy SK, Carr PA. Enabling Microfluidics: from Clean Rooms to Makerspaces. Trends Biotechnol. 2017; **35**: 383–392.

58 Novak R, Ng CF, Ingber DE. Rapid prototyping of thermoplastic microfluidic devices. In:

Methods in Molecular Biology. Humana Press Inc., 2018, pp 161–170.

59 Bartholomeusz DA, Boutté RW, Andrade JD. Xurography: Rapid prototyping of microstructures using a cutting plotter. *J Microelectromechanical Syst* 2005; **14**: 1364–1374.

60 Malek CGK. Laser processing for bio-microfluidics applications (part II). Anal. Bioanal. Chem. 2006; **385**: 1362–1369.

61 Khan Malek CG. Laser processing for bio-microfluidics applications (part I). *Anal Bioanal Chem* 2006; **385**: 1351–61.

62 Locascio LE, Ross DJ, Howell PB, Gaitan M. Fabrication of polymer microfluidic systems by hot embossing and laser ablation. *Methods Mol Biol* 2006; **339**: 37–46.

63 Klank H, Kutter JP, Geschke O. CO2-laser micromachining and back-end processing for rapid production of PMMA-based microfluidic systems. *Lab Chip* 2002; **2**: 242.

64 Urech L, Lippert T. Photoablation of Polymer Materials. In: *Photochemistry and Photophysics of Polymer Materials*. John Wiley and Sons, 2010, pp 541–568.

65 Tweedie M, Maguire • P D. Microfluidic ratio metering devices fabricated in PMMA by CO 2 laser. doi:10.1007/s00542-020-04902-w.

66 Powell J. CO2 Laser Cutting, 2nd Edition, John Powell. 1998. Springer-Verlag. 248 pp. ISBN 1-852-33047-3. 2020. doi:10.1017/S0263034600214122.

67 Systems U. Universal Systems VLS3.60. https://www.ulsinc.com/products/platforms/vls3-60.

68 David A, Arizpe R. Oncoslice: A Microfluidic Platform for Personalized Cancer Care and Drug Development. .

69 Castro K, Folch A, Lutz B. Digital Manufacturing Techniques for Microfluidic Device

Fabrication. .

70 Mohammed MI, Quayle K, Alexander R, Doeven E, Nai R, Haswell SJ *et al.* Improved Manufacturing Quality and Bonding of Laser Machined Microfluidic Systems. *Procedia Technol* 2015; **20**: 219–224.

71 Kun Lian Z-GL. Post-exposure heat treatment to reduce surface roughness of PMMA surfaces formed by radiation lithography. 2000.

72 Belder D, Ludwig M. Surface modification in microchip electrophoresis. Electrophoresis. 2003; **24**: 3595–3606.

73 Tsao CW, Hromada L, Liu J, Kumar P, DeVoe DL. Low temperature bonding of PMMA and COC microfluidic substrates using UV/ozone surface treatment. *Lab Chip* 2007; **7**: 499–505.

74 Noh HS, Huang Y, Hesketh PJ. Parylene micromolding, a rapid and low-cost fabrication method for parylene microchannel. *Sensors Actuators, B Chem* 2004; **102**: 78–85.

75 Ogilvie IRG, Sieben VJ, Floquet CFA, Zmijan R, Mowlem MC, Morgan H. Reduction of surface roughness for optical quality microfluidic devices in PMMA and COC. *J Micromechanics Microengineering* 2010; **20**: 065016.

76 Tsao CW, DeVoe DL. Bonding of thermoplastic polymer microfluidics. *Microfluid Nanofluidics* 2009; **6**: 1–16.

77 Burke J. Solubility Parameters: Theory and Application. In: *The Book and Paper Group Annual*. The American Institue for Conservation, 1984, p Vol. 3, 2-6, 12-16.

78 Brydson JA, Brydson JA. *Plastics Materials*. Elsevier Science & Technology: Oxford, UNITED KINGDOM, 1999http://ebookcentral.proquest.com/lib/washington/detail.action?docID=318259.

79 Belmares M, Blanco M, Goddard WA, Ross RB, Caldwell G, Chou S-H *et al.* Hildebrand and Hansen Solubility Parameters from Molecular Dynamics with Applications to Electronic Nose Polymer Sensors. *J Comput Chem* 2004; **25**: 1814–1826.

80 Tennico YH, Koesdjojo MT, Kondo S, Mandrell DT, Remcho VT. Surface modification-assisted bonding of polymer-based microfluidic devices. *Sensors Actuators B* 2010; **143**: 799–804.

81 Kim K, Park SW, Yang SS. The optimization of PDMS-PMMA bonding process using silane primer. *BioChip J* 2010; **4**: 148–154.

82 Aran K, Sasso LA, Kamdar N, Zahn JD. Irreversible, direct bonding of nanoporous polymer membranes to PDMS or glass microdevices. *Lab Chip* 2010; **10**: 548–52.

83 Sip CG, Folch A. Stable chemical bonding of porous membranes and poly(dimethylsiloxane) devices for long-term cell culture. *Biomicrofluidics* 2014; **8**: 036504.

84 Pourmand A, Shaegh SAM, Ghavifekr HB, Najafi Aghdam E, Dokmeci MR, Khademhosseini A *et al.* Fabrication of whole-thermoplastic normally closed microvalve, micro check valve, and micropump. *Sensors Actuators B Chem* 2018; **262**: 625–636.

85 Shaegh SAM, Pourmand A, Nabavinia M, Avci H, Tamayol A, Mostafalu P *et al.* Rapid prototyping of whole-thermoplastic microfluidics with built-in microvalves using laser ablation and thermal fusion bonding. *Sensors Actuators, B Chem* 2018; **255**: 100–109.

86 Pourmand A, Shaegh SAM, Ghavifekr HB, Najafi Aghdam E, Dokmeci MR, Khademhosseini A *et al.* Fabrication of whole-thermoplastic normally closed microvalve, micro check valve, and micropump. *Sensors Actuators B Chem* 2018; **262**: 625–636.

87 Dang F, Shinohara S, Tabata O, Yamaoka Y, Kurokawa M, Shinohara Y *et al.* Replica

multichannel polymer chips with a network of sacrificial channels sealed by adhesive printing method. *Lab Chip* 2005; **5**: 472–478.

88 Han J, Lee S, Puntambekar A, Murugesan' S, Cboj J-W, Beaucage' G *et al.* UV ADHESIVE BONDING TECHNIQUES IN ROOM TEMPERATURE FOR PLASTIC LAB-ON-A-CHIPS. .

89 Lu C, Lee LJ, Juang YJ. Packaging of microfluidic chips via interstitial bonding technique. *Electrophoresis* 2008; **29**: 1407–1414.

90 CLAREX® Optical Quality Cell Cast Precision Thin Sheet. https://astraproducts.com/info-acrylic-precision-thin-sheet.asp (accessed 16 Jul2020).

91 Meijer TG, Naipal KA, Jager A, van Gent DC. Ex vivo tumor culture systems for functional drug testing and therapy response prediction. *Futur Sci OA* 2017; **3**: FSO190.

92 Majumder B, Baraneedharan U, Thiyagarajan S, Radhakrishnan P, Narasimhan H, Dhandapani M *et al.* Predicting clinical response to anticancer drugs using an ex vivo platform that captures tumour heterogeneity. *Nat Commun* 2015; **6**: 1–14.

93 Raju ENS, Kuechler J, Behling S, Sridhar S, Hirseland E, Tronnier V *et al.* Maintenance of Stemlike Glioma Cells and Microglia in an Organotypic Glioma Slice Model. *Neurosurgery* 2015; **77**: 629–643.

94 Merz F, Gaunitz F, Dehghani F, Renner C, Meixensberger J, Gutenberg A *et al.* Organotypic slice cultures of human glioblastoma reveal different susceptibilities to treatments. *Neuro Oncol* 2013; **15**: 670–681.

95 de Graaf IAM, Olinga P, de Jager MH, Merema MT, de Kanter R, van de Kerkhof EG *et al.* Preparation and incubation of precision-cut liver and intestinal slices for application in drug metabolism and toxicity studies. *Nat Protoc* 2010; **5**: 1540–1551.

96 Guyot C, Lepreux S, Combe C, Sarrazy V, Billet F, Balabaud C *et al.* Fibrogenic cell phenotype modifications during remodelling of normal and pathological human liver in cultured slices. *Liver Int* 2010; **30**: 1529–1540.

97 Kanter R, Monshouwer M, Meijer D, Groothuis G. Precision-Cut Organ Slices as a Tool to Study Toxicity and Metabolism of Xenobiotics with Special Reference to Non-Hepatic Tissues. *Curr Drug Metab* 2002; **3**: 39–59.

98 Rosales Gerpe MC, van Vloten JP, Santry LA, de Jong J, Mould RC, Pelin A *et al.* Use of Precision-Cut Lung Slices as an Ex Vivo Tool for Evaluating Viruses and Viral Vectors for Gene and Oncolytic Therapy. *Mol Ther Methods Clin Dev* 2018; **10**: 245–256.

99 Poosti F, Pham BT, Oosterhuis D, Poelstra K, van Goor H, Olinga P *et al.* Precision-cut kidney slices (PCKS) to study development of renal fibrosis and efficacy of drug targeting ex vivo. *Dis Model Mech* 2015; **8**: 1227–36.

100 Kallendrush S, Körfer J, Lordick F, Bechmann I. Human tumor slice cultures for cancer research and drug testing. *Integr Cancer Sci Ther* 2017; **4**: 1–5.

101 Minami N, Maeda Y, Shibao S, Arima Y, Ohka F, Kondo Y *et al.* Organotypic brain explant culture as a drug evaluation system for malignant brain tumors. *Cancer Med* 2017; **6**: 2635–2645.

102 Roife D, Dai B, Kang Y, Perez MVR, Pratt M, Li X *et al.* Ex vivo testing of patient-derived xenografts mirrors the clinical outcome of patients with pancreatic ductal adenocarcinoma. *Clin Cancer Res* 2016; **22**: 6021–6030.

103 Naipal KAT, Verkaik NS, Sánchez H, van Deurzen CHM, den Bakker MA, Hoeijmakers JHJ *et al.* Tumor slice culture system to assess drug response of primary breast cancer. *BMC Cancer* 2016; **16**: 78.

104 Huang Y, Williams JC, Johnson SM. Brain slice on a chip: Opportunities and challenges of applying microfluidic technology to intact tissues. Lab Chip. 2012; **12**: 2103–2117.

105 Scott A, Weir K, Easton C, Huynh W, Moody WJ, Folch A. A microfluidic microelectrode array for simultaneous electrophysiology, chemical stimulation, and imaging of brain slices. *Lab Chip* 2013; **13**: 527–535.

106 Roper MG, Shackman JG, Dahlgren GM, Kennedy RT. Microfluidic chip for continuous monitoring of hormone secretion from live cells using an electrophoresis-based immunoassay. *Anal Chem* 2003; **75**: 4711–4717.

107 Rocheleau J V., Walker GM, Head SS, McGuinness OP, Piston DW. Microfluidic glucose stimulation reveals limited coordination of intracellular Ca2+ activity oscillations in pancreatic islets. *Proc Natl Acad Sci U S A* 2004; **101**: 12899–12903.

108 Godwin LA, Pilkerton ME, Deal KS, Wanders D, Judd RL, Easley CJ. Passively operated microfluidic device for stimulation and secretion sampling of single pancreatic islets. *Anal Chem* 2011; **83**: 7166–7172.

109 Li X, Brooks JC, Hu J, Ford KI, Easley CJ. 3D-templated, fully automated microfluidic input/output multiplexer for endocrine tissue culture and secretion sampling. *Lab Chip* 2017; **17**: 341–349.

110 Li X, Easley CJ. Microfluidic systems for studying dynamic function of adipocytes and adipose tissue. Anal. Bioanal. Chem. 2018; **410**: 791–800.

111 Brooks JC, Ford KI, Holder DH, Holtan MD, Easley CJ. Macro-to-micro interfacing to microfluidic channels using 3D-printed templates: Application to time-resolved secretion sampling of endocrine tissue. *Analyst* 2016; **141**: 5714–5721.

112 Zambon A, Zoso A, Gagliano O, Magrofuoco E, Fadini GP, Avogaro A *et al.* High

Temporal Resolution Detection of Patient-Specific Glucose Uptake from Human ex Vivo Adipose Tissue On-Chip. *Anal Chem* 2015; **87**: 6535–6543.

113 Dawson A, Dyer C, Macfie J, Davies J, Karsai L, Greenman J *et al.* A microfluidic chip based model for the study of full thickness human intestinal tissue using dual flow. *Biomicrofluidics* 2016; **10**: 064101.

114 Richardson A, Schwerdtfeger LA, Eaton D, McLean I, Henry CS, Tobet SA. A microfluidic organotypic device for culture of mammalian intestines: Ex vivo. *Anal Methods* 2020; **12**: 297–303.

115 Shim S, Belanger MC, Harris AR, Munson Bde JM, Pompano RR. Lab on a Chip Two-way communication between ex vivo tissues on a microfluidic chip: application to tumor-lymph node interaction †. 2019; **19**: 1013.

116 Ross AE, Belanger MC, Woodroof JF, Pompano RR. Spatially resolved microfluidic stimulation of lymphoid tissue ex vivo †. *Analyst* 2017; **142**: 649.

117 Van Midwoud PM, Merema MT, Verpoorte E, Groothuis GMM. A microfluidic approach for in vitro assessment of interorgan interactions in drug metabolism using intestinal and liver slices. *Lab Chip* 2010; **10**: 2778–2786.

118 van Midwoud PM, Janse A, Merema MT, Groothuis GMM, Verpoorte E. Comparison of Biocompatibility and Adsorption Properties of Different Plastics for Advanced Microfluidic Cell and Tissue Culture Models. *Anal Chem* 2012; **84**: 3938–3944.

119 Heinonen JT, Sidhu JS, Reilly MT, Farin FM, Omiecinski CJ, Eaton DL *et al.* Assessment of regional cytochrome P450 activities in rat liver slices using resorufin substrates and fluorescence confocal laser cytometry. *Environ Health Perspect* 1996; **104**: 536–543.

120 Hattersley SM, Dyer CE, Greenman J, Haswell SJ. Development of a microfluidic device

for the maintenance and interrogation of viable tissue biopsies. *Lab Chip* 2008; **8**: 1842–1846.

121 Komeya M, Kimura H, Nakamura H, Yokonishi T, Sato T, Kojima K *et al.* Long-term ex vivo maintenance of testis tissues producing fertile sperm in a microfluidic device. *Sci Rep* 2016; **6**: 1–10.

122 Xiao S, Coppeta JR, Rogers HB, Isenberg BC, Zhu J, Olalekan SA *et al.* A microfluidic culture model of the human reproductive tract and 28-day menstrual cycle. *Nat Commun* 2017; **8**: 1–13.

123 Horowitz, L.F., Rodriguez, A.D., Dereli, Z, Lin, R, Monnat Jr., R, Folch, A, Rostomily RC. Multiplexed drug testing of cancer slice cultures using a microfluidic delivery platform. *Nat Precis Oncol* 2019.

124 Bhattacharjee N, Parra-Cabrera C, Kim YT, Kuo AP, Folch A. Desktop-Stereolithography 3D-Printing of a Poly(dimethylsiloxane)-Based Material with Sylgard-184 Properties. *Adv Mater* 2018; **30**: e1800001.

125 Kuo AP, Bhattacharjee N, Lee Y, Castro K, Kim YT, Folch A. High-Precision Stereolithography of Biomicrofluidic Devices. *Adv Mater Technol* 2019; **4**: 1800395.

126 Wang ZK, Zheng HY, Lim RYH, Wang ZF, Lam YC. Improving surface smoothness of laser-fabricated microchannels for microfluidic application. *J Micromechanics Microengineering* 2011; **21**: 095008.

127 Samavedi S, Poindexter LK, Van Dyke M, Goldstein AS. Synthetic Biomaterials for Regenerative Medicine Applications. *Regen Med Appl Organ Transplant* 2014; : 81–99.

128 Zhao B, Moore JS, Beebe DJ. Surface-directed liquid flow inside microchannels. *Science* 2001; **291**: 1023–6.

129 Hsu C-H, Chen C, Folch A. “Microcanals” for micropipette access to single cells in microfluidic environments. *Lab Chip* 2004; **4**: 420–424.

130 Sip CG, Bhattacharjee N, Folch A. Microfluidic transwell inserts for generation of tissue culture-friendly gradients in well plates. *Lab Chip* 2014; **14**: 302–314.

131 Hilderbrand, Joel H., Scott RL. *The Solubility of Nonelectrolytes*. Reinhold Publishing Corporation: New York, 1936.

132 Jiang J, Zhan J, Yue W, Yang M, Yi C, Li C-W. A single low-cost microfabrication approach for polymethylmethacrylate, polystyrene, polycarbonate and polysulfone based microdevices. *RSC Adv* 2015; **5**: 36036–36043.

133 Vesel A, Mozetic M. Surface modification and ageing of PMMA polymer by oxygen plasma treatment. *Vacuum* 2012; **86**: 634–637.

134 Cheeseman SL, Joel SP, Chester JD, Wilson G, Dent JT, Richards FJ *et al.* A ‘modified de Gramont’ regimen of fluorouracil, alone and with oxaliplatin, for advanced colorectal cancer. *Br J Cancer* 2002; **87**: 393.

135 Souglakos J, Androulakis N, Syrigos K, Polyzos A, Ziras N, Athanasiadis A *et al.* FOLFOXIRI (folinic acid, 5-fluorouracil, oxaliplatin and irinotecan) vs FOLFIRI (folinic acid, 5-fluorouracil and irinotecan) as first-line treatment in metastatic colorectal cancer (MCC): a multicentre randomised phase III trial from the Hellenic Oncology Research Group (HORG). *Br J Cancer* 2006; **94**: 798–805.

136 Jiang X, Seo YD, Chang JH, Coveler A, Nigjeh EN, Pan S *et al.* Long-lived pancreatic ductal adenocarcinoma slice cultures enable precise study of the immune microenvironment. *Oncoimmunology* 2017; **6**: e1333210.

137 Seo YD, Jiang X, Sullivan KM, Jalikis FG, Smythe KS, Abbasi A *et al.* Mobilization of

CD8+ T cells via CXCR4 blockade facilitates PD-1 checkpoint therapy in human pancreatic cancer. *Clin Cancer Res* 2019; **25**: 3934–3945.

138 Zboralski D, Hoehlig K, Eulberg D, Frömming A, Vater A. Increasing tumor-infiltrating T cells through inhibition of CXCL12 with NOX-A12 synergizes with PD-1 blockade. *Cancer Immunol Res* 2017; **5**: 950–956.

139 Vianello F, Papeta N, Chen T, Kraft P, White N, Hart WK *et al.* Murine B16 Melanomas Expressing High Levels of the Chemokine Stromal-Derived Factor-1/CXCL12 Induce Tumor-Specific T Cell Chemorepulsion and Escape from Immune Control. *J Immunol* 2006; **176**: 2902–2914.

140 Thorsen T, Maerkl SJ, Quake SR. Microfluidic large-scale integration. *Science* 2002; **298**: 580–4.

141 Cooksey GA, Sip CG, Folch A. A multi-purpose microfluidic perfusion system with combinatorial choice of inputs, mixtures, gradient patterns, and flow rates. *Lab Chip* 2009; **9**: 417–426.

142 Unger MA, Chou HP, Thorsen T, Scherer A, Quake SR. Monolithic Microfabricated Valves and Pumps by Multilayer Soft Lithography. *Science (80-)* 2000; **288**: 113–116.

143 Lai H, Folch A. Design and dynamic characterization of "single-stroke" peristaltic PDMS micropumps. *Lab Chip* 2011; **11**: 336–342.

144 Lam EW, Cooksey GA, Finlayson BA, Folch A. Microfluidic circuits with tunable flow resistances. *Appl Phys Lett* 2006; **89**: 164105.

145 Hsu C-H, Folch A. Spatio-temporally-complex concentration profiles using a tunable chaotic micromixer. *Appl Phys Lett* 2006; **89**: 144102.

146 Ng SP, Wiria FE, Tay NB. Low Distortion Solvent Bonding of Microfluidic Chips.

Procedia Eng 2016; **141**: 130–137.

147 Neils C, Tyree Z, Finlayson B, Folch A. Combinatorial mixing of microfluidic streams. *Lab Chip* 2004; **4**: 342–350.

148 Kenerson, Heidi, Yeung R. Tumor Slice Culture as a Biologic Surrogate of Human Cancer. *Ann Transl Med* 2019; : accepted.

149 Schindelin J, Arganda-Carreras I, Frise E, Kaynig V, Longair M, Pietzsch T *et al.* Fiji: An open-source platform for biological-image analysis. *Nat Methods* 2012; **9**: 676–682.

150 Carpenter AE, Jones TR, Lamprecht MR, Clarke C, Kang I, Friman O *et al.* CellProfiler: image analysis software for identifying and quantifying cell phenotypes. *Genome Biol* 2006; **7**: R100.

151 Balko JM, Sosman JA. A critical need for better cancer immunotherapy models: Are organotypic tumor spheroid cultures the answer? *Cancer Discov* 2018; **8**: 143–145.

152 Jahnke HG, Poenick S, Maschke J, Kendler M, Simon JC, Robitzki AA. Direct chemosensitivity monitoring ex vivo on undissociated melanoma tumor tissue by impedance spectroscopy. *Cancer Res* 2014; **74**: 6408–6418.

153 Simeone K, Guay-Lord R, Lateef MA, Péant B, Kendall-Dupont J, Orimoto AM *et al.* Paraffin-embedding lithography and micro-dissected tissue micro-arrays: tools for biological and pharmacological analysis of ex vivo solid tumors. *Lab Chip* 2019; **19**: 693–705.

154 Esch EW, Bahinski A, Huh D. Organs-on-chips at the frontiers of drug discovery. Nat. Rev. Drug Discov. 2015; **14**: 248–260.

155 Skardal A, Shupe T, Atala A. Organoid-on-a-chip and body-on-a-chip systems for drug screening and disease modeling. Drug Discov. Today. 2016; **21**: 1399–1411.

156 Ronaldson-Bouchard K, Vunjak-Novakovic G. Organs-on-a-Chip: A Fast Track for Engineered Human Tissues in Drug Development. Cell Stem Cell. 2018; **22**: 310–324.

157 McLean IC, Schwerdtfeger LA, Tobet SA, Henry CS. Powering ex vivo tissue models in microfluidic systems. *Lab Chip* 2018; **18**: 1399–1410.

158 Horowitz LF, Rodriguez AD, Ray T, Folch A. Microfluidics for interrogating live intact tissues. Microsystems Nanoeng. 2020; **6**. doi:10.1038/s41378-020-0164-0.

159 Tan WH, Takeuchi S. A trap-and-release integrated microfluidic system for dynamic microarray applications. *Proc Natl Acad Sci U S A* 2007; **104**: 1146–1151.

160 Kobel S, Valero A, Latt J, Renaud P, Lutolf M. Optimization of microfluidic single cell trapping for long-term on-chip culture. *Lab Chip* 2010; **10**: 857–863.

161 Das T, Meunier L, Barbe L, Provencher D, Guenat O, Gervais T *et al.* Empirical chemosensitivity testing in a spheroid model of ovarian cancer using a microfluidics-based multiplex platform. doi:10.1063/1.4774309.

162 Astolfi M, Fartoumi S, Kataria S, Faille M-H, Sanger W, Morin O *et al.* On-chip trapping and viability assessment of submicroliter primary tissues for personalized treatment of ovarian cancer. In: *Proceedings of the 17th International Conference on Minitiarization in Chemistry and the Life Sciences, Freiburg, Germany*. 2013, pp 422–424.

163 Moshksayan K, Kashaninejad N, Warkiani ME, Lock JG, Moghadas H, Firoozabadi B *et al.* Spheroids-on-a-chip: Recent advances and design considerations in microfluidic platforms for spheroid formation and culture. *Sensors Actuators, B Chem* 2018; **263**: 151–176.

164 Pauli C, Puca L, Mosquera JM, Robinson BD, Beltran H, Rubin MA *et al.* An emerging role for cytopathology in precision oncology. *Cancer Cytopathol* 2016; **124**: 167–173.

165 Zanoni M, Piccinini F, Arienti C, Zamagni A, Santi S, Polico R *et al.* 3D tumor spheroid models for in vitro therapeutic screening: a systematic approach to enhance the biological relevance of data obtained. *Sci Rep* 2016; **6**: 19103.

166 Astolfi M, Péant B, Lateef MA, Rousset N, Kendall-Dupont J, Carmona E *et al.* Micro-dissected tumor tissues on chip: an ex vivo method for drug testing and personalized therapy. *Lab Chip* 2016; **16**: 312–325.

167 Glaser AK, Reder NP, Chen Y, McCarty EF, Yin C, Wei L *et al.* Light-sheet microscopy for slide-free non-destructive pathology of large clinical specimens. *Nat Biomed Eng* 2017; **1**: 84.

168 Barner LA, Glaser AK, True LD, Reder NP, Liu JTC. Solid immersion meniscus lens (SIMlens) for open-top light-sheet microscopy. *Opt Lett* 2019; **44**: 4451.

169 Glaser AK, Reder NP, Chen Y, Yin C, Wei L, Kang S *et al.* Multi-immersion open-top light-sheet microscope for high-throughput imaging of cleared tissues. *Nat Commun* 2019; **10**: 2781.

170 Klingberg A, Hasenberg A, Ludwig-Portugall I, Medyukhina A, Männ L, Brenzel A *et al.* Fully automated evaluation of total glomerular number and capillary tuft size in nephritic kidneys using lightsheet microscopy. *J Am Soc Nephrol* 2017; **28**: 452–459.

171 Serafin R, Xie W, Glaser AK, Liu JTC. FalseColor-Python: a rapid intensity-leveling and digital-staining package for fluorescence-based slide-free digital pathology. *bioRxiv* 2020. doi:10.1101/2020.05.03.074955.

172 Baratta JL, Ngo A, Lopez B, Kasabwalla N, Longmuir KJ, Robertson RT. Cellular organization of normal mouse liver: A histological, quantitative immunocytochemical, and fine structural analysis. *Histochem Cell Biol* 2009; **131**: 713–726.

173 Tan W-H, Takeuchi S. A trap-and-release integrated microfluidic system for dynamic microarray applications. *Proc Natl Acad Sci* 2007; **104**: 1146–1151.

174 Teshima T, Ishihara H, Iwai K, Adachi A, Takeuchi S. A dynamic microarray device for paired bead-based analysis. *Lab Chip* 2010; **10**: 2443.

175 Liu D, Garimella S V. Investigation of Liquid Flow in Microchannels. *J Thermophys HEAT Transf*; **18**. doi:10.2514/1.9124.

176 Wu HY, Cheng P. Friction factors in smooth trapezoidal silicon microchannels with different aspect ratios. doi:10.1016/S0017-9310(03)00106-6.

177 Bahrami M, Yovanovich MM, Culham JR. Pressure drop of fully-developed, laminar flow in microchannel of arbitrary cross-section. *J Fluids Eng Trans ASME* 2006; **128**: 1036–1044.

178 Ruppen J, Cortes-Dericks L, Marconi E, Karoubi G, Schmid RA, Peng R *et al.* A microfluidic platform for chemoresistive testing of multicellular pleural cancer spheroids. *Lab Chip* 2014; **14**: 1198–1205.

179 Noda H. Physico-chemical studies on the soluble collagen of rat-tail tendon. *BBA - Biochim Biophys Acta* 1955; **17**: 92–98.

180 Gonzalez-Tello P, Camacho F, Blazquez G. Density and Viscosity of Concentrated Aqueous Solutions of Polyethylene Glycol. *J Chem Eng Data* 1994; **39**: 611–614.

181 Knocke WR, Dishman CM, Miller GF. Measurement of chemical sludge floc density and implications related to sludge dewatering. *Water Environ Res* 1993; **65**: 735–743.

182 Jackson-Holmes EL, Mcdevitt TC, Lu H. A microfluidic trap array for longitudinal monitoring and multi-modal phenotypic analysis of individual stem cell aggregates HHS Public Access. 2017; **17**: 3634–3642.

183 Kapusta P. Absolute Diffusion Coefficients: Compilation of Reference Data for FCS Calibration. 2010. doi:10.1209/0295-5075/83/46001.

184 Urien S, Lokiec F. Population pharmacokinetics of total and unbound plasma cisplatin in adult patients. *Br J Clin Pharmacol* 2004; **57**: 756–763.

185 Balázs B, Deschamps J, Albert M, Ries J, Hufnagel L. A real-time compression library for microscopy images. bioRxiv. 2017; : 164624.

186 Hörl D, Rojas Rusak F, Preusser F, Tillberg P, Randel N, Chhetri RK *et al.* BigStitcher: reconstructing high-resolution image datasets of cleared and expanded samples. *Nat Methods* 2019; **16**: 870–874.

187 Serafin R. False Color Python. GitHub Repos. 2020.

188 Giacomelli MG, Husvogt L, Vardeh H, Faulkner-Jones BE, Hornegger J, Connolly JL *et al.* Virtual hematoxylin and eosin transillumination microscopy using epi-fluorescence imaging. *PLoS One* 2016; **11**: 1–13.